DESIGN AND CONTROL OF TUNABLE OPTICAL RESONANCES IN

PLASMONIC NANOPARTICLE ENSEMBLES

by

ANDREA GOERING

A DISSERTATION

Presented to the Department of Physics
and the Graduate School of the University of Oregon
in partial fulfillment of the requirements
for the degree of
Doctor of Philosophy

March 2019

DISSERTATION APPROVAL PAGE

Student: Andrea Goering

Title: Design and Control of Tunable Optical Resonances in Plasmonic Nanoparticle Ensembles

This dissertation has been accepted and approved in partial fulfillment of the requirements for the Doctor of Philosophy degree in the Department of Physics by:

Dr. Benjamín Alemán	Chair
Dr. Miriam Deutsch	Advisor
Dr. Richard Taylor	Core Member
Dr. Mark Lonergan	Institutional Representative

and

Janet Woodruff-Borden	Vice Provost and Dean of the Graduate School

Original approval signatures are on file with the University of Oregon Graduate School.

Degree awarded March 2019

DISSERTATION ABSTRACT

Andrea Goering

Doctor of Philosophy

Department of Physics

March 2019

Title: Design and Control of Tunable Optical Resonances in Plasmonic Nanoparticle Ensembles

Predicting and verifying the tunable optical properties of metal nanostructures is central to designing materials optimized for specific applications. Chemically-deposited nanostructures have been well-studied near the percolation threshold, but at lower surface coverages they exhibit sample-to-sample variations in the optical response. We identify how these variations are driven by the high variability in the particle size distribution in a particular surface coverage range. We then explore film-coupled nanoparticle systems consisting of a silver nanoparticle, thin dielectric spacer layer, and flat silver film, to enable tuning toward the blue and green parts of the spectrum. We use the boundary element method to visualize charge distributions of various resonances. We fabricate samples using thermal evaporation and spin coating methods, and use polarized reflectance spectroscopy to measure their optical response at an ensemble level. We achieve a 532nm resonance for 80nm silver nanoparticles on 13nm PMMA spacers and 100nm silver thin films. The resulting design is a candidate for enhancing fluorescence in a new spectral range. This dissertation includes previously unpublished co-authored material.

CURRICULUM VITAE

NAME OF AUTHOR: Andrea Goering

GRADUATE AND UNDERGRADUATE SCHOOLS ATTENDED:
    University of Oregon, Eugene, OR
    Colorado School of Mines, Golden, CO

DEGREES AWARDED:
    Doctor of Philosophy, Physics, 2019, University of Oregon
    Bachelor of Science, Engineering Physics, 2010, Colorado School of Mines

AREAS OF SPECIAL INTEREST:
    Optics, Plasmonics, Nanophotonics
    Science Policy, Science Writing, Science Communication

PROFESSIONAL EXPERIENCE:

    Graduate Teaching Fellow, University of Oregon, 2010-2012, 2015-2017, and
        2018-present

    Graduate Research Assistant, University of Oregon, 2017-2018

    National Science Foundation Graduate Research Fellow, University of Oregon,
        2012-2015

GRANTS, AWARDS AND HONORS:

    National Science Foundation Graduate Research Fellowship, 2012-2015

    Weiser Senior Teaching Award, University of Oregon, 2012, 2016, and 2017

ACKNOWLEDGEMENTS

There are many things I've learned the hard way in graduate school. Many teachers have probably tried to share their wisdom, but I am quite sure that we must learn certain lessons in our own time. I am grateful that I have had the chance to learn, to play, to fail, to explore, to exchange ideas with others, and to have done all of this in a community which helped me when I was stuck, consoled me when I failed, provided me with new ideas, challenged my assumptions, and allowed me to occasionally chase wild geese. I am endlessly grateful to my advisor Miriam for the gift of time, space, and resources to learn the hard way. There will always be more people I would like to thank for their contributions to my journey than space on the page will allow, but the following individuals deserve my specific gratitude.

Mom: thank you for modeling how to be fiercely independent and passionately opinionated. Dad: thanks for using a Coke bottle to explain calculus to me, and in the process teaching me that cool people love math. Also, thanks for not complaining when I beat you in Scrabble, and not gloating when you won. Eldon: thanks for indulging my many questions, for sharing your wild ideas, and for getting me hooked on NPR. You always knew I was a space cadet. To my grandma Patty: thanks for teaching me to respond to adversity with laughter. To my grandma Loree: your perennial greeting is "What do you know, kid?" I might finally have an answer.

Thanks to Jeremy, Chris, Liza, Alex, Yasin, Dileep, Kyle, Erik, and Jason, for banding together to survive our first year. To my peer mentors, Fehmi and Kara: I hope I have been as helpful to you as you have to me. Thanks to David Miller, who graciously assisted me with SEM; to David Westley Miller, who is always quick with a helpful idea; and to Kahli Burke, rubber ducky extraordinaire. Thanks to my

colleagues in the Deutsch Lab (Shikha, Brian, Caleb, Yevgeniy, and Mick) and the undergraduates who worked with us (Felicia, Cynthia, Emily, Aaron, and Madison). I'm glad I got to learn from, with, and alongside you. Thanks to Fuding Lin and Kurt Langworthy of CAMCOR, John Boosinger and Cliff Dax of the machine and electronics shop, and Jodi Myers in the physics office.

I have had many teachers over the years, but a few stand out: I learned a good deal of physics from Paul Csonka, Dan Steck, and Hailin Wang. I wouldn't have made it this far without the encouragement of my mentors at the UO (Ben McMorran, Benjamín Alemán, and Greg Bothun) and at CSM (Reuben Collins, Tom Furtak, Vince Kuo, and Chuck Stone). To my McBride professors Kay Godel-Gengenbach, Dave Muñoz, and Dendy Sloan: thanks for pointing out that the real world is both more complicated and more elegant than we usually give it credit for. Thanks to Stan Micklavzina and Brandy Todd: you both taught me that science is about joy, wonder, and belonging.

Thanks to the Big House, Rock House, Farm House, Thai Monday, and Marche crews, and numerous friends who love to ski, bike, run, camp, or drink beer, for encouraging me to explore the wider world. Thanks to my yoga teachers, my massage therapist, and my meditation pals, for helping me continue to find my center.

Last, but not least: to my husband Adam Goering, thank you for building a life with me, and for diving in even when we didn't know what we were doing.

TABLE OF CONTENTS

LIST OF FIGURES

LIST OF TABLES

CHAPTER I

INTRODUCTION

In September of 1950, eastern Canada and the United States were treated to a blue moon. Huge plumes of smoke produced by fires in Canadian muskeg swamps contained particles of just the right size to cause "bluing."[1] The expression "once in a blue moon" is an idiom for all things rare because observing a blue moon is itself so rare. We are more familiar with the blood red moon observed near moonrise and moonset. The moon appears red when it is low on the horizon for the same reason the sunset appears red.[1] A variety of other colorful atmospheric phenomena, including rainbows, white clouds, and the blue sky, each owe their explanations to the scattering of light by small particles.

FIGURE 1.1. Colorful atmospheric phenomena in a Eugene, Oregon sunset.

---

[1]On Earth, anyway; Martian sunsets are blue.[2]

Scientists are often inspired by some unusual observation that draws in our curiosity, which drives us to poke and prod, theorize and investigate, and embark on a voyage of discovery. What we learn along the way can be used to predict yet more unusual behavior, which we eagerly seek to create in the laboratory in the quest to find something completely new and unique in this world. The unusual optical behavior of the Lycurgus cup is a wonderful example (Fig. 1.2). When lit from the front, the cup reflects a dusty jade green. However, when it is lit from behind or from within, it glows ruby red. This unusual behavior is due to small gold and silver particles which are (probably accidentally) embedded within the glass.

FIGURE 1.2. Dichroic phenomena due to nanoparticles in the Lycurgus Cup. The cup, made entirely from glass (including the cameo) appears green when light is reflected from its surface (left) but red when light transmits through it (right). Images by user Johnbod on Wikimedia Commons, copyright CC-BY-SA 3.0.

Though stained glass was studied throughout the 1600s, the gold particles themselves were not a research subject until 1856. That summer, the prodigious tinkerer Michael Faraday was mounting gold leaf to microscope slides. The process accidentally created a ruby red solution, which he kept and began to study. The colorful behavior of gold colloids were later probed experimentally by Walter

Streubing, whose dissertation prompted his advisor, Gustav Adolf Feodor Wilhelm Ludwig Mie, to develop a theoretical explanation of the colorful behavior of gold colloids in 1908.[3] Strangely, though this work is what Mie is best known for today, particle scattering is a topic he touched on only briefly and never returned to or considered to be a consequential contribution. Still, Mie's voyage of discovery resulted in a way to understand not only how small bits of gold behave, but also much more: the Mie theory explains why we sometimes see blood moons and sometimes blue moons, has been used to interpret radar for weather forecasting here on Earth and to learn about the cosmos by fingerprinting space dust, and provides a foundation for building novel synthetic materials that bend light backwards.[4]

The interaction of light with small particles is deep at the heart of many scientific stories, and it is certainly the core of my own. My work focuses on the opportunity to tune the optical response of silver nanostructures to specific colors in the visible range. In the following section, I will describe how the spectral tunability made possible by metal nanostructures can contribute to a variety of scientific questions and practical applications. Then, I will identify two approaches to tunability using different material systems, and discuss the open questions for each system that this dissertation will address.

1.1. Spectral tunability in metal nanostructures

There are many basic scientific questions which spectrally-tunable metal nanostructures can help to answer. For example, researchers are able to measure emission of single molecules,[5, 6] and dynamically monitor vibrations, rotations, and conformation changes of molecules in situ using surface enhanced spectroscopies.[7, 8] The first surface-enhanced spectroscopy to be discovered was surface enhanced

Raman spectroscopy (SERS), which relied on placing molecules onto roughened noble metal surfaces,[9] and was eventually understood to rely on electromagnetic field enhancements in nanoscale "hot spots."[10] These discoveries sparked the development of SERS substrates engineered to enhance signal over either broad or narrow spectral ranges, using solution-deposited silver aggregates,[11] arrays of nanoparticle clusters,[12] nanocavities in flat silver films,[13] and particles on films.[14] A family of surface-enhanced spectroscopies now exist, including plasmon-enhanced fluorescence spectroscopy, in which metal particles efficiently radiate, at an enhanced intensity, the light emitted by a fluorophore in their vicinity.[15, 16] The highest fluorescence enhancements are achieved when the overlap between the molecular absorption and emission spectra of the fluorophore and the metal nanoparticle resonance overlap.[17] Thus, the tunability of the nanostructure resonance to match a given fluorophore is a design requirement for measuring molecular behavior.

Just as molecular measurements can be made at the nanoscale, so too can distance measurements. In nanoparticle pairs and nanoparticles spaced from metal films by thin spacer layers, optical response is sensitive to the spacing between the metallic elements. This sensitivity to distances at the nanoscale has led to "plasmon rulers."[18] While distances less than 10nm can be measured via Förster Resonance Energy Transfer (FRET), plasmon rulers push nanoscale measurements beyond that 10nm limit.[19] In fact, the shifting colors of particles as they pack closely together is the physics behind the home pregnancy test. The molecule human chorionic gonadotropin hormone (hCG), present during pregnancy, doesn't scatter enough light to be measured. However, in pregnancy tests, the molecule binds to a substrate. In turn, secondary antibodies linked to gold nanoparticles bind to the hCG molecules, causing the nanoparticles to form a monolayer near the substrate. The interactions

between the now densely-packed nanoparticles shift their color from light green to bright red and confirm the presence of hCG (and, by extension, a pregnancy).[20]

1.2. Chapter outline

These applications revolve around the same questions: how do we tune the optical response of silver nanostructures to specific colors in the visible range? How do we produce nanostructures which behave as we wish in the easiest and least expensive way? What tradeoffs exist between the ease of fabrication, the robustness of the resulting structure, and the predictability of the optical response? We have identified two approaches to producing field enhancements in spectral ranges optimized for specific applications, following the principle that either absorption or emission enhancements are greatest when the spectra of the absorber or emitter material matches the spectra of the nanostructure.

First, we can target field enhancements toward absorbers with broad absorption spectra, such as photovoltaic materials. In that case, we would like to design nanostructured materials which also have broad spectra (which may be composed of many discrete and overlapping resonances). A good candidate for this case is solution-processed silver, whose optical spectra can range from narrow to broad. These nanostructures are composed of single particle building blocks that either bind to the substrate or to other particles as the chemical process proceeds. The main measure of film morphology in these systems, commonly described by the percolation model, is the surface coverage. There is some surface coverage at which the film is considered "percolated;" that is, if you were an electron, you could find your way from one edge of the substrate to the other by following some twisting path of connected metal parts. However, far from the percolation threshold, the surface

coverage is not an adequate metric for predicting the optical properties of the films. In Chapter III (which contains unpublished co-authored material), I dig deeper into the film morphological and optical properties to find a better metric that does help to predict the strength of resonances at different colors in the optical spectrum.

Second, we can target spectral selectivity in a narrow range, for example to measure fluorophores with narrow absorption spectra. In that case, the nanostructure spectra should also be narrow, and easily tunable to match a given fluorophore's absorption peak. For this application, we turn to monodisperse nanoparticle colloids spaced nanometers away from flat metal films, which offer excellent spectral selectivity. Most investigators focus on gold nanoparticles, achieving spectral selectivity mostly in the red and infrared. Only rarely has silver been used to target resonances in the blue and green. In particular, little has been done to address the range near the popular 532nm laser line. Therefore, in Chapter IV, I turn to monodisperse silver nanospheres near silver spheres, and simulate their response in order to predict how to produce specific colors via careful control of the spacer layer thickness and particle size. Finally, in Chapter V, I make and measure layered materials containing silver films and silver nanoparticles, and pinpoint the geometric properties necessary to attain a 532nm resonance.

Throughout this work, we will see how easily our questions are posed yet how elusive answers can be. Experimental complications and caveats abound. We will emerge with an appreciation for the craft of optical design at the nanoscale, and pose new questions regarding the design and application of tunable plasmonic systems. In the following chapter, we will review the physics behind tunable coupling to build a foundation for this work.

CHAPTER II

BACKGROUND

In this chapter I lay out the physical underpinnings of the interaction of light with metallic nanoparticles. I begin by reviewing the optical response of metals. Then, I describe the scattering and absorption by small particles in the quasistatic limit, and more generally by discussing the Mie theory. Moving beyond single particles, I discuss particle ensembles and the interactions between particles and substrates.

2.1. Permittivity of metals: the Drude model

In the Drude model, the conductivity of metals is understood by assuming the material is composed of a gas of free electrons moving within an immobile background of positively charged ions.[21] Electrons are assumed not to interact significantly with either the ionic background or with one another (these are the free electron and independent electron approximations). We also assume that the material has a relative magnetic permeability $\mu = 1$.

When an incident time-varying electromagnetic field is incident upon the material, electrons follow the oscillating field, relaxing with a characteristic time constant τ, which is inversely proportional to the rate γ of momentum-dissipating collisions whose origin is unspecified.[1]

The equation of motion for the oscillating charges is

$$m(\frac{d^2x}{d^2t} + \gamma\frac{dx}{dt} + \omega_0 x) = -eE(x,t), \tag{2.1}$$

---

[1]Typical values at room temperature are $\tau \sim 10^{-14}$ and $\gamma \sim 100THz$

where $\gamma = 1/\tau$ is the damping constant, ω_0 is the binding frequency, and the time dependence of the field is harmonic: $E(t) = E_0 e^{-i\omega t}$.

The dipole moments of all electrons in an isotropic medium conspire to produce the overall induced polarization $P = \epsilon_o \chi_e E$ where χ_e is the electric susceptibility. The definition of the permittivity ϵ comes from considering the electric displacement $D = \epsilon_0 E + P = \epsilon_o(1 + \chi_e)E = \epsilon E$.

The single-electron dipole moment is given by

$$p = -ex = \frac{e^2}{m}(\omega_0^2 - \omega^2 - i\omega\gamma)^{-1}E. \tag{2.2}$$

By adding the contributions of all of the electrons in the material with binding frequencies ω_i, damping constants γ_i, and electron densities n_i, we find the relative permittivity:

$$\frac{\epsilon(\omega)}{\epsilon_0} = 1 + \frac{e^2}{\epsilon_0 m}\sum_i n_i(\omega_i^2 - \omega^2 - i\omega\gamma_i)^{-1}. \tag{2.3}$$

We can separate the permittivity into a bound electron term and a free electron term, considering a number density N of free electrons in the material to have $\omega_0 = 0$ and effective mass m^*.[22] The bound electron term takes a Lorentz oscillator form to account for interband transitions.[23] We arrive at the Drude model of the permittivity:

$$\frac{\epsilon(\omega)}{\epsilon_0} = \epsilon_b(\omega) + i\frac{Ne^2}{\epsilon_0 m^* \omega(\gamma_0 - i\omega)}. \tag{2.4}$$

If the damping γ_0 is small compared to the frequency ω of the incident field, the permittivity is approximated by

$$\epsilon(\omega) = \epsilon_b(\omega) - \frac{\omega_p^2}{\omega^2}, \tag{2.5}$$

8

where $\omega_p^2 = \frac{Ne^2}{\epsilon_0 m^*}$ is the bulk plasma frequency.

The plasma frequency of noble metals is typically in the ultraviolet. Below the plasma frequency, free electrons readily respond to the oscillation. The varying field is screened by the electron response, thus the field penetrates only a short distance into the metal, and light is reflected. In this region, the real permittivity ϵ' is negative, and the wave number is imaginary. For noble metals, this occurs through the visible range and gives rise to our experience of metals as "shiny." Above the plasma frequency, the bound term dominates, ϵ' is positive, and the metal can transmit; this occurs for noble metals in the UV and is gives rise to their "ultraviolet transparency." The precise location of the observed plasma frequency, when $\epsilon' = 0$, depends on the interband transitions. For silver, the bulk plasma frequency is 9.2 eV (wavelength 135nm). However, the positive contribution from $\epsilon_b(\omega)$ (stemming from the interband transitions) shifts the measured zero of ϵ' to 3.9eV (318nm).[24] The real and imaginary components of the permittivity of silver, as measured by Johnson and Christy,[25] are shown in Fig. 2.1.
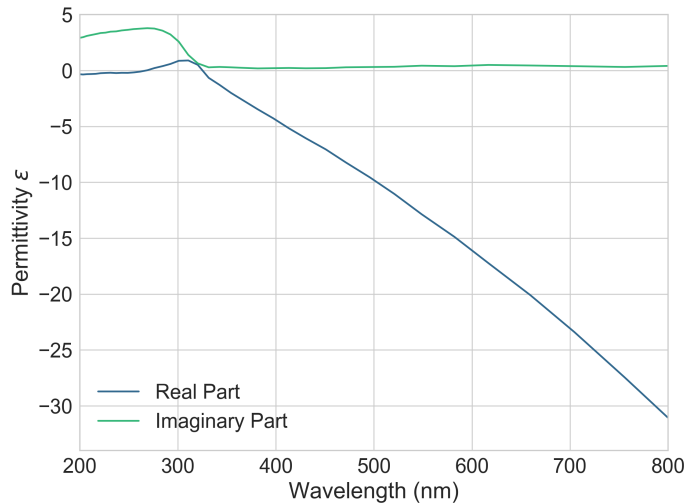
FIGURE 2.1. Permittivity of silver.
Tabulated experimental values by Johnson and Christy.[25]

9

2.2. Localized surface plasmons

Localized surface plasmon polaritons (LSPs) are resonant electromagnetic surface modes supported on nanoparticles or within nanovoids. When a harmonic incident electromagnetic field is incident upon small particles ($d \ll \lambda$), the particles experience an electric field which is constant across their surface (the quasistatic approximation). In this case, the optical response is characterized by a complex polarizability

$$\alpha = 4\pi a^3 \frac{\epsilon - \epsilon_m}{\epsilon + 2\epsilon_m}, \tag{2.6}$$

where a is the particle radius, ϵ is the particle permittivity, and ϵ_m is the permittivity of its embedding medium.[26] This approximation is good for small or slowly varying ϵ, which as we have seen holds for silver at wavelengths longer than its interband transitions.
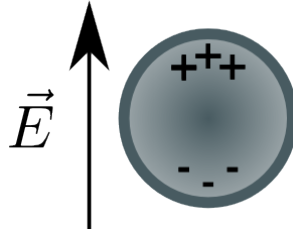
FIGURE 2.2. Localized surface plasmon polariton excitation.

The polarizability has a resonance when the Fröhlich condition, $Re[\epsilon] = -2\epsilon_m$, is met. The resonant mode is called the dipolar surface plasmon. For a Drude metal in air, the dipolar resonance occurs at the frequency $\omega = \omega_p/\sqrt{3}$ where $\omega_p = \frac{ne^2}{\epsilon_0 m}$ is the bulk plasma frequency of the conductor. By combining the Fröhlich condition and the real part of the permittivity (setting the $\epsilon_b = 1$), we find that the frequency scales with ϵ_m as

$$\omega^2 = \frac{\omega_p^2}{1 + 2\epsilon_m} - \gamma^2, \tag{2.7}$$

10

which shows that the resonance redshifts as ϵ_m increases. Thus metal nanoparticles are useful for detecting changes in the refractive index of their surroundings.

2.3. Mie theory

It is helpful to visualize the resonance of metallic nanoparticles using the LSP description, but this applies only in the quasistatic approximation. We can generalize beyond the quasistatic approximation by considering the LSP description as a special case of the Mie theory for particle scattering and absorption.

Mie theory is both a conceptually elegant and computationally efficient treatment of absorption and scattering by small particles. It is an exact solution to Maxwell's equations. The power of Mie's approach is that it separates the problem into two parts: first, the solution of the electrodynamic problem, solved by first principles; second, the phenomenological description of the material response via the permittivity. This conceptual separation allows the theory to be applied in a wide variety of circumstances, because many complicating factors can be incorporated by adopting different expressions and approximations for the permittivity.[27] Additionally, the spherical harmonics lead to an eigenmode description, allowing interactions between excitations to be viewed in the mode hybridization picture.

In this section I discuss the electrodynamic solutions for scattering and absorption by spherical particles, the relationship of the Mie solutions to common physical observables, modifications of the permittivity used to treat effects of particle size and inhomogeneous environments, and computational approaches to modeling both simple and more general problems.

Exact classical electrodynamic problem

The geometry of the electrodynamic problem, shown in Fig. 2.3, is as follows: a linearly polarized plane wave is incident on a sphere with radius a. The incident electric and magnetic fields are expanded into an infinite series of vector spherical harmonics. Several factors determine the expansion coefficients and choice of vector spherical harmonics for the scattered fields and the fields inside the sphere: the spherical expansion of the incident field, the orthogonality of the vector harmonics, finiteness at the origin of the sphere, and the boundary conditions at the sphere interface.
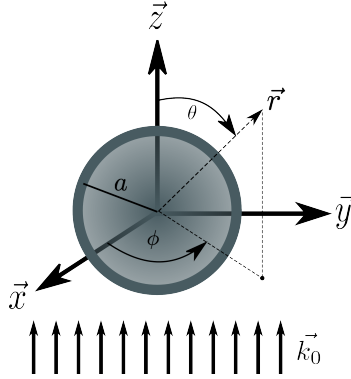
FIGURE 2.3. Mie scattering geometry.

Normal modes

The expansion of the scattered fields is given by

$$E_s = \sum_{n=1}^{\infty} E_n(i a_n \vec{N}_{e1n}^{(3)} - b_n \vec{M}_{o1n}^{(3)}) \tag{2.8}$$

and

$$H_s = \frac{k}{\omega \mu} \sum_{n=1}^{\infty} E_n(i b_n \vec{N}_{o1n}^{(3)} + a_n \vec{M}_{e1n}^{(3)}), \tag{2.9}$$

where e and o are the even and odd forms of the vector spherical harmonics, and the superscript (3) indicates that the radial dependence of the generating functions for those vector spherical harmonics is from the first spherical Hankel function $h_n^{(1)}$, whose form in the far-field corresponds to an outgoing wave.

The vector spherical harmonics $\vec{M}_n$ and $\vec{N}_n$ are the electromagnetic normal modes for spherical particles. Full expressions for these may be found in Bohren and Huffman.[24] In general, the scattered field is a superposition of these modes, weighted by the scattering coefficents a_n and b_n. There are two types of normal modes for each order n. One has no radial magnetic component; these modes correspond to plasmon resonances in metal spheres, so we call these the electric modes. The other has no radial electric field component; these modes correspond to eddy currents in metal spheres, so we call these the magnetic modes.[27] The "natural frequencies" for a scattered field described purely by either a_n or b_n alone are in general complex, so these are often called "virtual modes." However, sometimes the imaginary part of a virtual mode's frequency is negligible compared to the real part, and thus the real parts are approximately equal to the real frequencies of the incident electromagnetic waves. For example, the particle dipole is dominated by a_1. The summation index n gives the order of the partial wave: 1 is the dipole, 2 is the quadrupole, etc.

The angle-dependent functions in the vector spherical harmonics (which we will not examine closely here) have a notable consequence: the higher order angular functions have alternating positive and negative components in the backscattering direction, but always have positive components in the forward scattering direction. As a result, larger spheres scatter primarily in the forward rather than backward direction. This, in part, is the reason sunsets are red: the larger particles scatter the

red colors of sunlight primarily forward, while the smaller particles scatter the blue colors in all directions.

Scattering coefficients

So far, the electrodynamic description has not involved the permittivity of the particle and its surroundings explicitly. These permittivities enter into the solution via the scattering coefficients a_n and b_n. Assuming the permeabilities of the particle and surrounding medium are identical, a_n and b_n are given by

$$a_n = \frac{m\psi_n(mx)\psi_n'(x) - \psi_n'(mx)\psi_n(x)}{m\psi_n(mx)\eta_n'(x) - \psi_n'(mx)\eta_n(x)} \tag{2.10}$$

and

$$b_n = \frac{\psi_n(mx)\psi_n'(x) - m\psi_n'(mx)\psi_n(x)}{\psi_n(mx)\eta_n'(x) - m\psi_n'(mx)\eta_n(x)} \tag{2.11}$$

where $x = ka$ is the size parameter and $m = n_p/n_m$ is the relative refractive index (the ratio of complex particle index n_p and real surrounding medium index n_m). The functions $\psi_n(\rho) = \rho j_n(\rho)$ and $\eta_n(\rho) = \rho h_n^{(1)}(\rho)$ are Riccati-Bessel cylindrical functions, and the prime indicates differentiation with respect to the argument. Note that a_n and b_n vanish as m approaches unity. This is reassuring: no particle, no scattering.

Scattering and extinction cross sections

The cross sections arise from energy conservation. They are given by:

$$\sigma_{scat} = \frac{2\pi a^2}{x^2} \sum_{n=1}^{\infty} (2n+1)(|a_n|^2 + |b_n|^2), \tag{2.12}$$

$$\sigma_{ext} = \frac{2\pi a^2}{x^2} Re \sum_{n=1}^{\infty} (2n+1)(a_n + b_n), \tag{2.13}$$

14

and

$$\sigma_{abs} = \sigma_{ext} - \sigma_{sca}. \tag{2.14}$$

The cross sections are calculated by first calculating the coefficients a_n and b_n using recurrence relations of the Bessel functions. It is common to normalize a particle's optical cross section by its physical cross section: this is the scattering or absorption efficiency. These efficiencies can be greater than one.

It is worth reflecting on the meaning of an efficiency greater than one, because this implies that particles can absorb more than the light incident upon them. This result may seem strangely unphysical, until one considers that metals perturb the incident electromagnetic field. The field lines of the Poynting vector are deflected by and converge near the sphere, and therefore the sphere absorbs light which would have simply passed by in the geometric optics picture.[24] Thus there is nothing inherently unphysical about an absorption efficiency greater than unity, so long as one remembers that the intuitively-familiar geometric optics is just an approximation of a richer theory.

We can likewise apply the wave perspective to reflection and refraction, the geometric optical behavior of bulk matter. According to the Ewald-Oseen extinction theorem, an incident wave is completely extinguished inside a medium. The superposition of secondary scattered waves generates reflected and refracted beams. Thus, reflection and refraction are scattering phenomena at their core.

<u>Permittivities</u>

With the electrodynamic problem fully specified, we are now confronted with the material problem. The question is what form of the permittivity to choose for the particle and its surroundings. The surroundings are simple: generally a particle

15

is embedded within some homogeneous material (for example, air or water), which is well-described by its bulk permittivity. In high permittivity media, the particle polarization is reduced because the medium polarizes as well. This decreases the surface charge and thus the restoring force at resonance, redshifting the resonant frequency. This is why particles are sensitive to sub-wavelength changes of the permittivity in their environment, and leads to many applications in refractive index sensing and monitoring. Inhomogeneous permittivity environments, such as mixed matrices or substrates, can be treated to first order by choosing an averaged permittivity based on the permittivities and volume fractions of each component.[27]

For particles, the bulk permittivity is often a reasonable starting place; a good rule of thumb is that bulk values are appropriate for bodies larger than about 10nm diameter.[24] For smaller particles, size-dependent effects emerge as various characteristic length scales in the material problem (e.g., electron mean free path or Fermi wavelength) become commensurate with particle size. These types of size effects are called intrinsic, and reflect the failure of bulk permittivities to describe very small particles.

Intrinsic size effects arising from various length scales

The first characteristic length scale, the electron mean free path, describes the average distance free electrons travel in a material prior to collision; in silver, this is 52nm. For small particles, the electron mean free path becomes constrained by the particle boundary.[24] Additional collisions with the particle surface must then be included in the Drude model damping constant, and because collisions will be proportional to the particle radius, the permittivity winds up with a size dependence

16

proportional to $1/R$. The $1/R$ dependence leads to broadened absorption spectra with lower peak heights as particles become smaller.[27]

The second characteristic length scale, the Fermi wavelength of the electron, softens the abrupt interface between the imagined metal particle and dielectric environment. This "spill-out" or "smear-out" of charge density at the interface lowers the energy of the surface plasmon peaks for small particles, because the mean electron density averaged over the particle volume is decreased. The resonant wavelength of silver particles may deviate from Mie theory for particles smaller than 5nm diameter, and the width of the resonance may be affected for particles smaller than 10nm.[27]

A more rigorous description of this "smear-out" effect is given by the hydrodynamic model of material response. The response is called spatially dispersive or nonlocal, meaning that the polarization at a given spatial point is influenced by the microscopic interactions over a volume surrounding the point. These interactions are accounted for by treating the electrons as a fluid, which is described by a charge density, fluid velocity, and pressure. The electron pressure term accounts for both Pauli exclusion and the Coulomb interactions between electrons. The hydrodynamic model doesn't account for specific quantum effects such as tunneling, but recently some groups have made an effort to include quantum corrections.[28–30]

While the classical model of the electron response assumes that charges occupy an infinitesimal sliver at surfaces, the hydrodynamic model allows the charge density to spread out. The degree of this spread is described by a nonlocality parameter β, proportional to the Fermi velocity. Depending on whether the charge density tends to spread further into the bulk region inside the particle or into the region surrounding the particle, the resonances may either blueshift or redshift, but the typical effect for a single particle, particle dimer, or nanoparticle-film system is to blueshift the

plasmon resonance from its local counterpart, and to reduce the field enhancement factor.[31] The most dramatic plasmon resonance shifts occur for gap distances below 5nm,[32, 33] but the enhancement factor can be reduced at larger gap sizes (such as 10–70nm), before a noticeable plasmon shift occurs.[34]

Analytically, the hydrodynamic model involves treating the longitudinal modes as well as transverse modes, and thus it introduces a new boundary condition.[31] This means that the Mie problem is completely reformulated at the geometric level, making it inconvenient to incorporate the hydrodynamic model into extended Mie theories.[35, 36] Other numerical implementations are also challenging, because the problem involves spatial variations on the angstrom scale but also requires a domain size on par with the wavelength of the light. For this reason, it is typical to use finite element or finite difference methods which allow for nonuniform meshing.

The hydrodynamic model usually results in small shifts of resonant wavelengths. We describe it here to acknowledge the breadth of theoretical and computational options for the problem of scattering and absorption by small particles, but will focus on the classical Mie theory in this dissertation in an effort to glean as much physical insight as possible from the normal mode picture.

Extrinsic size effects

Larger particles also have size-dependent response, but not as a consequence of inappropriately assuming bulk permittivities. For particles with radii larger than their skin depths, the interior of the particle will be shielded from incident fields. As a result, the quasistatic approximation no longer holds for radii between about 10–100nm (when the size parameter $x = ka$ no longer obeys $x << 1$). Being an electrodynamic description, Mie theory accounts for this retardation of

the electromagnetic wave across the particle surface. Retardation is an example of an extrinsic size effect; that is, it arises only because of the relationship between the particle size and the light wavelength, and requires no adjustments to the permittivity.

The main consequence of retardation is that the dipole absorption peak redshifts and broadens for larger radii. As particles become large, the quadrupole resonance comes into play and even can overcome the dipole contribution at a certain size. Octopole resonances emerge for even larger particles and the dipole resonance can become negligible. These effects can each be seen in Fig 2.4. Even as the absorption spectra evolve, the dipole can still dominate the extinction cross section because the dipolar scattering dominates.[27]
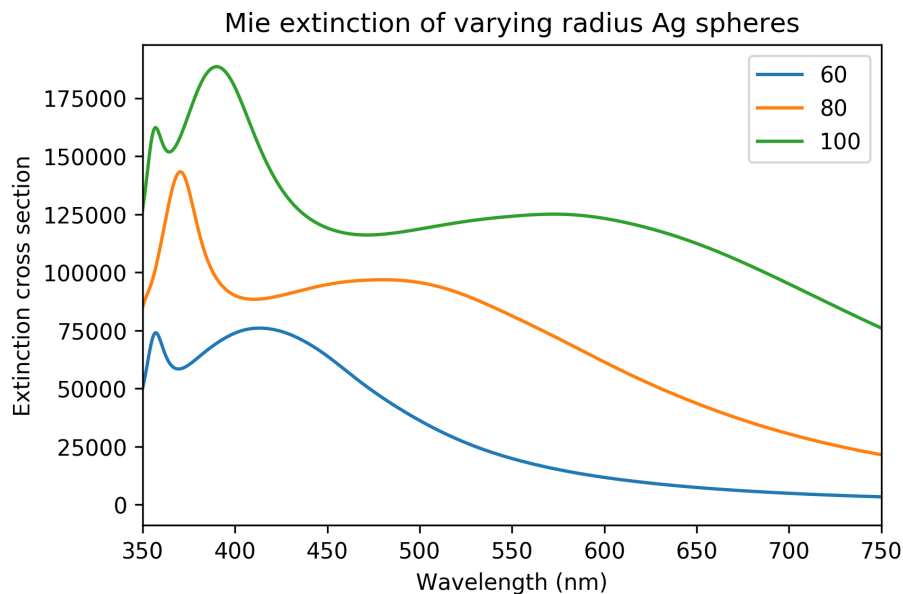
FIGURE 2.4. Mie extinction spectra of silver spheres with varying sizes. As particle radius becomes larger, the longer-wavelength dipole peak and shorter-wavelength quadrupole peak each redshift and broaden. Note the emergence of an octopole peak for the 100nm radius particles.

The bulk permittivity is perfectly usable for particles large enough for extrinsic size effects to arise. However, it may be necessary to adjust permittivity in order to account for constraints imposed by small dimensions other than the particle radius; for example, in geometries containing nanoscale gaps or sharp features. In those cases, one may need to account for nonlocal effects despite the large sizes of the bodies in the system.

So far, we have considered only spherical particles. However, nanoparticles in the laboratory are often only approximately spherical. It is important to understand the effects of deviations from sphericity in order to make sense of experimental results. Ellipsoids are a natural starting place, both because spheres are a special case and because the full spectrum of ellipsoidal shapes is broad, ranging from discs to needles.

Because Mie theory is built on spherical symmetry, it is necessary to return to the quasistatic approximation and construct shape-dependent polarizabilities for ellipsoids. Though this comes at the expense of including retardation effects, it does help to build an intuition for how trends in particle shape may affect observed spectra.

As we move from spheres to ellipsoids, axial symmetries drop away, degeneracy is lifted, and eigenmodes can be calculated for each axis. The particle shape is described by depolarization factors L_i with $i = a, b, c$ describing each axis. Two of these factors are independent, while the third is constrained by a sum rule $\sum L_i = 1$. These depolarization factors also determine the electric polarizability along the principal axes of the ellipsoid. The depolarization factors occur in the denominator of α and thus result in different resonances along each axis for an ellipsoid.

The orientation of the particle with respect to the light polarization determines the strengths of each mode. Both redshifts and blueshifts relative to the spherical

modes can result depending on the particle aspect ratio. For a collection of randomly oriented identical ellipsoids, the distinct modes can produce a more structured spectrum. However, if instead there are a distribution of eccentricities, this structure can wash out into a broad multipeak spectrum.

To illustrate, it is helpful to look at the absorption cross sections averaged over orientations for different shapes:

$$< C_{abs} >_{sphere} = \frac{kv}{3} [\frac{27}{(\epsilon' + 2)^2 + \epsilon''^2}] \epsilon'', \tag{2.15}$$

$$< C_{abs} >_{needle} = \frac{kv}{3} [\frac{8}{(\epsilon' + 1)^2 + \epsilon''^2} + 1] \epsilon'', \tag{2.16}$$

and

$$< C_{abs} >_{disk} = \frac{kv}{3} [\frac{1}{\epsilon'^2 + \epsilon''^2} + 2] \epsilon'', \tag{2.17}$$

where ϵ is the relative permittivity of the particle and its surrounding medium, k is the wave number in the medium, and v is the volume of the particle. For negative ϵ'; e.g. in metals, there can be large differences in the magnitudes of these cross sections. Consider the magnitudes of the prefactor (the term in brackets) for spheres, needles, and disks of equivalent volume. In silver at 425nm, the ratio between the prefactors is 1.68 : 1.32 : 2.03. At 500nm, the ratio is 0.42 : 1.10 : 2.01. In both cases the scattering cross sections are quite different depending on shape. Silver is more sensitive to shape effects than gold because its ϵ'' is smaller than gold, and thus its cross sections are affected more by changing shape.

21

Computational approaches

Because Mie theory is applicable to many fields, and because the solution is relatively easy to code (after all, Gustav Mie performed these calculations without a computer), there are a multitude of software packages written by scientists in a variety of languages. Many are based on the BHMIE program provided in Bohren and Huffman.[24] In this dissertation, I use the Python packages MiePy ([37]) and Py_GMM ([38]) to solve simple Mie and generalized Mie problems (for particle aggregates).

2.4. Particle ensembles

While Mie theory is helpful for analyzing the behavior of individual particles, it does not tell us how to treat particle ensembles. Ensembles will often have spectra different from their individual components. There are several main causes: first, polydispersity of spherical particles; second, deviations of particles from sphericity, and third, particle aggregation. We have already discussed deviations from sphericity. In this section, we examine the nature of coupling between metal particles and describe how normal modes hybridize in a prototypical two particle aggregate. Then, we consider the effects of aggregation in samples of uniform spheres. Finally, we comment on how to calculate optical spectra in samples containing aggregates, which will incidentally also solve the problem of polydispersity.

When particles within ensembles aggregate, they may interact via Coulomb forces. For this reason, in order to understand the behaviors of aggregates, it is helpful to consider the problem of particles interacting in their near field as coupled harmonic oscillators. Then, we can better understand specific aggregate configurations which

will arise in this dissertation and build up a set of heuristics that will prove to be helpful for qualitative interpretation of optical spectra. We then consider the arrangement of these aggregates in order to appreciate the complications that can arise due to the proximity of aggregates to one another. Finally, we can consider the polydispersity of the individual particle constituents and how that may impact the various types of aggregates and classifications of aggregated matter.

Mode hybridization in particle dimers

A hybridized coupled mode response arises from interactions between individual plasmonic modes. Individual resonances, when coupled, split into two new resonances which have different energies than either of the individual resonances. The magnitude of this splitting depends on the energetic overlap (detuning) of the individual modes; greater spectral overlap (small detuning) leads to larger splittings.[39] The coupling mechanism in plasmonic systems is the Coulomb near-field interaction. Coupling is thus stronger when particles are in close proximity.

To illustrate a simple coupled system, we investigate a particle homodimer; that is, two closely spaced particles of equivalent shape and size. For linear polarizations, the dipolar plasmon mode can split into 1) the low energy ("bonding") mode which contains end-to-end aligned dipoles, producing a large induced dipole and strong far-field coupling, and 2) the high energy ("antibonding") mode in which dipoles point in the opposite direction, resulting in a small or zero induced dipole. These modes are illustrated in Fig. 2.5. Dipolar modes are radiative, so the lack of the net dipole in the antibonding mode means this is a dark mode - it does not scatter (at least appreciably) to the far field and is thus not experimentally detected.
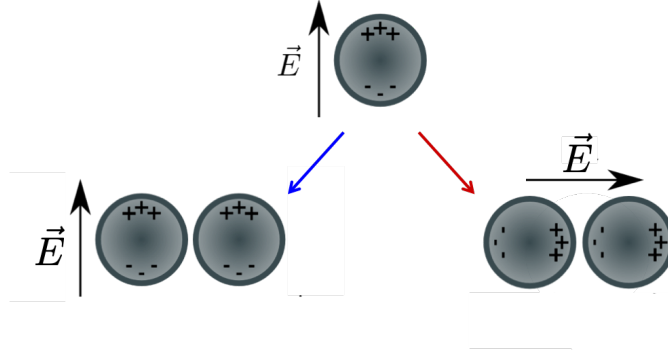
FIGURE 2.5. Polarization-dependent bonding modes for plasmonic dimers. The transverse (antibonding) mode (left) blueshifts while the longitudinal (bonding) mode (right) redshifts relative to the single particle resonance.

Hybridized spectra are sensitive to changing particle size, spacing, and orientation. This is illustrated in Fig. 2.6 for a system of orientationally-averaged homodimers, which indicate larger peak splitting for increasing R/d. In coupled sphere dimers with controllable spacing, this scaling of the resonance has been exploited to develop "plasmon rulers" which can measure distance at the nanoscale.[18] For dimers consisting of nonspherical particles (such as ellipsoids or nanorods), orientation effects are pronounced; both blueshifted or redshifted spectra occur for particle pairs in different relative orientations, analogously to coupling between excitons on chromophores (J and H aggregates).[40]

Ensemble configurations

The behavior of particle ensembles depends on the typical dimension d of the structures involved relative to the incident wavelength. When $(d/\lambda) \leq 10^{-2}$, the material can be considered to be relatively homogeneous, and effective medium theories may be used to find an average permittivity describing the system. Above that limit (which is equivalent to the quasistatic approximation), scattering becomes important. Particles then may "feel" the fields scattered from nearby particles. Waves

scattered from many particles may interfere, and the details of the interference will depend on the precise topology of particles on the surface.

(a) Homodimer geometry

(b) Absorption spectra for quasistatic homodimer
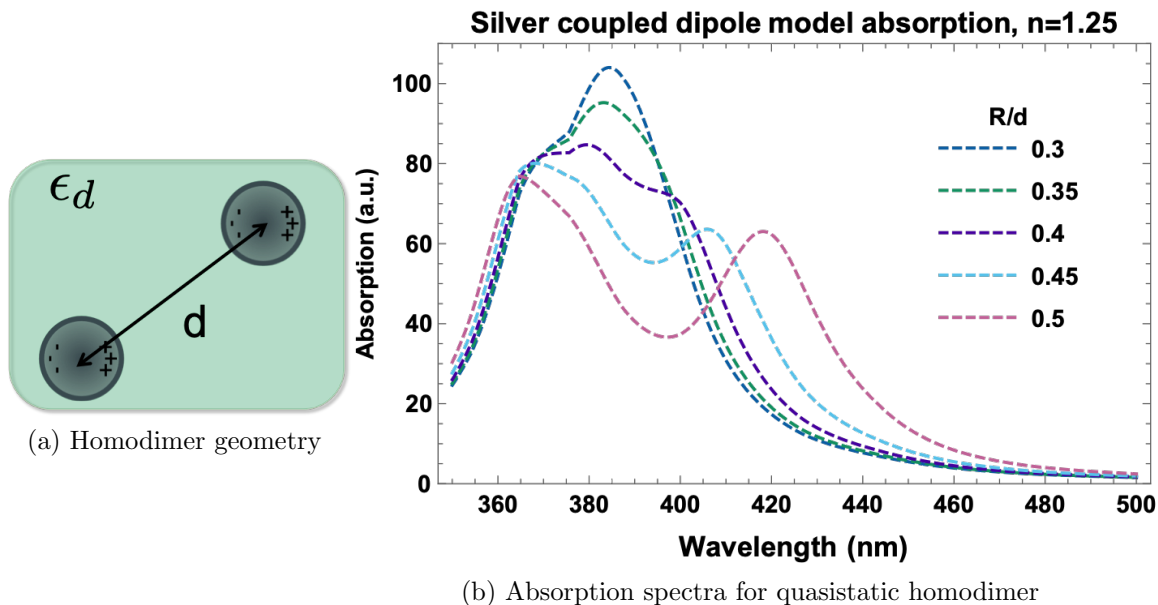
FIGURE 2.6. Mode splitting in plasmon homodimers.
Silver homodimers with radii R and center-to-center separation d are embedded in a uniform environment with $n = \sqrt{\epsilon_d} = 1.25$. Spectra are calculated in the quasistatic approximation with three dimensional orientational averaging following Kreibig and Vollmer.[27] Peak splitting increases for increasing R/d.

Ensembles of particles may configure themselves on surfaces in a variety of ways, ranging from regular arrangements to complete statistical disorder. Ensembles are generally described by an average volume filling factor $f = V_{particles}/V_{sample}$. However, if the microscopic configurations cause local deviations of the filling fraction relative to the overall sample, then the utility of f will be limited. According to Oseen, the coherent geometric optical properties (such as the specular reflectance) are proportional to f^2, while the incoherent diffuse scatter depends on the local deviations $(f_{loc} - f)$. There is no hard and fast rule to decide when to consider particles as independent scatterers. Mischchenko *et al.* suggest that particles are

independent if their size is on the order of the wavelength and if their separation satisfies $d > 4R$.[41] Otherwise, one must consider the multiply scattered (or diffuse) component of the incident radiation appropriately.

Aggregate configurations

Kreibig and Vollmer classify particle ensembles based on how particles cluster into aggregates and how densely the resulting aggregates are packed.[27] These classifications are shown in Fig. 2.7. Discrete aggregate shapes can be useful to consider when modeling random collections of small aggregates. Considering the behavior of heterodimers, chains, ordered arrays, and compact aggregates can produce some rules of thumb with which to understand assemblies in ensembles.
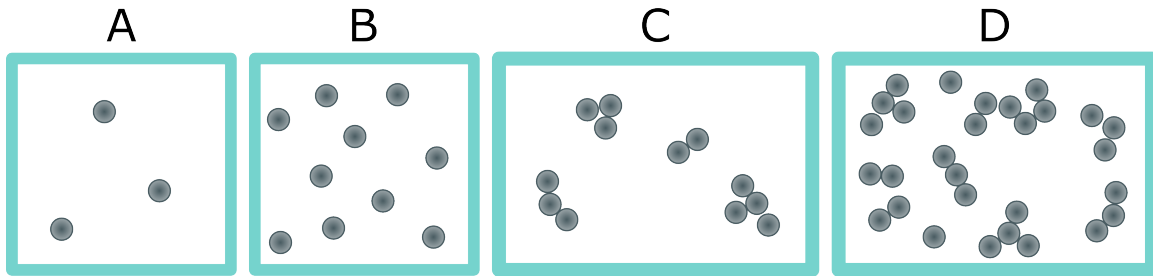
FIGURE 2.7. Classifications of aggregated particles.
(A/B): Individual particles are sparsely (A) or densely (B) arranged and in full statistical disorder with no aggregation. Effective media are often sufficient to describe these cases.
(C): Particles cluster into aggregates, but there is no interaction between aggregates. Both exact and statistical approaches may be used to calculate ensemble cross sections.
(D): Particles cluster into densely packed aggregates, which interact with one another. A spectral effective medium description may be useful if individual aggregates can be treated in the quasistatic approximation.

Heterodimers

We have already discussed the simple homodimer configuration. A step beyond this is the heterodimer, in which one particle has a different size, shape, or material than the other. Coupled dimers of the same material and size (homodimers) have dark antibonding modes, but heterodimers formed of particles of different material and/or different size can make those modes bright.[42]

Chains

Dimer coupling effects are amplified by increasing the number of particles that can affect each neighbor. For example, in chains of spherical particles, the individual particle modes again split into longitudinal and transverse modes (Fig. 2.8) depending on how the incident polarization is aligned relative to the chain.[43] If particle diameters are a quarter of the incident wavelength, these can further split into in-phase and opposite-phase modes. As more particles are added to the chain, the magnitude of mode splitting increases (Fig. 2.9) up to a certain point, beyond which the magnitude saturates as subsequent particles cannot be impacted by the near-field of their farthest neighbors.[26]

(a) Longitudinal modes redshift.

(b) Transverse modes blueshift.
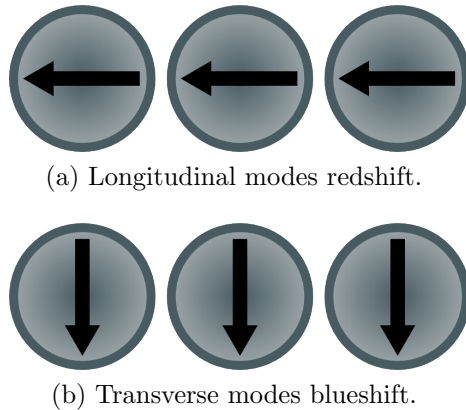
FIGURE 2.8. Schematic of longitudinal and transverse modes in particle chains.
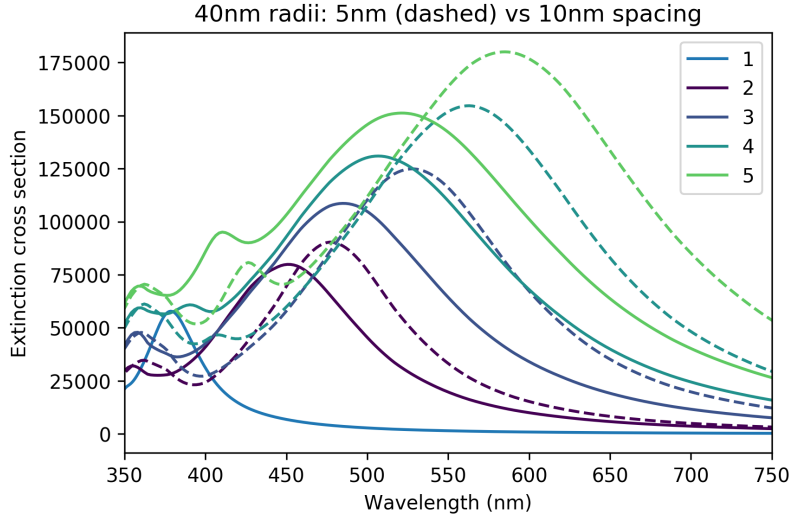
FIGURE 2.9. Mie extinction spectra for chains of 40nm radius silver particles. Peak splitting increases as the number of particles in the chain (indicated in the legend) increases. Chains with edge-to-edge spacings of 5nm (dashed curves) are redshifted further than those with spacings of 10nm (solid curves).

Ordered arrays

A regular array is another way to increase the number of particle-particle interactions, enabling narrow collective resonances to emerge from dipolar[44] or quadrupolar[45] mode coupling. Various degrees of freedom (particle size, interparticle spacing, and relative orientation) may be manipulated to change the frequency and width of the plasmon line shape. Generally, fine control over these degrees of freedom is accomplished by fabricating arrays using lithographic or ordered assembly approaches.

Compact aggregates

Compact (non-linear) aggregates such as trimers, quadruplets, quintuplets, and other shapes don't result in a decomposition into longitudinal and transverse dipolar modes; instead, they result in multiple modes which are sometimes excited

simultaneously and are therefore not easy to resolve. Sometimes peaks stemming from different modes can be separated in measurements by changing the angle and polarization of the incident light.

Highly symmetric aggregates may act as small ordered arrays. In such structures, interference between different modes can lead to Fano resonances, which are particularly useful in sensing due to the high figures of merit resulting from narrow line shapes.[46] The ability to tailor the line shapes of hybridized modes which stem from specific aggregate shapes has led to the concept of plasmonic "meta-atoms" or "metasurfaces" whose effective permittivities and permeabilities may be manipulated to produce highly controllable response.[47] This concept can be extended beyond the solid state, since three-dimensional aggregates whose optical properties are independent of orientation may be dispersed in liquids or amorphous solids.[48]

Rules of thumb

With these examples under our belt, we can enumerate a few rules of thumb for predicting the influence of various aggregate types on optical spectra. In general, peak splitting is largest for chains, and smaller for more compact structures. Compact, nearly spherical aggregates can have a single peak structure similar to a spherical particle of equal size. The dipole mode contributes most to peak splitting, but higher multipoles become more influential for larger particle sizes.

Analytical and numerical approaches

There are several approaches to calculating the optical spectra of different aggregates. We have already discussed particle dimer coupling under the quasistatic

approximation. However, it is known that this approximation can underestimate peak shifts for dimers.[49] Therefore, we want to extend our understanding of coupling to include retardation effects and multipoles.

The generalized Mie theory (GMT) is used to calculate the response of small aggregates beyond the quasistatic approximation. First, the particle polarizability α_i is calculated using Mie theory, including multipoles and retardation, and allowing for different sizes and materials for all particles. The aggregate shapes and sizes are set by the coordinates of each particle (which are not allowed to touch or overlap). Coupling fields between particles are given by the retarded near-field solutions of scattered Mie fields from all other particles. The spectra of nonlinear "prototypical" particle aggregates consisting of particles on square grids have been calculated systematically using the generalized Mie theory and correlated with optical measurements of randomly deposited particles.[43, 50]

The GMT approach can be combined with morphological statistics to calculate optical spectra in cases when aggregate are not too closely spaced (e.g. Case C in Fig. 2.7). The procedure again begins by calculating the α_i for various aggregates in the Mie theory. These can be added with weightings based on the distribution of aggregate shapes and sizes in the overall sample, which can be gleaned from electron microscope images. Such a statistical approach collapses what would otherwise be a large numerical problem into a set of small problems. When sufficient morphological information is available, this approach may be quite powerful in interpreting optical spectra.

Size-distributed Mie theory

The statistical approach to treating particle aggregates also treats the problem of polydispersity. In this case, the overall cross section of the sample is calculated by weighting the contribution of each particle according to its abundance; that is, averaging over the particle size distribution. In general, as the FWHM of the size distribution increases, the structure of distinct multipoles in optical spectra are smeared out. For small particles, the dipole mode will dominate the resulting broadened spectra; for large particles, the quadrupole mode will dominate. This approach is called the size-distributed Mie theory and has been used to solve the "inverse problem:" estimating particle size and shape given their optical spectra.[51, 52] If the size distribution is particularly broad, calculating spectra in this way may prove to be too time consuming.[41]

For narrow size distributions, polydispersity can be partially accounted for by calculating a single extinction spectrum for the mean particle size. For $R << \lambda$, absorption is proportional to $(kR)^3/k^2$, and scattering to $(kR)^6/k^2$. So the broad size distributions for extinction are dominated by the largest particles (which are heavily scattering). Thus the appropriate mean size for extinction spectra should be obtained by averaging R^3 if absorption dominates (small aggregates) but by averaging R^6 if scattering dominates (large aggregates).[27]

By considering how particles interact with one another within aggregates and how aggregates interact in larger configurations, we can interpret the spectra of a wide variety of sample geometries. The quasistatic approximation, generalized Mie theory, and size- or shape-distributed Mie theory are good examples of numerical methods which are closely linked to sample morphology. They can thus provide excellent phenomenological insight and help unravel the contributions of different particle

shapes and sizes, and different modes within those particles, to the optical spectra. Additional approaches such as a semianalytical multipolar coupling approach[45], or a polar or singular representation of coupled multipolar resonances[53] yield similar insights, but are more complicated to implement. Finally, finite element methods produce results which are very faithful to experiment, but this faithfulness can come at the expense of providing phenomenological insight. For this reason, we primarily use the generalized Mie theory and size-distributed Mie theory in this dissertation.

2.5. Particle-substrate interactions

The presence of a substrate, whether metal or dielectric, can also affect the particle plasmon resonance. For a particle otherwise surrounded by a uniform permittivity, a nearby substrate whose permittivity differs from the homogeneous surroundings will perturb the particle's dielectric environment and cause its resonance to change and shift in several ways. This substrate effect can be understood using several theoretical frameworks, and the changes in resonance frequencies calculated using analytic but approximate effective medium approaches, or numerically but exactly using a variety of computational approaches. We discuss these frameworks below.

Effective medium approach

The effective medium approach is a helpful, albeit approximate, way to understand interactions with dielectric substrates. Typically, a substrate will have a higher index than the surroundings. This increases the effective index of the particle environment and leads to a redshift of the plasmon resonance. A simple treatment is therefore to replace the permittivity of the particle environment with a homogeneous

permittivity, averaging between the substrate and surrounding medium:

$$\epsilon_e \approx 1/2(\epsilon_m + \epsilon_s) \tag{2.18}$$

where the subscripts m and s refer to the embedding and substrate media, respectively. It is easy to add one more step of sophistication by noticing that the particle is not embedded half within the substrate, but may be more or less surrounded by the substrate material due to the substrate's surface roughness. This suggests a weighted effective index approach:

$$n_{eff} = \xi * n_m + (1 - \xi) * n_s \tag{2.19}$$

where ξ is an empirically-determined weighting factor.[54] These simple effective index approximations, though not quantitatively precise, leverage the Mie theory's conceptual separation of permittivity from the exact electrodynamic solution, are simple to incorporate into calculations, and can be qualitatively helpful in interpreting spectra.

Image charge approximation

The effects of either dielectric or metal substrates may also be understood through an image charge approximation. The particle plasmon interacts with its own image of surface charges, screened by a factor of $(\epsilon_s - 1)/(\epsilon_s + 1)$.[55] The image charge and particle interact via a Coulomb potential, redshifting the overall resonance relative to the independent particle. As permittivity increases, the image interaction and thus redshift increase, scaling linearly with ϵ_s.

The coupling strength for different modes is determined by charge localization at the substrate. Modes with their surface charges located close to the substrate will redshift more than those whose surface charges are located far from the substrate. Thus, the redshift will be greatest for a dipole oriented perpendicular to the surface. For light incident at an angle onto particles on high permittivity substrates, the small peak shift for s- and large peak shift for p- polarized spectra can manifest as a polarization-dependent color change.[56]

Image interactions can be particularly dramatic for particles on metallic films, separated from conductive contact by nanometer-scale spacers. For polarizations parallel to the film, the induced image cancels the dipole, and no scatter is observed in the far field; for polarizations perpendicular to the film, the induced image couples resonantly to the dipole and far-field scattering is observed with a peak dramatically redshifted (from about 540nm to 670nm for a gold particle on a gold film) from the individual nanoparticle resonance on a dielectric substrate.[57] The redshift is consistent with interactions in nanoparticle dimers illuminated with light polarized along their symmetry axis. Incorporating the nanoparticles into a Kretschmann-configured surface plasmon resonance measurement results in a high sensitivity to very small thickness changes in the spacer layer, which in aqueous environments could enable Angstrom-scale distance measurements.

Mode hybridization picture

The effective medium and image charge approaches, while convenient, obscure a deeper way to understand particle-on-substrate system: the symmetry of the dielectric environment is broken by the substrate. The broken symmetry lifts the degeneracies between plasmon modes, allowing them to mix. The multipolar coupling due to

symmetry breaking can be understood qualitatively using a plasmon hybridization picture.[58]

In an isotropic environment, a nanosphere has a 3-fold degenerate dipole resonance. When placed on a substrate, these split into two resonances: the first is a dipole oscillating perpendicular to the surface (D_1, Fig. 2.10a), while the second is a dipole oscillating parallel to the surface (D_2, Fig. 2.10b), which is two-fold degenerate. The nanosphere also has a 5-fold degenerate quadrupolar mode, which splits into three orthogonal modes with different surface charge distributions: Q_1 is oriented perpendicular to the substrate (Fig. 2.10c), Q_2 results in a charge distribution with a greater interaction strength than Q_1 (Fig. 2.10d), and Q_3 has the weakest interaction strength of all (Fig. 2.10e).

At the interface, the surface charges induced on the substrate are similar for the vertically-oscillating dipole D_1 and the quadrupolar mode excited by 45 degree incident light (Q_2, though with the opposite charge distribution than that illustrated in Fig. 2.10d). The substrate thus mediates an interaction between these modes.[59] The quadrupole-like result of this hybridization has a dipolar component that allows far-field radiation, whereas the original quadrupolar mode is not necessarily bright. The hybridization of modes results in a peak splitting, which depending on the details of the system may or may not manifest as individually resolvable peaks; instead, the hybridization may simply serve to broaden the existing vertical dipole peak. This is especially true for lower permittivity substrates, in which the plasmon mode broadens into an anomalous "spoof" plasmon.[56] This hybridization picture is essentially the same for dielectric and metallic substrates.

(a) First dipole mode

(b) Second dipole mode

(c) First quadrupole mode

(d) Second quadrupole mode

(e) Third quadrupole mode
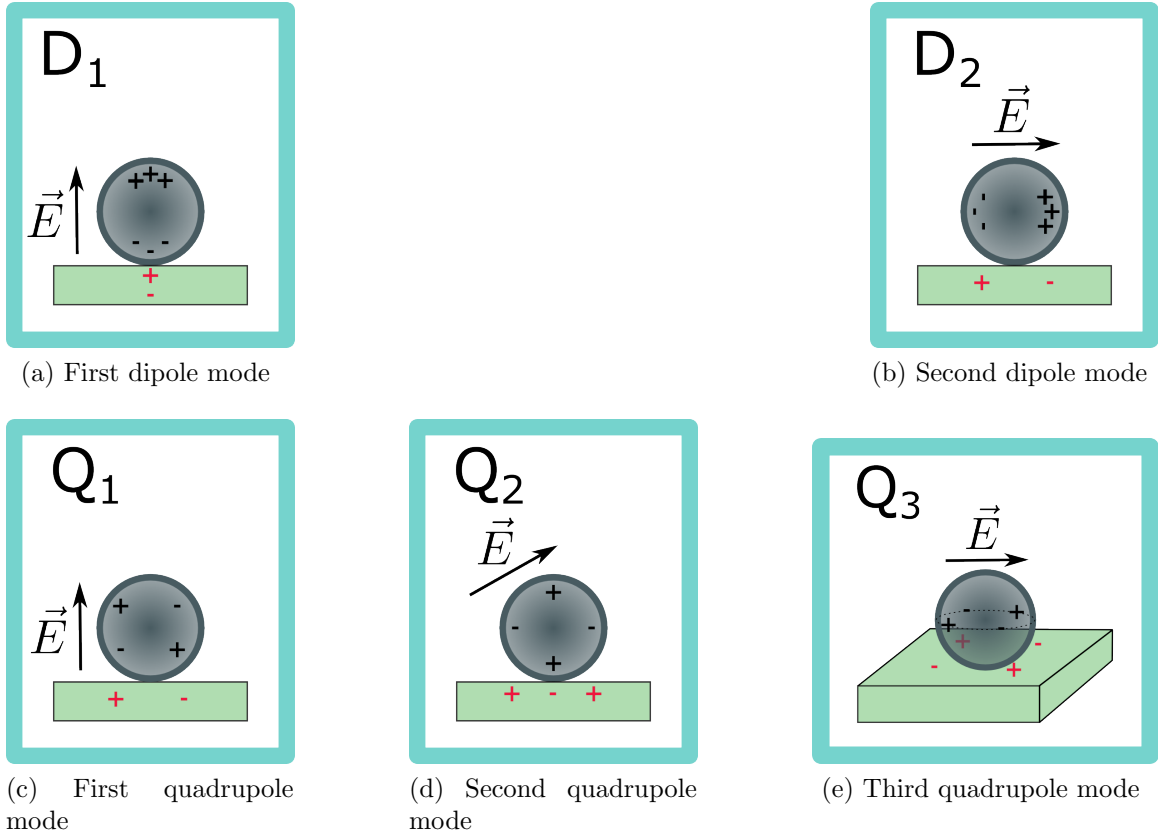
FIGURE 2.10. Nanoparticle-film mode hybridization picture.

Broken symmetries in other plasmonic systems have been shown to mix the multipolar modes within a single particle, modifying the resonant frequency of the system and changing how those modes couple to the far field.[60] For example, the quadrupolar plasmon modes of small particles are optically dark (that is, they cannot be excited from or radiate to a free space plane wave), but they can become bright in the presence of a substrate as they hybridize with the radiative dipolar mode.

Hybridization regimes: dependence on the thickness of the metal film

For metallic substrates, the particle plasmons can additionally hybridize with surface plasmon polariton modes of the metal, behaving similarly to the Fano-

Anderson impurity model in condensed matter physics in which a discrete mode (in this case the particle plasmon) interacts with a continuum (the metal band structure or surface plasmon polariton band).[61, 62] In this case, the nanoparticle plasmon resonances can redshift or blueshift depending on the relative energies of the nanoparticle plasmon and surface plasmon polaritons. Thus, when illuminating with different light polarizations, there is nearly no substrate effect for the s-polarization.[56]

There are three interaction regimes in the particle-plasmon and surface-plasmon hybridization ("tunable impurity") picture. First, when the film is much thicker than the nanoparticle diameter, the effective film continuum lies above the particle plasmon resonance. Here, the hybridization results in strong energy splittings. The image approximation is a valid description of this scenario. The second regime occurs for film thicknesses on the same order as the particle diameter. In this case, the particle plasmon lies within the surface plasmon continuum. The plasmon density of states at $\omega = \omega_p$ is reduced, thus the hybridization is weaker, and the weak hybridization results in a broadening of the discrete nanoparticle plasmons. Finally, for films much thinner than the particle diameter, the nanosphere plasmons are at a higher energy than the film continuum. A resonant virtual state emerges, which is primarily a film plasmon state which can be understood as an incomplete image response to the nanoparticle plasmon. The energy of this state depends strongly on the thickness of the metal film, with the energy decreasing as the film thickness is reduced. The thick, intermediate,[63] and thin[61] regimes have each been studied experimentally.

The mode hybridization picture, image charge approximation, and effective medium approach are each helpful frameworks for different material combinations

and size regimes. We will couch our discussion of substrate effects in the appropriate framework each time we encounter them in the following chapters.

2.6. Summary

Armed with a physical intuition for light-matter interactions in nanoparticles, we return to the question we began with: how can we tune the optical response of silver nanostructures to specific colors in the visible range? In Chapter III, I investigate a chemically deposited silver system in order to understand how very different optical properties can emerge from films with macroscopically similar but microscopically different morphologies. In Chapter IV, I simulate the response of monodisperse silver nanospheres near flat metal films, in order to predict how system morphology can be manipulated to tune optical resonances. Finally, in Chapter V, I build and measure these systems, demonstrating that silver particles near silver metal films can achieve a predicted resonance in the green.

CHAPTER III

MORPHOLOGICAL DRIVERS OF VARIABLE EXTINCTION IN SILVER
AGGREGATE FILMS

*The experimental work in this chapter was done by Shikhadeep DeFazio and
Yevgeniy Krasnitsky. I performed all data analysis, modeling, and writing.*

Chemically deposited metal nanoparticle films have been employed in
applications ranging from sensing[11, 64, 65] and catalysis[66, 67] to efficiency
enhancements for photodetectors[68, 69] and solar cells[70]. Chemical deposition
processes can produce a range of film morphologies with varying levels of particle
aggregation, from isolated single particles to compact and extended aggregated
islands to percolated structures. Different applications take advantage of the unique,
morphology-dependent electromagnetic excitations these films can support, such as
individual particle plasmon resonances[69] or spatially localized modes stemming from
multiple scattering in dense configurations of randomly located particles.[11] Because
experimenters excite and detect these electromagnetic modes optically, the advantages
they offer can only be harnessed if their optical properties are thoroughly understood.

Robust models have been successfully developed for the extinction and
scattering of nanoparticle films with various levels of aggregation. Monodisperse
particle ensembles with no aggregation are adequately described by Mie theory.[27]
Polydisperse ensembles can be handled using a size-distributed Mie model, treating
aggregates containing only a few small particles (radii between 2nm and 10nm)
as uniform spheroids under the Mie-Gans model.[51] Highly symmetric aggregates
consisting of a few small (less than 5nm radius) identical particles can be treated
in the quasistatic approximation as coupled dipoles, while aggregates of up to ten
40nm radius single-particle constituents have been modeled using the generalized

39

Mie theory.[43] However, films comprising large, polydisperse particle ensembles and irregular aggregates of nonidentical constituents cannot be modeled using any of these approaches alone.

In this chapter, I consider the extinction of silver island films grown via electroless deposition methods. Samples with identical deposition conditions nevertheless exhibit very different extinction line shapes. In order to understand how those variations in line shape arise from differences in microscopic morphologies, I analyze particle size distributions, aggregate configuration, and island coalescence for a range of films. These quantities serve as inputs for a size-distributed Mie model constrained by aggregation information. The model can both explain the features of optical extinction spectra and yield physical insight into their dependence on film morphology, and thus aid in employing films in practical applications. I find that extinction line shape is described well by the size-distributed Mie response of round particles, with broadening stemming from an increase in both average particle size and polydispersity.

3.1. Deposition and characterization of Tollens films

Deposition of silver nanoparticle films

Silver nanoparticle films with a range of surface coverages were grown using a modified Tollens reaction.[71] Glass microscope slides were cleaned by soaking in piranha solution (a 1:3 ratio of hydrogen peroxide to sulfuric acid) for at least 30 minutes to remove organic contaminants. Substrates were then coated with a solution containing 40% (vol/vol) poly(methyl methacrylate) (PMMA), 40% anisole, and 20% ethanol, by spin coating at 3000rpm for 60 seconds and curing at 180°C for 6 minutes. For the purposes of a different experiment, the PMMA was doped with Rhodamine

6G dye at a concentration of $6.022 * 10^{11}$ molecules/square cm. The dye produces an extinction peak at about 530nm which is both spectrally distinct from and far weaker than the aggregate response, and thus only visible for the two lowest filling fraction samples.

PMMA-coated substrates were soaked for at least 1.5 hr in a glucose reducing agent (0.6%wt glucose in ultrapure 18.2MΩ-cm water), which is maintained at 6°C using a temperature-controlled water bath. A Tollens reagent (5mL of 10%wt aqueous silver nitrate, 0.5g of 0.5%wt sodium hydroxide, and 1.5g of 10%wt ammonium hydroxide) was added to the chilled glucose solution under mechanical stirring. Maintaining low temperatures during the reaction allows for smaller particles to form, while mechanical stirring slows the particle growth rate compared to sonication.[72]

As the reaction begins, the solution color changes from clear to yellow. The initial color change occurs only after the reagents are well-mixed, allowing for homogeneous nucleation of silver nanoparticles which results in narrow particle size distributions.[72] During the 10–30 seconds following the initial color change, the color evolves from light to bright yellow as particles grow rapidly.[73] Finally, the color evolves to brown and then gray over time scales of minutes as particles slowly aggregate[72, 74] and deposit on substrates. At the desired deposition time, measured from the initial color change, samples were removed from the solution and rinsed with ultrapure water and ethanol to stop the reaction. Silver particles were removed from one side of each substrate by swabbing with a 20% hydrochloric acid solution, then the samples were rinsed again with ethanol and allowed to dry. After drying, samples were stored in an inert nitrogen environment to avoid oxidation. We made 2–10 samples for each deposition time between 5 and 60 minutes in 5 minute increments.

Structural characterization via SEM

To measure the number and size of nanoparticle aggregates on PMMA, we imaged samples using an FEI Quanta 200 FEG variable pressure SEM. Ten scans were taken over different areas for each sample. Typical image sizes were about 1024x880 square pixels with 6nm/pixel scale factors for lower deposition times and about 512x440 square pixels with 14nm/pixel scale factors for higher deposition times.

Image analysis was performed in MATLAB using both built-in image processing algorithms and user-contributed programs. First, built-in image processing scripts were used to correct uneven background illumination and maximize contrast. To remove noise from substrate charging without eroding the smallest nanoparticles, images were thresholded by brightness using an interactive user-contributed script.[75] The resulting boolean images, representing a two-dimensional projection of the three-dimensional film, were used to calculate the surface coverage, ζ, defined as the ratio of white pixels to total pixels in the image. Surface coverage calculated in this way has an approximate maximum error not exceeding 0.01.[73]

Extinction measurements

Ultraviolet-visible extinction (UV-VIS) spectra were collected in air on an Agilent 8453 spectrophotometer over a 350–750nm range, using a glass slide as a blank sample. In order to correct for a small (1%) intensity drift which may be due to the instrument source or electronics, three spectra were averaged for each sample. Repositioning error during this process is not a concern, because the spot size of the sampling beam averages over a large sample area. Peak and shoulder positions were extracted from smoothed spectra and their second derivatives using PeakUtils, a peak detection

algorithm in Python.[76] In the following section, we examine the variability of these extinction spectra, and explore how that may be driven by film morphology.

3.2. Variation in extinction line shapes

The line shapes of extinction spectra typically depend on silver surface coverage; however, some samples of the same surface coverage demonstrate very different line shapes, as shown in Fig. 3.1. Low surface coverage samples typically have clearly distinguishable, high intensity dipole peaks and lower intensity quadrupole peaks, while higher surface coverage samples tend to have a distinct, intense quadrupole peak and a broad, weak dipole shoulder. We dubbed these line shapes and the samples which produce them α and β, and classify samples by their relative peak intensity, $\Delta_I = I_{dipole} - I_{quadrupole}$. We define α samples as having positive Δ_I (dipole dominance) and β samples as having negative Δ_I (quadrupole dominance). Line shapes do not transition smoothly from α to β types as surface coverage increases; instead, beginning at a surface coverage of about 0.2, sample line shape cannot be used to reliably infer surface coverage or vice versa. The transition between α and β line shapes occurs between surface coverages of 0.2 and 0.4, corresponding to deposition times between 20 and 30min. Deposition times below and above the transition time range result in exclusively α and β samples, respectively.

While α and β spectral categories can be easily identified by eye using Δ_I; we sought to better quantify these categories using the peak width and position, which are more directly driven by morphological details. The positions, intensities, and widths of the dipole and quadrupole peaks were extracted by fitting spectra with a single or double Lorentzian model using LMFIT, an open-source least-square minimization and curve fitting program in Python.[77] When peak width is plotted against position,

43

as shown in Fig. 3.2, natural groupings of α and β emerge in the long-wavelength dipole resonance. The α dipole peak redshifts and broadens over a wider range than for β samples, whose dipole widths and positions are less dependent on surface coverage. This suggests that α samples offer superior optical tunability using the dipole resonance. The quadrupole resonance, by contrast, shifts and broadens rather uniformly with surface coverage, but in a narrow spectral range.
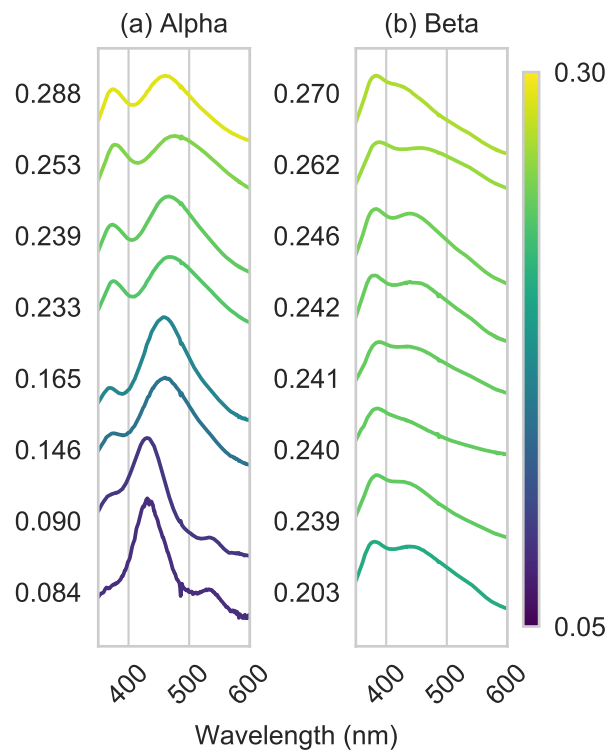
FIGURE 3.1. Extinction line shape variation in Tollens films
(a) Dipole-dominant α and (b) quadrupole-dominant β type normalized extinction line shapes, offset vertically for clarity and colored by sample surface coverage. Each curve is labeled with its surface coverage. The small peak at $\sim$530nm is due to the Rhodamine 6G dye and is not included in our peak finding algorithm.

44
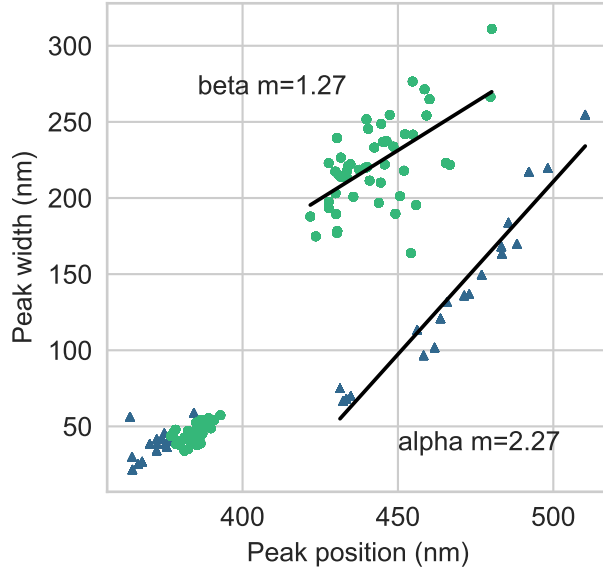
FIGURE 3.2. Defining Tollens sample groups by peak position and width.
The α and β samples naturally group when peak width is plotted against position.
Note the redshift and broadening of the dipole peaks, which is more pronounced in
α samples.

We hypothesize that the line shape variations arise from differences in the microscopic morphologies of the α and β samples. In order to test this hypothesis, we analyze the microscopic morphologies of Tollens films and build an extinction model based on the results.

3.3. Microscopic morphologies of Tollens films

The morphologies of films resulting from the Tollens process can range from dilute islands to collections of aggregates to fully percolated and even semicontinuous films.[73] These very different morphologies require some common index for comparison; one such parameter is the surface coverage. Critical values of the surface coverage are used to describe morphological transitions of physical consequence; for example, surface enhanced Raman scattering reaches a maximum efficiency when

45

the density of hot spots peaks, this occurs at surface coverages corresponding to the percolation threshold.[11]

Aside from this simple surface coverage measurement, Tollens films are characterized by several other characteristic length scales. These include the 25nm monomer radius, which is independent of film growth time, and the average island radius which increases from about 30–200nm as growth proceeds.[73] While these characteristic lengths are reproducible from batch to batch, both particle nucleation and deposition onto the substrate are random. This leads to samples which have statistically similar global morphologies (averaged across hundreds of square microns) but variation in morphologies at the microscale. Especially for relatively low surface coverage films, these microscale variations may have a large impact on film optical response. In the next section, we quantify these microscopic morphologies by analyzing island shape.

<u>Island shape analysis procedure</u>

Islands were defined based on their connectivity in boolean SEM images using the following procedure. First, particles touching the edges of the image were removed to discount partial islands. Then, a 2-sigma Gaussian blur was applied to smooth pixelation effects at island borders which lead to spurious perimeter measurements. Finally, islands were identified as white pixels sharing an edge (4-connected definition), and a built-in image analysis routine tabulated properties such as area, perimeter, and centroid. Examples of raw SEM images and their thresholded, Gaussian-smoothed counterparts are shown in the top and middle rows of Fig. 3.3.

46
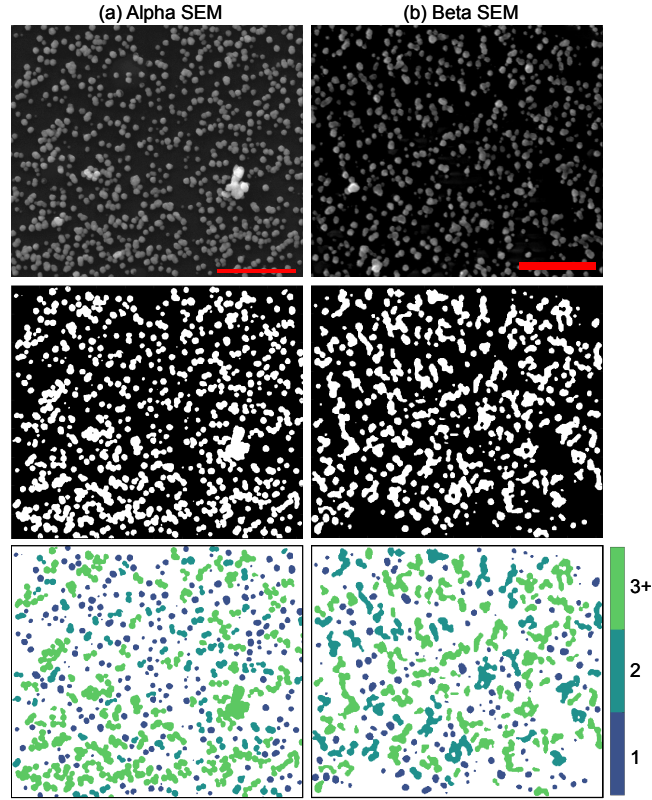
FIGURE 3.3. SEM of alpha and beta samples with similar surface coverage. SEM of samples with similar surface coverage in the crossover region: (a) α, $\zeta = .301$ and (b) β, $\zeta = .306$. Top row: raw SEM; middle row: filtered SEM with Gaussian blur; bottom row: islands colored by the estimated number of particles in each aggregate. Scale bars are 2 micron wide.

We assume that individual islands contain a number N_p of round particle constituents, which may be coagulated (not touching) or coalesced (fused together by additional growth at their boundaries). Single round particles ($N_p = 1$) are assigned by their circularity, defined using $f_{circ} = 4\pi A/p^2$ where p is the island perimeter. Islands with $f_{circ} \geq 1$ are classified as single round particles. Theoretically, round objects should have a maximum circularity of 1, but due to MATLAB's perimeter algorithm, the round particles in our dataset sometimes had circularities just greater than 1.

Islands which are not round must be further classified by the number of round constituents N_p. This requires an additional particle-counting and assignment step. To assign aggregates of $N_p > 1$, we identify their round particle constituents via island edge curvature using MATLAB's built-in circular Hough transform method (imfindcircles). The minimum radius is set to 5 pixels (the imfindcircles lower limit), which for for α samples corresponds to about 30nm. This digitally-defined single-particle unit is on the same order as the previously-observed 25nm fundamental monomer grain size (mean particle size at early deposition times).[73] Constituent particles are assigned to their host aggregates by matching the center position of a given constituent circle to the island containing that pixel position.

Discussion of morphological results

In the bottom row of Fig. 3.3, SEM images have been colored by N_p, revealing that the β sample at this surface coverage ($\zeta \sim 0.25$) has larger round particle constituents, fewer total islands, fewer round islands, and more aggregates than the α sample. Overall, β samples appear more highly aggregated than α samples, suggesting that a morphological transition driven by particle aggregation may underpin the observed line shape variation.

In order to compare the size of round islands and multiple-particle aggregates, we employ the radius of gyration, defined as $R_g = (\frac{1}{A} \sum_{i=1}^{A} a_i)^{1/2}$ where a_i is the distance of each pixel from the island center of mass.[78] The average R_g ranges from about 25–175nm for nanoparticle films ranging in surface coverage from 0.06 to 0.52. A crossover between α and β categories occurs between surface coverages of 0.2 and 0.4, when average R_g jumps up and the slope of both $R_g(\zeta)$ and island area $A(\zeta)$ increases

(Fig. 3.4). During this crossover, β samples have small area yet large R_g compared to α samples because β islands are less compact.
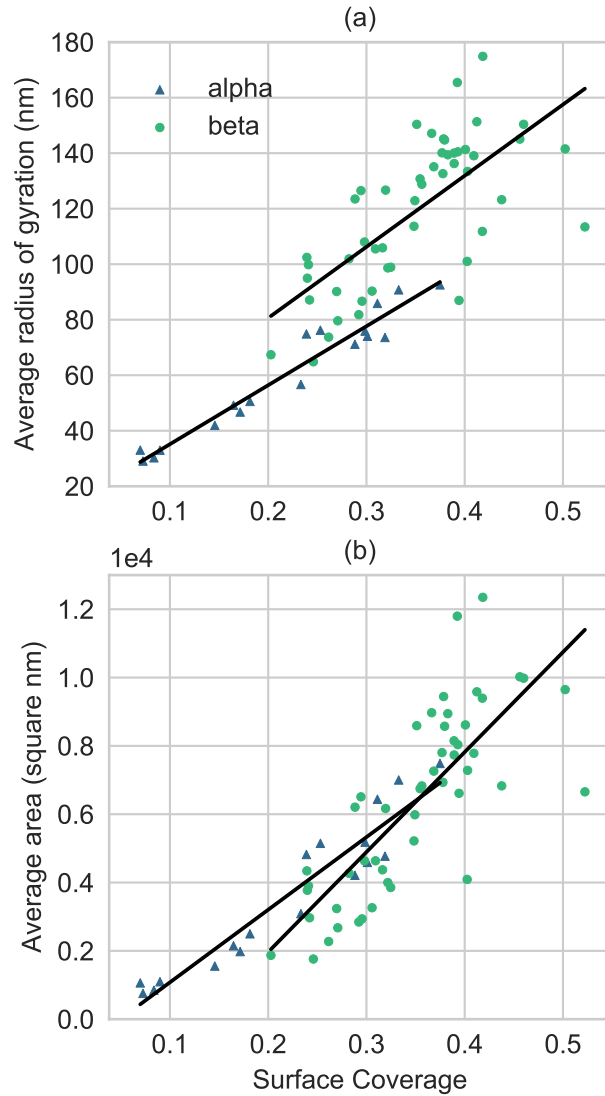
FIGURE 3.4. Average island morphologies versus surface coverage. Average (a) gyration radius and (b) area for all islands.

To understand how islands aggregate as ζ increases, we track $f_p = N_p/N_{tot}$, the ratio of islands with a given number of constituent particles N_p to the number of total islands. This is plotted in Fig. 3.5. Round islands ($N_p = 1$) dominate in

all samples, making up more than half of α islands. The round island population decreases monotonically until $\zeta = 0.3$, when it levels off. Dimers ($N_p = 2$) increase quickly from about 5% to 20% of all α islands as ζ increases from 0.05 to 0.25. Meanwhile, large aggregates ($N_p \geq 3$) increase slowly, overtaking dimers by about $\zeta \sim 0.26$. In β samples, dimers are always outnumbered by large aggregates (including the large, irregular aggregates which cannot be assigned a specific N_p). Based on these population statistics, we hypothesize that the round island majority should dominate the α extinction response for low ζ, with greater contributions from dimers and larger aggregates emerging as ζ increases.
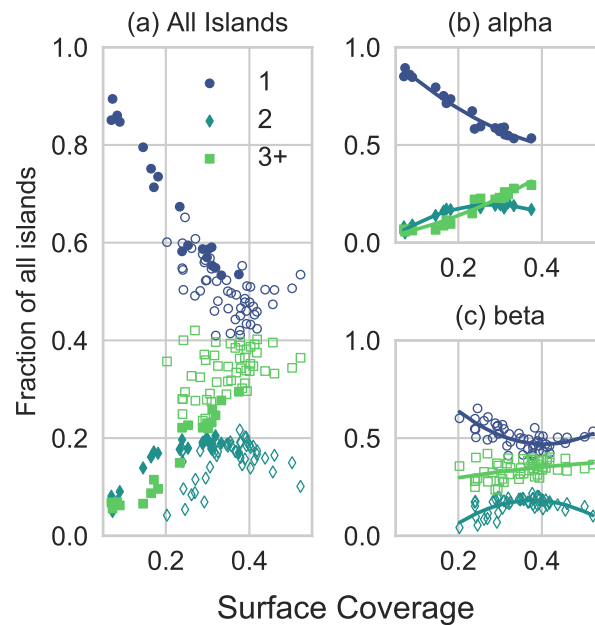
FIGURE 3.5. Individual island shape trends with surface coverage. The fraction of all islands populated by a given aggregate number for (a) all samples, (b) α samples only (filled shapes), and (c) β samples only (unfilled shapes). Round islands are identified as N=1.

Estimation of aggregate quality of fit

The constituent assignment process allowed us to easily detect three types of spurious fits: 1) circles with centers outside an eligible host island, 2) aggregates fit by only a single circle, and 3) aggregates with no identifiable circular constituents. These spurious fits generally seem to stem from aggregates with large N_p, whose constituents suffer a loss of definition due to the thresholding process required to procure a binary image. Therefore we include them in the $N_p \geq 3$ count. The total fraction of aggregates affected by spurious fits was only about 5% for α samples but sometimes up to 35% of β samples.

We further estimate aggregate quality of fit by calculating the fraction f_A of aggregate area covered by constituent particles, expressed by $f_A = (\sum_p A_p)/A$, where A_p is constituent particle area and A is aggregate area. The aggregate is fit well by its constituents if $f_A \sim 1$. We find that f_A drops as N_p increases, because the imfindcircles method only detects constituents contributing to an aggregate's edge curvature. The fractions of aggregates which come within 10% or 20% of complete coverage are shown in Table 1. Excluding poorly covered aggregates does not appreciably affect how N_p trends with surface coverage, even though nearly 70% of large aggregates are not within 10% of perfect coverage. This robust island statistics is thanks to the large number of islands measured per sample (1000-6000) and small number of large N_p aggregates. We therefore do not restrict our analysis to any particular f_A range.

In this section we explored film morphology and discover that α samples comprise mostly round islands. To test our hypothesis that round islands dominate the α extinction response, we simulate the extinction of those samples based on the numbers and sizes of only the round islands in each.

TABLE 1. Fraction of aggregates with number of constituents N_p deviating from complete area coverage by 10% or 20%.

N_p	10%	20%
2	45	70
3	39	63
4+	30	53

3.4. Size-distributed Mie extinction simulation procedure

Mie extinction was simulated with the open-source Python program MiePy,[37] based on the Mie code by Bohren and Huffman,[24] using tabulated values for silver permittivity from Johnson and Christy.[25] We included up to 10 multipole orders.

<u>Effect of a substrate on particle extinction</u>

To account for the presence of a substrate, which is known to redshift particle resonances, we embedded particles within an effective index environment of n=1.25, chosen by averaging the indices of the air environment and the PMMA-glass substrate.[27] The following explains our choice of effective index.

Spectra for Tollens films with a coverslip redshift and broaden

We measured 15min deposition time Tollens samples on PMMA with and without a coverslip and index matching fluid of n=1.516. In order to calculate the peaks and peak shifts, we fit the resulting spectra to a model of two Lorentzians on a falling exponential background, as shown in Fig. 3.6. The dipole resonance shifts by about 55nm while the quadrupole shifts by about 60nm.
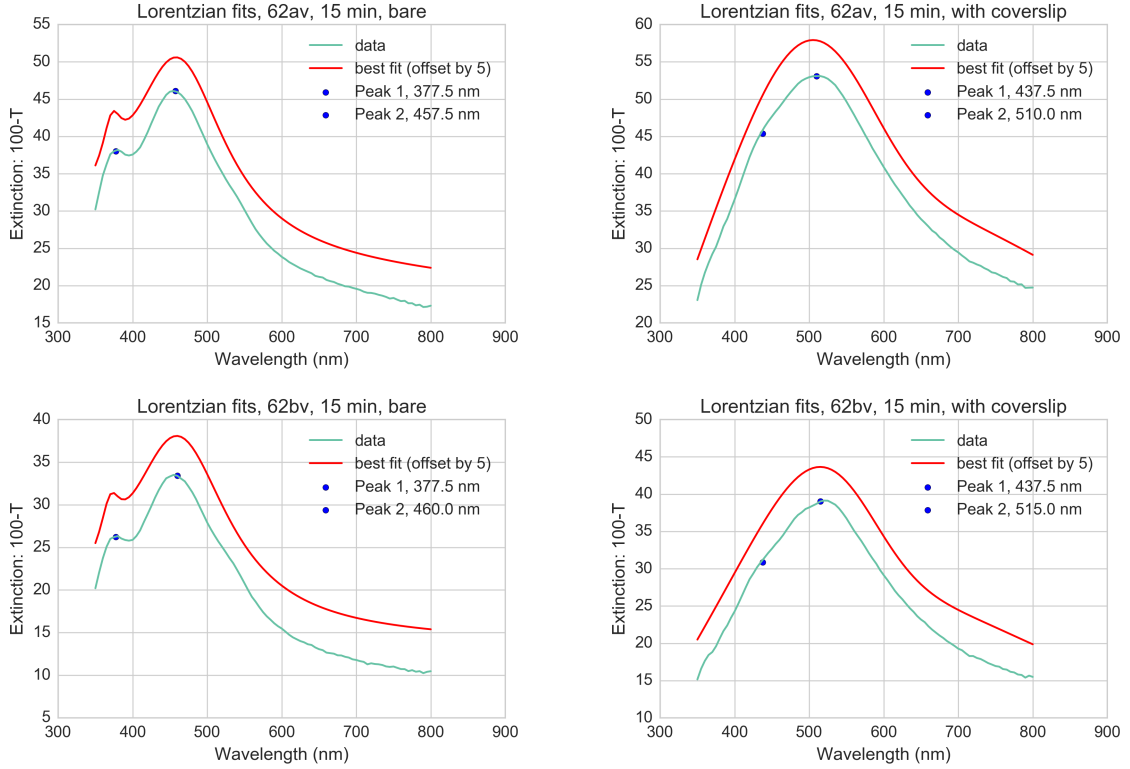
FIGURE 3.6. Lorentzian fits to Tollens samples with and without a coverslip. Samples without a coverslip (left) have two distinct peaks which redshift and broaden when a coverslip is added (right).

Calculating an empirical effective index term by matching simulation to data

An empirical effective index term is given by $n_{eff} = \xi \cdot n_{medium} + (1 - \xi)n_{substrate}$ where ξ is an empirical weighting term.[54] In order to estimate ξ, we simulated the 15 minute Tollens samples as monodisperse samples. For simplicity, we chose to use a single effective radius corresponding to the peak of the lognormal particle size distribution for the other 15 minute deposition time samples in our dataset. The results of choosing ξ equal to 1, 0.5, and 0 are shown in Fig. 3.7. Simulations with an n=1 effective index environment (left) do not agree with the data, but simulations with an n=1.25 effective environment (center) do agree. On the right is a simulation

53

using an n=1.5 environment and the data for samples with cover slips, which show

that the radii chosen are a reasonable proxy for these samples.
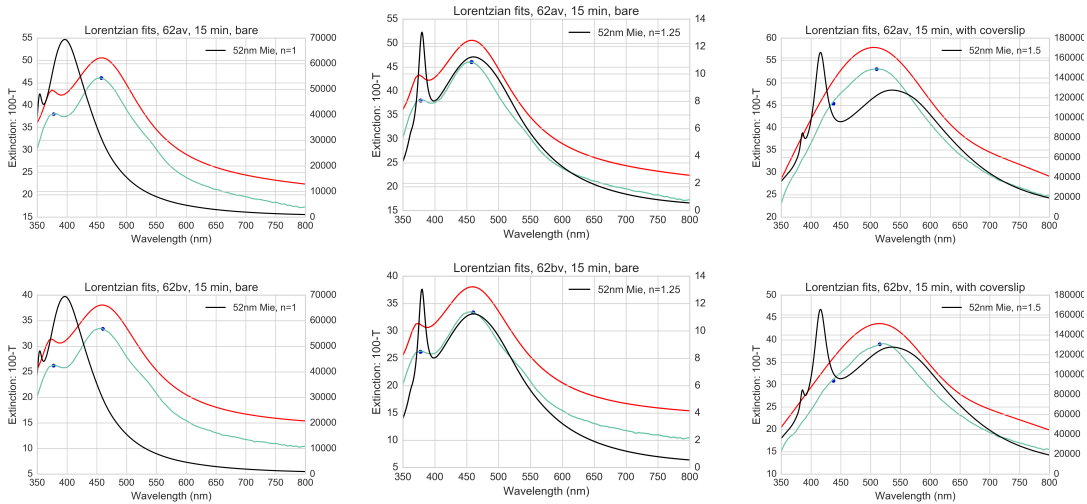
FIGURE 3.7. Choosing an empirical refractive index offset term.
Extinction of two 15min Tollens samples without a coverslip (top and bottom rows)
are compared to simulations of a single 52nm particle radius and a uniform
refractive index environment of n=1 (left) and n=1.25 (center). Simulated spectra
with n=1.5 are compared to data for the same samples with a coverslip (right).

While the effects of substrates on particle resonance can be complex,[79, 80]

monodisperse simulations support the use of a simple effective index, which allows us

to proceed with a descriptive Mie model rather than relying on alternative simulation

techniques which may produce more accurate results but obscure the underlying

physics.

Generating particle size distributions

To isolate the effects of round particles on sample response, we simulate

extinction by calculating the size-distributed Mie response of samples with aggregates

excluded. The response of an ensemble of particles is modeled as a linear combination

of the single-particle response; that is, $\sigma_{tot} = \sum_{i}^{n} \sigma_i(R_i)$, where σ can be the extinction,

absorption, or scattering cross section. This model assumes negligible particle-particle interactions through near-field coupling or far-field multiple scattering. This assumption is known to be valid when particle sizes are on the order of the wavelength or larger and are separated by distances more than about four times their radii.[41] In our films, neither condition is met; however, we retain this assumption for the purposes of testing an aggregate-excluded Mie model against the real extinction of these films.

We extracted particle size distributions for Mie simulations from MATLAB image analysis results. While particle sizes were log-normally distributed with aggregates included, they were skew-normally distributed with aggregates excluded. The log-normal distribution is commonly used to describe particles grown under homogeneous nucleation conditions. The distribution can be derived using kinetic arguments for particle formation, assuming that particle growth and destruction times are normally distributed and that particle sizes are not restricted to a specific minimum or maximum. This growth model does not account for particle aggregation and coalescence, yet the log-normal distribution is a good fit for our samples with aggregates included. However, because the distribution is derived from a particle formation model, tampering with particle sizes after formation, for example by sieving, can result in deviations from linearity on a log-log plot of particle size and abundance.[81] Excluding aggregates from our simulation sample is a digital form of such sieving, and while it does not significantly affect the distribution mode, it does narrow the overall width by removing the long tail at large R_g.

To allow any arbitrary surface coverage to be simulated, distribution parameters (shape, location, and scale) were plotted against sample surface coverage, and curves of best fit (linear or quadratic where appropriate) were calculated for each parameter.

For α samples, the mean and variance of skew-normal versus log-normal distributions were indistinguishable, but the skew-normal fits outperformed the log-normal fits for all other parameters. For β samples, neither distribution yielded reliable trends with surface coverage; thus, we simulate only the surface coverage range and concomitant size distribution parameters for α samples.

To model α samples, the distribution parameter fits for a given surface coverage were used to generate a particle ensemble. Since the skew-normal distribution allows negative particles, these were forced to be positive. At most 1% of particles required correction, so we do not expect this process to introduce bias toward smaller particles. The extinction cross section was calculated for each particle in the ensemble and summed to simulate the overall sample. Ten ensembles were generated for each sample surface coverage.

3.5. Comparing measured and simulated extinction spectra

Mean simulated Mie spectra are compared to UV-VIS spectra of comparable surface coverages (including both α and β samples) in Fig. 3.8. Line shapes at small ζ have a strong dipole peak and weak quadrupole shoulder. As ζ increases, the dipole peak redshifts and broadens and the quadrupole peak begins to emerge, increasing in intensity until it overtakes the dipole intensity at about $\zeta \sim 0.2$. Finally, the dipole broadens until it is barely distinguishable by $\zeta = 0.4$. The bulk of the qualitative line shape behavior, including the transition from α to β line shapes as quantified by Δ_I, is reproduced by the round particle majority alone.
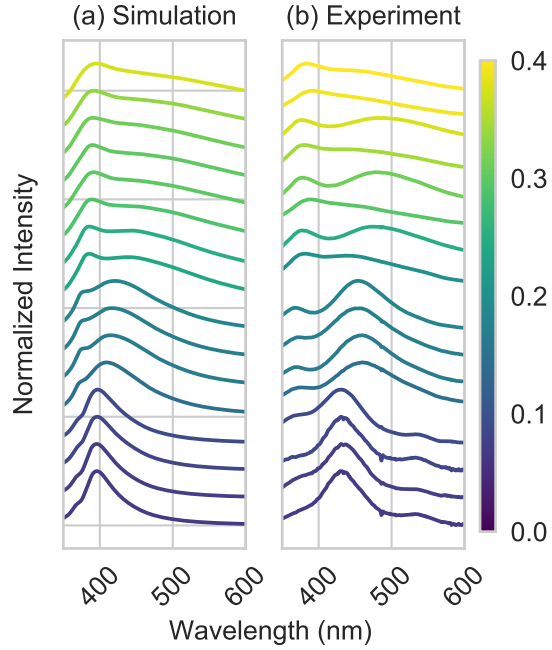
FIGURE 3.8. Simulated versus measured Tollens extinction spectra.
Extinction of silver nanoparticles (a) simulated using Mie theory and (b) measured
via UV-VIS spectroscopy. Traces are colored and ordered by surface coverage from
bottom to top, normalized to their maxima and offset for comparison. The small
peak at ~530nm is due to the Rhodamine 6G dye and is not included in our peak
finding algorithm.

The reproduction of the α–β transition in simulations is especially clear when
considering the dipole width-position relationship (Fig. 3.9). The width-position
slope for measured α samples matches simulated samples for $\zeta < 0.2$ (dashed lines).
However, simulated peak widths jump up abruptly for $\zeta > 0.2$, where the slope
of simulated samples (dotted line) is much flatter than other measured α samples
(dashed) and similar instead to the slope of measured β samples (solid line).
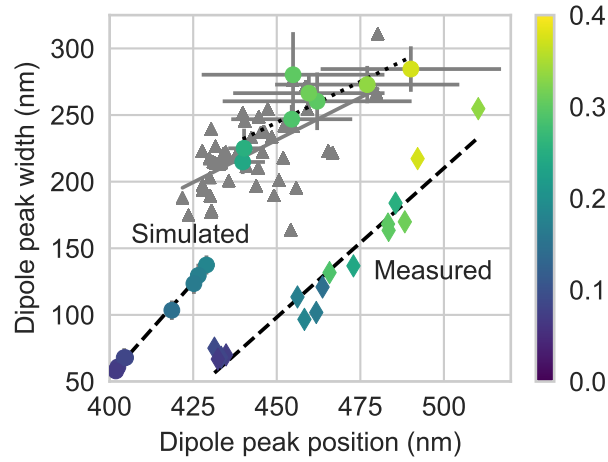
FIGURE 3.9. Tollens extinction peak positions and widths
(a) Measured (squares) and simulated (circles) α extinction dipole peak position
and width, colored by surface coverage increasing dark to light. Error bars indicate
the standard deviation of ten Mie simulation trials for each sample. Small gray
triangles indicate measured values for β samples.

Three sample archetypes emerge

The α samples appear to cluster into 3 distinct groups (a, b, and c) based
on their simulated dipole peak and width characteristics. These groups can also be
observed in the mean and variance of the round particle size distribution; distributions
are shown in Fig. 3.10 and extracted mean and variance are shown in Fig. 3.11.
Group statistics are summarized in Table 2. The similarity amongst samples within
a group indicates that the chemical deposition process is highly reproducible before
the transition surface coverage range.
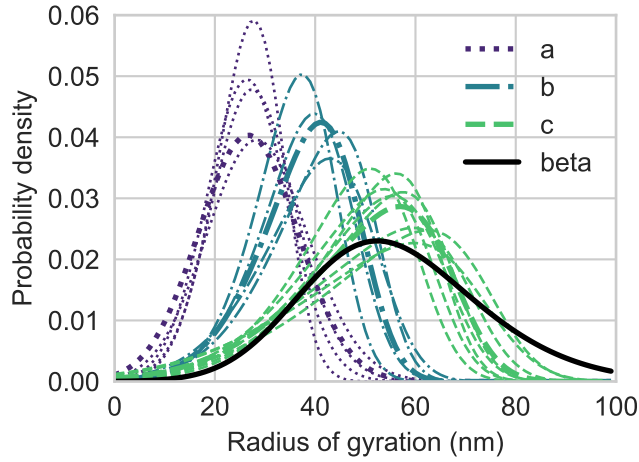
FIGURE 3.10. Round particle size distribution for alpha and beta samples. Round particle size distributions for α samples grouped by their optical extinction line shape (colors) and β samples (black) in the same surface coverage range as group c. Darker curves correspond to the mean size distributions for those groups and lighter curves to the individual samples.
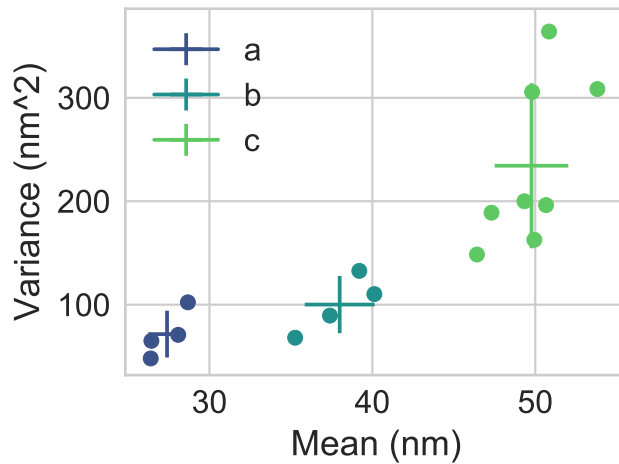
FIGURE 3.11. Mean and variance of Tollens round particle size distributions. Peaks and widths of round particle size distributions for α samples.

As ζ increases, particle size becomes larger and more disperse, causing the dipole peak to redshift and widen due to inhomogeneous broadening. The α group c size distribution closely resembles the mean β size distribution for the same surface coverage range. This causes the simulated α group c extinction to resemble measured

β extinction. This suggests that the bulk of the line shape variation may be explained solely by the round particle size distributions.

TABLE 2. Morphological and optical characteristics of alpha samples, grouped by surface coverage.

Group	a	b	c
Surface Coverage range	0.07 - 0.09	.15-.18	.24-.37
Deposition Time (min)	5	10	15-30
Simulated dipole position (nm)	403 ± 2	425 ± 2	460 ± 20
Simulated dipole width (nm)	32 ± 3	62 ± 4	128 ± 8
Rg mean (nm)	27	38	49
Rg variance (nm^2)	71	100	234

<u>Redshifts due to aggregation and substrate effects</u>

There is a persistent redshift between measured and simulated films. This redshift may be due to particle-particle coupling, elongated aggregates, or more complex substrate interactions. To estimate the magnitude of the redshift that may be assigned to particle-particle coupling in different aggregate configurations, we analyzed the statistics of two-particle aggregates (dimers). The single-particle resonances of such dimers, especially in α samples, are predicted to couple together, resulting in a splitting of the coupled mode resulting in a dipole redshift.[39]

Within the dimer population, we calculated dimer spacing as $s = d - 2\overline{R_g}$, where d is the center-to-center distance between particles and $\overline{R_g}$ is the average radius of gyration. About 70% of dimers in α samples have $s \leq 0$, indicating that they are fused or partially stacked out of plane. The remaining 30% of dimers are separated. Their average size and spacing varies by their α grouping as indicated in table 3.

TABLE 3. Radius of and spacing between dimer constituents for fused and separated dimers.

Group	R1 (nm)	R2 (nm)	$s < 0$ (nm)	$s > 0$ (nm)
a	51 ± 8	46 ± 7	-14 ± 11	12 ± 10
b	61 ± 9	53 ± 9	-22 ± 13	11 ± 7
c	78 ± 13	68 ± 16	-28 ± 17	13 ± 12

Separated dimers have redshifts increasing as spacing decreases following a $1/s^3$ relationship.[82] Preliminary simulations using the Generalized Mie theory indicate redshifts of 75nm for particles with 40nm radii and 10nm spacing. However, a universal scaling law for separated silver dimers suggests a more conservative redshift of about 6-7nm. Simplifying fused dimers by considering them as spheroids with ratio of long to short half-axis of ~2, the dipole resonance along the long axis can shift from 425nm to about 600nm.[83] Dimer contributions may therefore easily account for and even exceed the observed redshift, which ranges from about 30nm to nearly 60nm. Substrate effects stemming from dipolar or multipolar coupling between a particle and its own image charge likely contribute within a 5-30nm range.[80, 84] The specific redshift magnitude attributable to dimers considering the statistical distribution of dimer sizes and spacings, and the magnitude due to interactions with particles and their substrate image, are topics of future investigation.

3.6. Aggregation as a primary driver of line shape variation

Here we discuss an alternative idea about the primary driver of line shape variation. Within a type (e.g. alpha type), the round island extinction explains much of the peak position and width trends. However, this does not adequately explain the beta line shape. When we compare the SEM and UVvis spectra of carefully selected samples with the same surface coverage yet different line shapes, the

SEM looks qualitatively more aggregated for beta samples. We suspect that a well-constructed index of aggregation for a given sample may correlate well with the alpha-beta designation. Some possibilities include: the average interparticle separation or average number of nearest neighbors for individual particles or for aggregate islands, or the distributions for those entities, or a combination thereof.

3.7. Summary

In this chapter, we probe the origin of variations in the extinction spectra of chemically deposited silver films of the same surface coverage. These greatest variability in line shape is observed in the same surface coverage range as a morphological transition, when large aggregates begin to outnumber dimers in the sample. Round particles remain the dominant component at all surface coverages, and extinction spectra simulated using a size-weighted Mie theory (and considering only the round particles) reproduce the observed line shape transition. We conclude that the extinction transition is driven primarily by the increasing mean and width of the single particle size, and that the difference in aggregation between α and β samples, while correlated with the transition, is not necessary to understand it. However, the measured dipole peak positions are redshifted from simulations; this redshift may arise from aggregate response, intra- island coupling, and/or substrate image interactions.

The modified Tollens reaction described here yields reproducible morphologies and optical response at low surface coverage, offering a simple route toward tunable optical response. The randomness inherent to the Tollens process is tolerable and even helpful in certain applications, such as surface enhanced Raman scattering, which relies on near field enhancement more than spectral specificity, and random lasing,

which relies on the random location of scatterers, a process that is not particularly sensitive to particle size. In the following chapters, I set the Tollens system aside and discuss spectral specificity, which is best adjusted using monodisperse particle systems.

CHAPTER IV

TUNABLE PLASMONIC RESPONSE IN NANOPARTICLE-FILM COUPLED
SYSTEMS

In nanoparticle-film coupled systems, consisting of metallic nanoparticles spaced nanometers away from thin metal films, light can be confined to sub-wavelength volumes with a high degree of control. This confinement effect can be tuned across the visible spectrum. The optical resonances of the system emerge as the charge distributions on individual nanoparticles interact with their own image charges in the flat film, producing hybridized modes. The resonant wavelengths of these hybridized modes are governed by the shape and size of the nanoparticle, the choice of metals, and the thickness of the spacer layer between the particle and flat metal substrate. As the spacer thickness decreases, the simplest hybridized resonance redshifts with a power law dependence ($d^{-0.058}$ to $d^{-1.2}$).[85, 86] Similar scaling behavior, but with an exponential dependence, is observed in nanoparticle dimers, and has been employed as a "plasmon ruler" to measure nanoscale distances.[18]

In this chapter, I simulate the charge distributions and resulting resonant wavelengths of hybridized modes in nanoparticle-film systems. The goal is to understand the physical origin of modes in the coupled system and to understand how particle size and spacer thickness can be used to tune each resonance through the visible range.

4.1. Coupled dipole image model

Hybrid modes in nanoparticle-film systems can be interpreted using a coupled dipole image model. In this view, the nanoparticle plasmon and its image charge are each understood as dipoles. P-polarized light incident at an angle can excite

64

two dipole alignments. The first, called the horizontal coupled dipole (HCP) mode is excited by the parallel electric field component, and both the particle and image dipole align parallel to the substrate. The vertical coupled dipole (VCP) mode is excited by the perpendicular electric field component and both dipoles align perpendicular to the substrate.[63, 87] The HCP and VCP are shown schematically in Fig. 4.1.
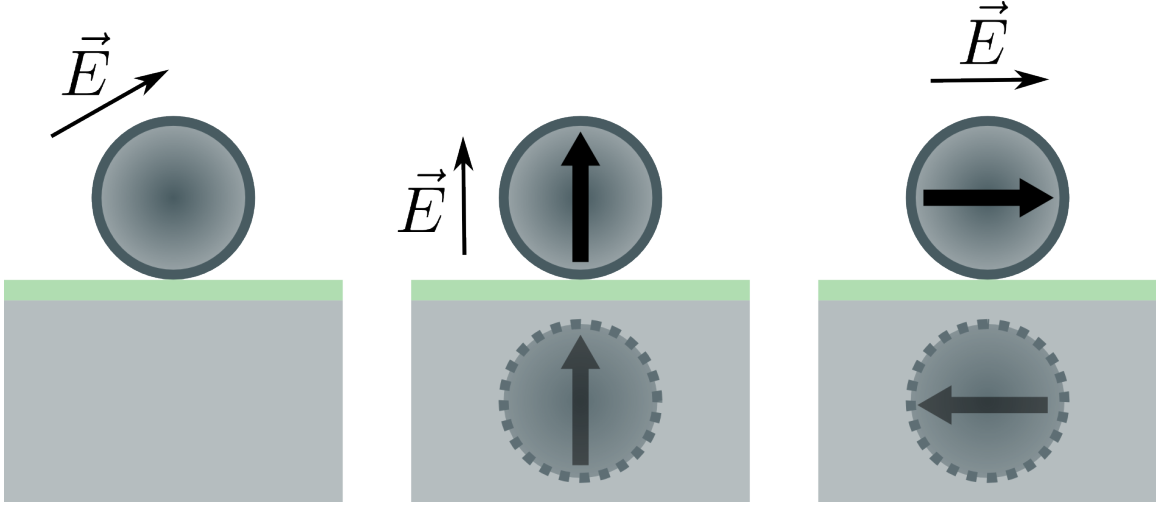
FIGURE 4.1. Schematic of horizontal and vertical particle-film coupled modes. (Left) schematic of architecture, illustrating p-polarized radiation incident at 45 degrees. (Center) schematic of vertically-coupled plasmon (VCP) mode. (Right) schematic of horizontally-coupled plasmon (HCP) mode.

The coupled mode energies can be calculated using electrostatics. The dipole interaction energy is given by

$$U = \frac{1}{4\pi\epsilon_0}\frac{1}{r^3}[\vec{p_1}\cdot\vec{p_2} - 3(\vec{p_1}\cdot\hat{r})(\vec{p_2}\cdot\hat{r})].$$
(4.1)

The interaction energy for the HCP becomes

$$U_H = -\frac{1}{4\pi\epsilon_0}\frac{1}{r^3}(|p_1|\,|p_2|),$$
(4.2)

65

and the energy for the VCP becomes

$$U_V = -2\frac{1}{4\pi\epsilon_0}\frac{1}{r^3}(|p_1|\,|p_2|). \tag{4.3}$$

Since U_H and U_V are both negative, both the HCP and VCP have a lower energy and thus redshift relative to the nanoparticle dipole resonance; that is, the image dipole acts to dampen the particle dipole in both cases. The dipole-dipole interaction becomes weaker with increasing separation (scaling as $1/r^3$), so the coupled mode redshift is largest for the smallest separations. As r changes, the relation $U_V = 2 * U_H$ implies that the energy shift is faster for the VCP than the HCP.

This coupled dipole picture allows us to form expectations for observations. First, the HCP should be measurable at both normal incidence and at larger angles, but the VCP should only be measurable for off-incident angles and p-polarized light. Second, the charge arrangement of the HCP is effectively quadrupolar, while the VCP is effectively dipolar. Consequently, the HCP should have a lower scattering efficiency than the VCP. Finally, in the VCP, the particle dipole can interact with the image dipole only through near-field interactions, which are strongest for small separations. In contrast, the HCP particle dipole can interact radiatively with the light scattered by the image dipole. This interaction can occur over greater distances, so the HCP should be measurable at greater spacer thicknesses than are required to observe the VCP.

Many authors use this simple dipole coupling model as a guide to understand experimental results; however, more complex behavior is also observed. For example, large particles support multipoles which in turn excite multipolar images, and all of these modes can couple under off-normal incidence p-polarized excitation. Also, particle scattering and dielectric spacers can help to overcome the wavevector

66

mismatch which normally prevents surface plasmon polariton (SPP) excitation on flat films in free space; thus the presence of spacers can allow LSP-SPP coupling. We will guide our discussion of coupled modes using the coupled dipole model, and discuss additional complications as they arise.

4.2. Simulating nanoparticle-film coupling via the boundary element method

In order to evaluate the tunable wavelength range of nanoparticle-film (NP-film) systems, we simulate various combinations of flat film material and thickness, spacer film thicknesses, and particle material and sizes. We simulate particles interacting with substrates (either dielectric or metal) using a boundary element method. The boundary element method (BEM) assumes that all objects consist of homogeneous and isotropic permittivities and are separated by one another and their environment by abrupt interfaces.[88] Because only these boundaries, and not the full simulation volume, need to be discretized, the BEM has modest memory requirements and reasonable run times compared to finite element methods.[89] For simulations of layered systems, the layer structure is divided into a grid, within which the Green functions are tabulated. These pre-tabulated Green functions are used in subsequent simulations (for different wavelengths) to save simulation time. Though the BEM is a numeric approach, it calculates surface modes which can be easily visualized. Thus, results can be interpreted in a way consistent with the hybridization description of plasmon-image charge interactions.

We use the Metal Nanoparticle Boundary Element Method (MNPBEM) Toolbox, an open-source boundary element method program in Matlab.[88] Our simulation geometry consists of a metal nanoparticle in vacuum sitting atop a dielectric spacer

layer and a flat metal film, which in turn rests on a thick glass substrate (Fig. 4.2). The primary simulation parameters are nanoparticle radius a, spacer thickness t_d, metal film thickness t_m, the angle θ_0 of incoming TM radiation, and the permittivities ϵ_i of each constituent. We take the substrate and spacer to each have a constant refractive index of 1.5. In all simulations, the nanoparticle boundary was located 1nm above the spacer layer to ensure that none of its vertices were inadvertently assigned the permittivity of the spacer layer.
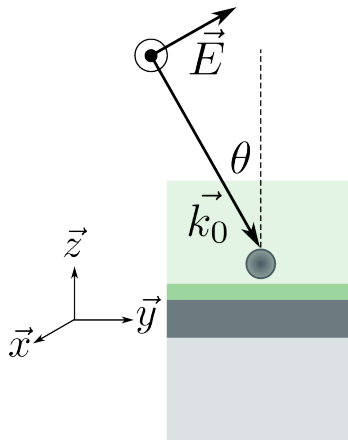
FIGURE 4.2. Nanoparticle-film system simulation geometry.
Particle of radius a and permittivity ϵ_m is separated by a spacer layer of thickness t_d and refractive index 1.5 from a metal film of thickness t_m and permittivity ϵ_m and illuminated with p-polarized light incident at angle θ.

The following parameters control the simulation resolution and time: the number of vertices v in the nanoparticle mesh, the number of points in the z-direction n_z, which sets the z-resolution of the simulation, the wavelength resolution n_e, and the wavelength resolution n_{eg} in the tabulated layer Green function. All simulations use $v = 144$, $n_z = 30$, $n_e = 2.5$, and $n_{eg} = 10$. To test these simulation parameters, we simulated a model system to compare to published results which also used the MNPBEM Toolbox. The model system contains a gold nanoparticle, spacer, and

gold film. Figure 4.3 shows excellent agreement between our calculations and the literature result.

Figure 2. (a) Schematic illustration of the MNPoM structure for the calculation of scattering cross sections and field patterns. (b) Calculated scattering spectra (Au NP diameter: 80 nm; gap length: 4 and 5 nm; gap refractive index: 1.7). Electric field enhancement (|E/E_0|) at the middle of the gap (c) at the scattering peak energy (1.9 eV) and (d) at the excitation energy for PL measurements (3.06 eV) when the gap length is 4 nm.

(a) Results from Reference [90].   (b) Scattering and extinction spectra simulated using MNPBEM.

FIGURE 4.3. Verifying MNPBEM simulation parameters.
We verify simulation parameters by comparing to published results. Simulation architecture consists of a 80nm Au nanoparticle spaced 4–5nm from a 100nm Au film by a spacer with refractive index 1.7. P-polarized light is incident on the structure at a 65 degree angle. There is good agreement between our simulations and published results.

4.3. Understanding the features of simulated spectra

We simulated silver nanoparticles with radii ranging from 20–60nm, on spacer layers in a realistic thickness range of 5–30nm, atop a flat metal film either 50nm or 100nm thick, excited by a TM polarized plane wave incident at either 0 or 45 degrees. To illustrate typical simulated extinction and scattering trends, we examine the R=30nm AgNP on a 50nm Ag film at normal and 45 degree incidence (Fig. 4.4).

(a) Extinction, normal incidence

(b) Extinction, 45 degree incidence

(c) Scattering, normal incidence

(d) Scattering, 45 degree incidence
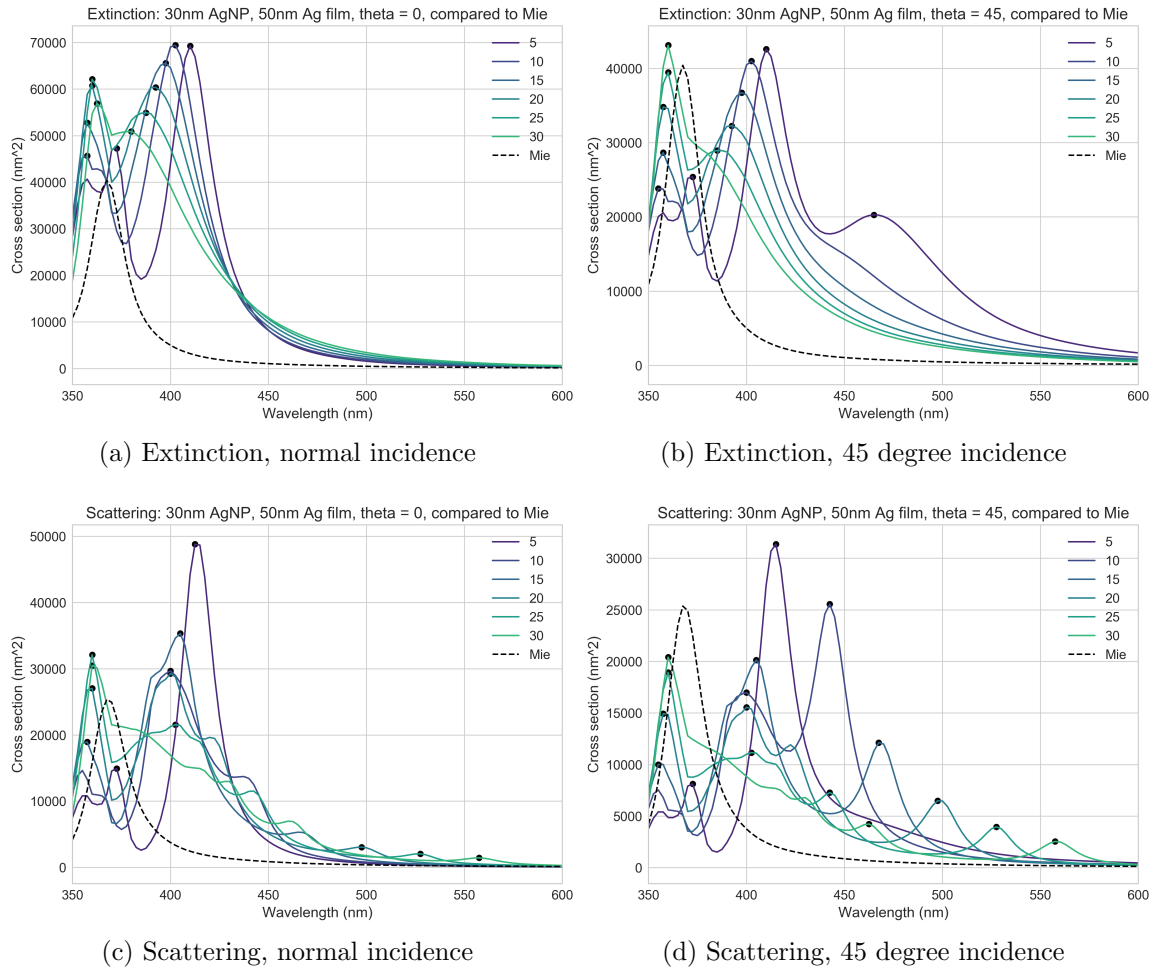
FIGURE 4.4. Spacer thickness effect on simulated spectra.
Layered sample contains a 30nm radius silver nanoparticle above a 50nm flat silver film, separated by a spacer layer of index n=1.5 and with thicknesses (in nanometers) denoted in the legends. The Mie spectrum of a 30nm radius silver nanoparticle in a homogeneous index n=1 environment is shown for comparison (dashed line).

At normal incidence, there are two extinction peaks (Fig. 4.4 (a)). The shortest wavelength peak (360nm) is relatively stationary with changing spacer thickness, while the long wavelength peak redshifts (from 380–425nm) as the spacer becomes thinner. The dipole resonance for the isolated nanoparticle lies between the two

hybridized peaks, at 367.5nm. Another resonance emerges at 465 nm for thin spacers at 45 degree incidence (Fig. 4.4 (b)).

Scattering spectra (Fig. 4.4 (c) and Fig. 4.4 (d)) are similar to the extinction spectra for short wavelengths; however, a number of additional peaks emerge in the red which have no equivalent in the extinction spectra. These ripples are most intense for thicker spacer layers and off-incident illumination, and are greatly diminished if the ground plane thickness is increased to 100nm. The small intensity, spectral coincidence for normal and 45 degree incidence, and harmonic nature suggests that these are higher order hybrid modes potentially enabled by multipolar coupling; i.e., the interaction of an image charge with a multipolar particle charge distribution.

As particle size increases, all peaks shift toward the red (Fig. 4.5). In this way, different nanoparticle radii enable access to different spectral ranges. As spacer layer thickness decreases, longer wavelength peaks tend to redshift more than shorter wavelength peaks. This implies that, at fixed particle size, some resonances will be more tunable than others. We next turn to assigning these resonances to specific modes.
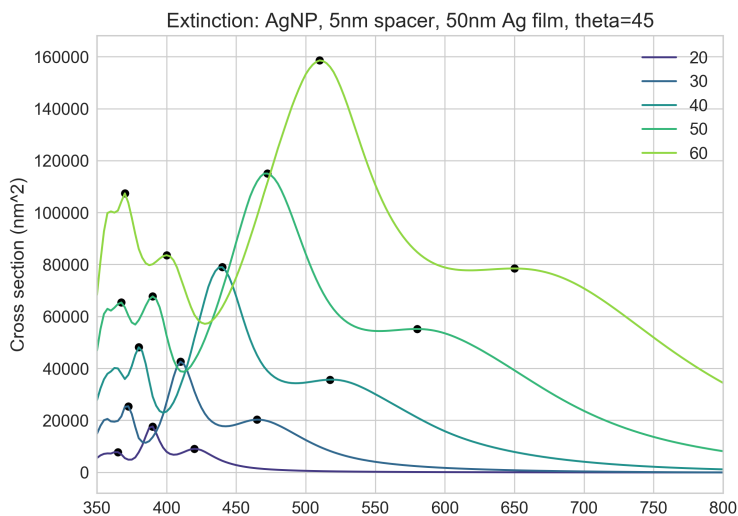
FIGURE 4.5. Effect of nanoparticle radius on nanoparticle-film extinction. Silver nanoparticles with 20–60nm radii are spaced from a 50nm silver film by a 5nm spacer layer. Radiation is incident at 45 degrees.

4.4. Assignment of simulated resonances

To better understand the nature of each simulated resonance, we calculate the nanoparticle charge distributions as well as spatial maps of the electric field at each resonance. We consider a AgNP-PMMA-Ag layered system with a 30nm radius particle, 5nm spacer, and 50nm film. The scattering and extinction spectra at normal and 45 degree incidence are shown in (Fig. 4.6). The 372.5nm, 410nm, and 465nm resonances are indicated by dashed vertical lines.
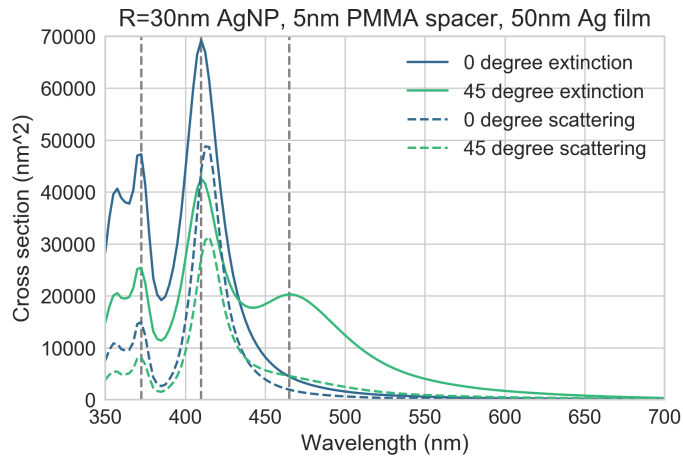
FIGURE 4.6. Simulated extinction and scattering: 30nm AgNP and 5nm spacer. Resonances at 362.5, 410, and 465nm are indicated by vertical dashed lines.

The 372.5nm resonance has a quadrupolar charge distribution, as can be seen in Fig. 4.7 (b). The quadrupole is asymmetric, with a large field strength and charge pileup directly underneath the particle while the rest of the particle has a dipolar field pattern. Of the three resonances, it has the strongest field strength in the spacer region (Fig. 4.7 (g)). This resonance is stronger at normal incidence, as indicated by the field strength and also by the peak height in Fig. 4.6. The mode is mostly absorptive; the absorption cross section (not shown) exceeds the scattering cross section by a factor of two. This is sensible; the quadrupolar mode is dark, but because of the asymmetry, the upper part of the particle acts as a weak dipole. This mode can be interpreted as a hybridized plasmon mode stemming from coupling between the quadrupolar particle plasmon and the dipolar image plasmon.[91]

The 410nm resonance has an asymmetric dipolar charge distribution, which is again strongest at the bottom of the particle (Fig. 4.8 (b)). This leads to a moderate field strength in the spacer, which on average is slightly higher at 45 degree incidence. The image of the particle is clearly seen in the x-component of the electric field profile (Fig. 4.8 (e)). This mode has the highest scattering efficiency of the three modes.

73

The overall scattering and absorption are strongest at normal incidence rather than 45 degree incidence. Due to these factors (dipolar charge distribution, high scattering efficiency, and apparent image dipole), we assign this mode to the horizontally coupled dipole mode (HCP).

The 465nm resonance (Fig. 4.9) is quite different at normal versus 45 degree incidence. At normal incidence, the charge distribution and x-component of the E-field point to a very weak dipole. However, at at 45 degrees, the E-field distribution is more complicated. The charge distribution looks like a nearly vertical dipole, with a strong net charge at the bottom right of the particle and a weak opposite charge spread out over the rest of the surface. This mode is almost solely absorptive and only excited at 45 degree incidence. These factors support the assignment of this mode to the vertically coupled dipole mode (VCP), because it is only observable off-incidence and for thin spacers (strongest near-field coupling).

We have now assigned the main simulated resonances in a coupled nanoparticle-film system. The shortest wavelength resonance at 362.5nm is most likely a quadrupolar particle plasmon interacting with a dipolar image plasmon. The sharpest resonance, at 410nm, appears to be the horizontally coupled dipole mode. The longest wavelength resonance, at 465nm, is only excited at off-normal incidence and is most likely the vertically coupled dipole mode.

(a) 372.5nm, 0 degrees

(b) 372.5nm, 45 degrees

(c) Norm, 0 degrees

(d) Norm, 45 degrees

(e) E_x, 0 degrees

(f) E_x, 45 degrees

(g) E_z, 0 degrees

(h) E_z, 45 degrees

FIGURE 4.7. Charge distributions and field maps of a 372.5nm hybridized mode. The layered system contains a 30nm radius silver nanoparticle, 5nm PMMA spacer, and 50nm flat silver film. Light is either normal incident (left) or incident from 45 degrees (right). From top to bottom: charge distributions, E-field norm, E-field z-component and E-field x-component.

(a) 410nm, 0 degrees

(b) 410nm, 45 degrees

(c) Norm, 0 degrees

(d) Norm, 45 degrees
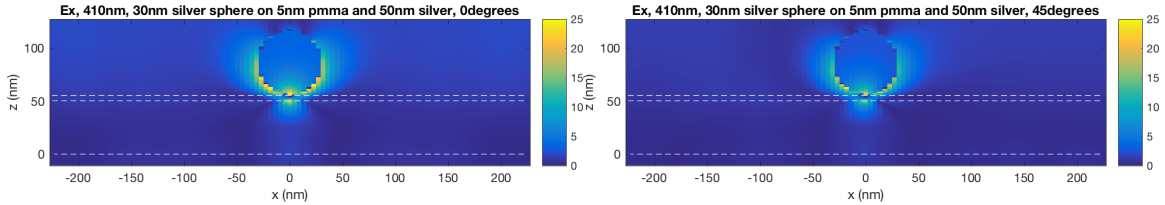
(e) E_x, 0 degrees
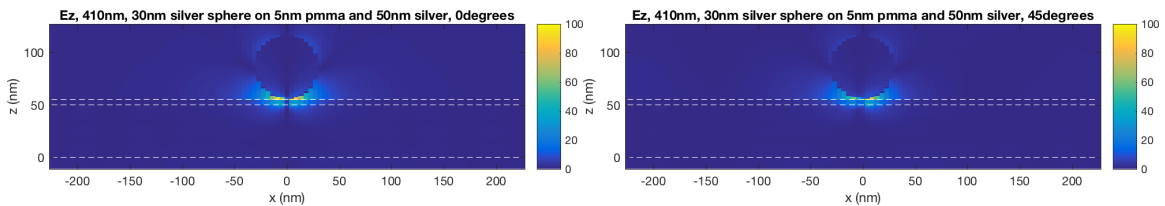
(f) E_x, 45 degrees

(g) E_z, 0 degrees

(h) E_z, 45 degrees

FIGURE 4.8. Charge distributions and field maps of a 410nm hybridized mode. The layered system contains a 30nm radius silver nanoparticle, 5nm PMMA spacer, and 50nm flat silver film. Light is either normal incident (left) or incident from 45 degrees (right). From top to bottom: charge distributions, E-field norm, E-field z-component and E-field x-component.

76

(a) 465nm, 0 degrees

(b) 465nm, 45 degrees

(c) Norm, 0 degrees

(d) Norm, 45 degrees

(e) E_x, 0 degrees

(f) E_x, 45 degrees

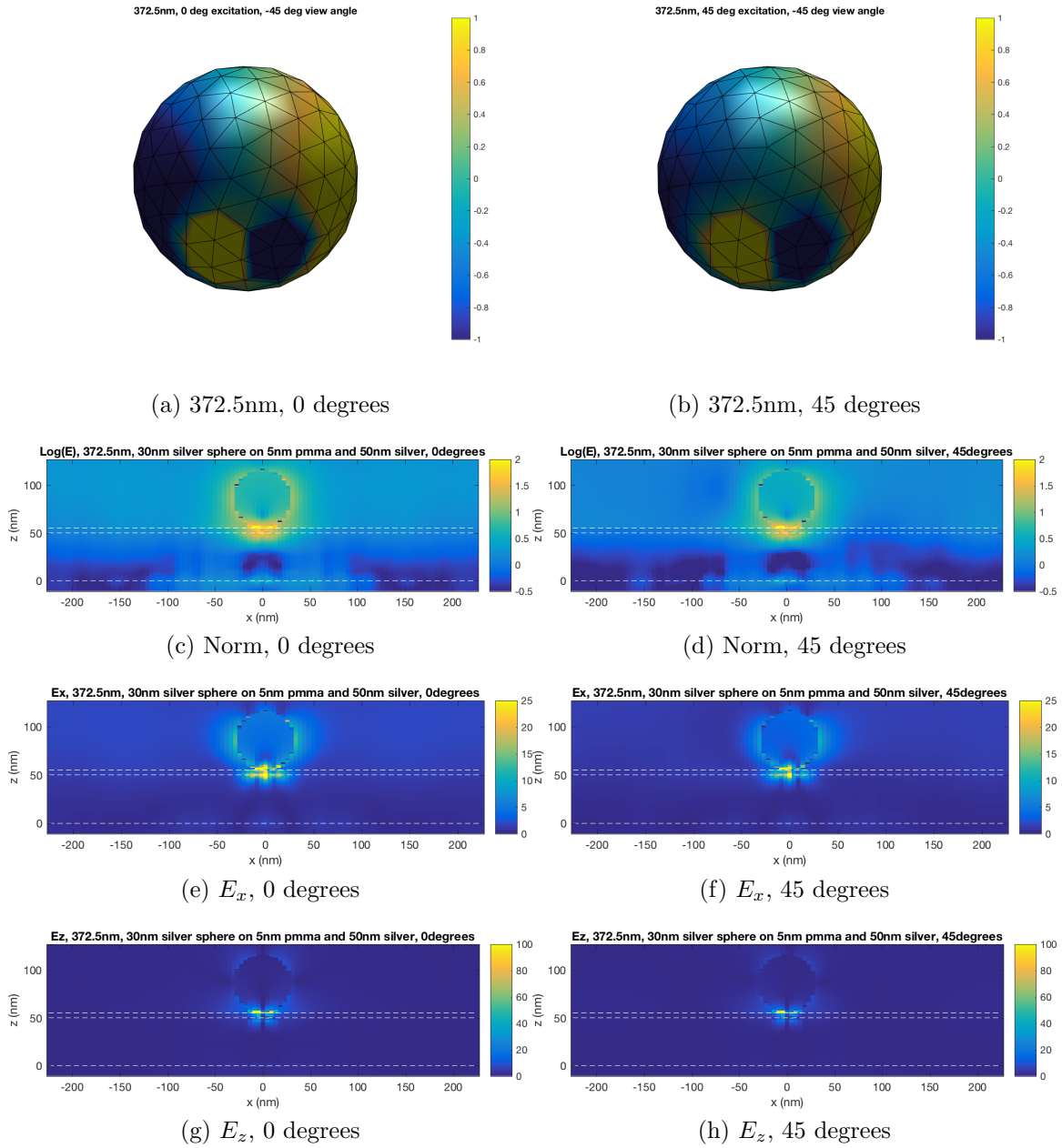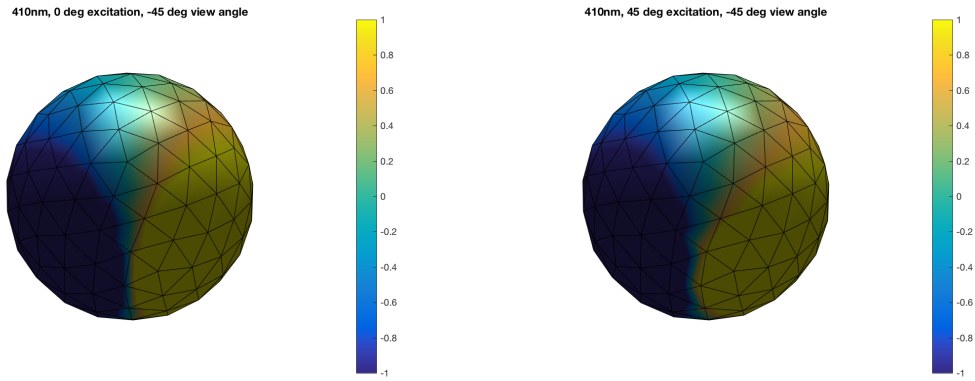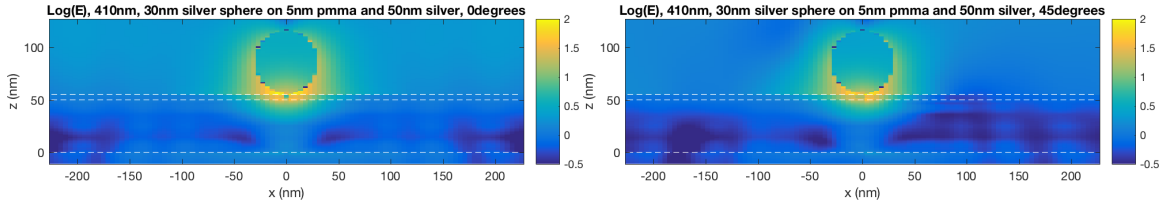(g) E_z, 0 degrees

(h) E_z, 45 degrees
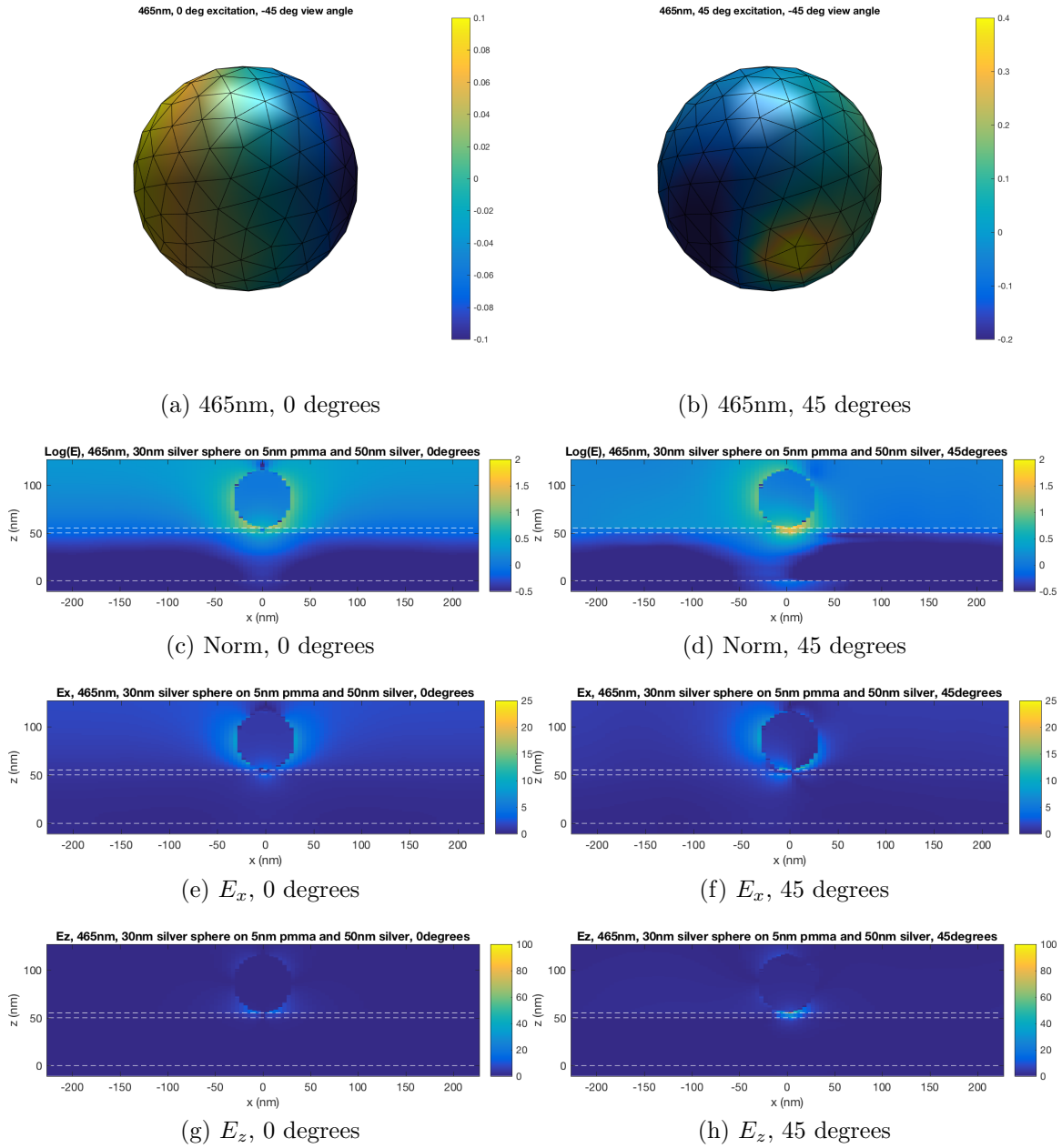
FIGURE 4.9. Charge distributions and field maps of a 465nm hybridized mode. The layered system contains a 30nm radius silver nanoparticle, 5nm PMMA spacer, and 50nm flat silver film. Light is either normal incident (left) or incident from 45 degrees (right). From top to bottom: charge distributions, E-field norm, E-field z-component and E-field x-component.

4.5. Tuning coupled system resonance to 532nm

As has already been mentioned, we would like to tune the wavelength of layered nanoparticle systems around certain absorber and emitter ranges of interest. In particular, 532nm is a popular laser line, and thus tuning to this region provides an opportunity to study enhanced fluorescence in common laser dyes. We thus aim to fabricate layered samples tuned to the 532nm range.

For silver particles on silver films, the tunability range is driven more by the nanoparticle size than the spacer layer thickness. When varying particle radii between 20 to 60nm, The HCP and VCP sweep over 100nm and 200nm worth of tunable wavelength ranges, respectively (Fig. 4.5). In contrast, when particle size is fixed at R =30nm and spacer thickness is varied between 5nm and 30nm, the HCP covers only a 50nm tunable wavelength range (Fig. 4.4 (a)). Because tunability is driven mostly by size, nanoparticle-film systems seeking sharp peaks for fluorescence enhancement, sensing, or surface-enhanced optical spectroscopy are generally fabricated using monodisperse nanospheres. Thus, we choose to fabricate samples using monodisperse particles rather than polydisperse particle island films.

Additionally, we have seen that the HCP mode dominates the extinction spectrum, and is accessible for both normal and off-normal incidence. Therefore, to identify a geometry capable of accessing a 532nm resonance, our design approach is to fix the spacer layer thickness at a moderate range and investigate the HCP extinction peak location as we vary the nanoparticle radius. Extrapolating our calculations, we predict that a 65nm particle radius and 5nm spacer may achieve a 532nm resonance (Fig. 4.10). Since the resonance wavelengths of nanoparticles deposited on substrates tend to be redshifted from their calculated scattering values

by aggregation and substrate effects, it is likely that we will actually access the 532nm resonance with somewhat smaller particles than our projections indicate.
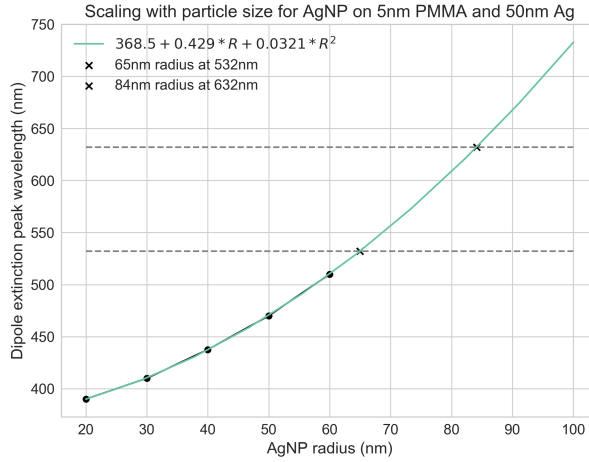
FIGURE 4.10. Projected extinction resonances of layered systems. Resonances for a 5nm spacer layer thickness and 50nm flat silver film are plotted as a function of the silver nanoparticle radius. Dashed gray lines indicate the particle radii projected to achieve 532nm and 632nm resonances are 65nm and 84nm, respectively.

4.6. Summary

In this chapter, I simulated the tunability and scaling of coupled modes in nanoparticle-film layered structures. I found that, of the three modes, the horizontally coupled plasmon (HCP) mode is the most tunable. Additionally, I find that the HCP mode's spectral tunability is influenced more by particle size than by spacer layer thickness. Simulations indicate that a 532nm resonance should be accessible using 65nm radius silver nanoparticles and a 5nm spacer layer. In Chapter V, I pinpoint this resonance by fabricating and characterizing layered systems containing 60nm, 80nm, and 100nm diameter particles.

CHAPTER V

FABRICATION AND CHARACTERIZATION OF NANOPARTICLE-FILM
COUPLED SYSTEMS

The coupled plasmon modes of nanoparticle-film systems can be spectrally aligned for different functions, such as enhanced fluorescence for molecular sensing,[92] enhanced luminescence and energy transfer in quantum dot phosphors,[90, 93] and FRET-like energy transfer in nanoscale donor-acceptor systems.[87, 90, 91, 94] Spectral tunability in nanoparticle-film systems is typically achieved by carefully choosing spacer thicknesses.[33, 95] The spacer thickness (and thus resonance) has even been modulated in-situ using pH-induced swelling of polyelectrolyte spacers,[96] voltage-controlled electrophoretic forces in molecular layers,[85] swelling and contracting a hydrogel,[97] and reversibly photoisomerized photochromic molecules in the gap region.[98]

In this chapter, I discuss the range of tunability demonstrated in prior experimental work in this area and highlight an opportunity to access the blue and green parts of the spectrum. I then fabricate layered samples and measure their response via angle resolved reflectance spectroscopy, in order to pinpoint the parameters capable of producing a 532nm resonance.

5.1. Scaling and tunability of plasmonic modes in nanoparticle-film systems

Most of the nanoparticle-film coupling literature is dominated by gold particles on gold films.[33, 61, 85, 87, 90, 91, 93, 95–97, 99, 100] This is probably due mostly to gold's stability in air (as silver-based architectures are prone to oxidation and the formation of silver sulfides)[33], and because it is easy to synthesize monodisperse

and shape-controlled gold nanoparticles via the citrate method. An example of the tuning ranges for 60nm gold particles on 30–50nm gold films, extracted from literature sources, is shown in Fig. 5.1;[33, 85, 95] the studies shown achieve tuning ranges between 540nm and 675nm. Gold nanoparticle response is generally in the range of 550-700nm. From the perspective of application to absorption and emission enhancement, this is beneficial for absorbers in the HeNe laser range. Tuning toward the 532nm frequency-doubled Nd:Yag line opens up the possibility of applications using fluorophores which absorb in the green and blue. Silver may enable tuning into this range because its interband transitions are in the UV, unlike the visible range transitions for gold. However, there have been comparatively fewer studies of silver particles on either silver or gold films (notable exceptions are investigations of monodisperse silver particles on gold films by Hu *et al.* ([63]) and of thermally-evaporated silver islands on silver films by Szmacinski *et al.* ([94]).
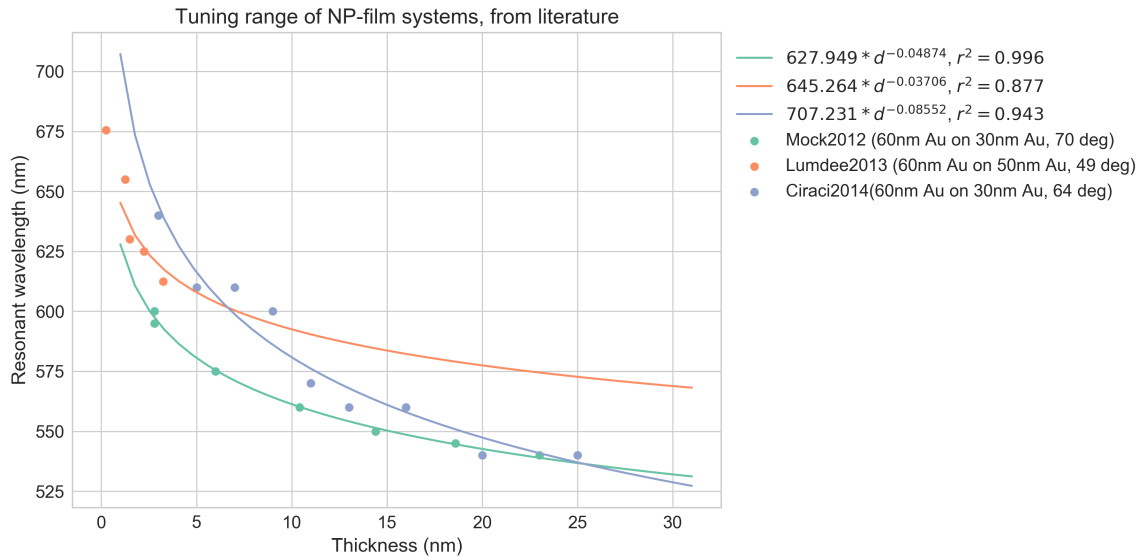
FIGURE 5.1. Tuning ranges for gold nanoparticle-film systems.
Data extracted from references and power law scaling added.[33, 85, 95]

Additionally, much of the present literature measures the response of single particle-film systems using dark field microscopy. There are several advantages of single particle studies as compared to ensemble measurements: first, subtle features are not swamped by inhomogeneous contributions, and therefore resonance line widths can be accurately measured.[63] Second, since most theoretical models and numerical simulations are based on single nanoparticle-film systems, the comparison between experiment to theory is direct. Third, the lack of inhomogeneous broadening for single particle-film systems is essential in applications requiring high quality factors (narrow line widths). On the other hand, single-particle measurements are more expensive and cumbersome. More importantly, averaging over many single particle-film systems can yield a more robust and universal gap-dependent response, precisely because monodisperse nanoparticle preparations are never exactly monodisperse. Thus, measuring single particle-film response with a changing spacer thickness can yield misleading gap-response information as the individual systems may each contain particles of differing sizes.[96]

For these reasons, we seek to measure the ensemble-level gap-dependent response of nanoparticle-film systems containing silver nanoparticles. We fabricate samples, characterize their geometries, and measure their off-incidence ensemble reflectance. We compare measurements to simulations, using differences between the two to understand the impact of practical experimental conditions on gap-dependent response. Finally, we develop a material system tuned to the 532nm green laser line.

5.2. Fabrication of nanoparticle-film systems with nanometer polymer spacers

We fabricate nanoparticle-film systems by evaporating silver on glass substrates, spin-coating PMMA spacers ranging from 2–20nm, and spin-coating silver or gold nanoparticles suspended in isopropanol. Flat, 50–70nm silver layers were thermally evaporated onto clean glass slides using the Angstrom Engineering AMOD physical vapor deposition system. Pellets obtained from the Kurt H. Lesker Company served as the evaporation source, and films were deposited at a rate of 5 Å/sec in a chamber pumped to $2 * 10^{-6}$ Torr. Next, PMMA films were spin coated atop the silver films at 3000rpm for 60 seconds from solutions of PMMA in an anisole-ethanol mixture, and subsequently annealed for 5min on a 180°C hotplate. The ethanol concentration was held constant at 20% by volume to adjust the solvent evaporation rate and allow for the possibility of doping with ethanol-soluble dyes. PMMA concentrations ranged from 1 - 12 mg/mL to achieve thicknesses between 2 - 20nm. Monodisperse silver and gold nanoparticles were obtained from NanoComposix, Inc. They were resuspended in isopropanol to a concentration of about 10^{11} particles/mL. Particles were dispersed onto prepared substrates by spin coating a volume of 40μL at 2000rpm for 40 seconds. All samples were stored in a nitrogen environment between deposition steps and after fabrication was complete.

Silver and PMMA film thickness measurements

Thicknesses of PMMA and silver were measured simultaneously using a Woollam variable angle spectroscopic ellipsometer. Alignment was performed at 65 degrees, assuming a 0.5 mm sample thickness, and spectra were acquired in 10 degree increments between 55 and 75 degree incidence angles for 1 second each. The

fitting model assumed a glass substrate, silver film of variable thickness (initial parameter guess: 50nm) and PMMA film of constant refractive index 1.489 and variable thickness (initial parameter guess: 10nm). The wavelengths used for fitting were limited to 350–800nm. While ellipsometry can be susceptible to error as it relies on modeling, it is the fastest and least invasive thin film characterization method available (compared to stylus profilometry, optical profilometry, AFM, or attenuated total reflectance methods). Accurate measurements of silver film thickness is difficult, because the measurement relies on the beam penetrating the sample, which is limited by the skin depth of the film. However, we can independently verify the PMMA thickness measurements via attenuated total reflectance (ATR), and use the verified results to bolster our confidence in the fast and minimally-invasive ellipsometry measurements.

In the ATR technique, the sample is mounted to a BK7 glass prism, in order to excite a surface plasmon polariton (SPP) at the silver-PMMA interface using a 632.8nm laser incident at the resonance angle (Fig. 5.2a). As the PMMA thickness increases, the SPP resonance shifts to higher angles, so locating the resonance angle provides a measurement of a sample's PMMA thickness.

For a system comprising a prism with permittivity ϵ_0, a metal film of permittivity ϵ_1 and thickness d_1, a polymer film of permittivity ϵ_2 and thickness d_2, and finally an air layer, the resonance angle is given by:

$$k_x = \frac{\omega}{c}\sqrt{\frac{\epsilon_1' * \epsilon_2}{\epsilon_1' + \epsilon_2}} \tag{5.1}$$

For small thicknesses d_2, the angle displacement relative to $d_2 = 0$ is linear:

$$\Delta k_x = \frac{\omega}{c} \frac{\epsilon_2 - 1}{\epsilon_2} \left(\frac{|\epsilon_1'|}{|\epsilon_1'| - 1} \right)^2 \frac{|\epsilon_1'| + \epsilon_2}{|\epsilon_1'| + 1} \frac{1}{\sqrt{|\epsilon_1'|}} \frac{2\pi d_2}{\lambda} \tag{5.2}$$

The approximation is valid for $k_{z,2}' d_2 << 1$, which holds for $d_2 << \lambda_0/(2\pi n_2)$.[101] At our operating wavelength of 632.8nm and $n_2 = 1.4887$, the linear approximation should strictly hold up to about 6–10nm. In practice, it appears to hold to about 20nm. Thicknesses obtained from ATR measurements agree with ellipsometry results to within 1nm, as shown in Fig. 5.2b.

(a) Attenuated total reflectance setup
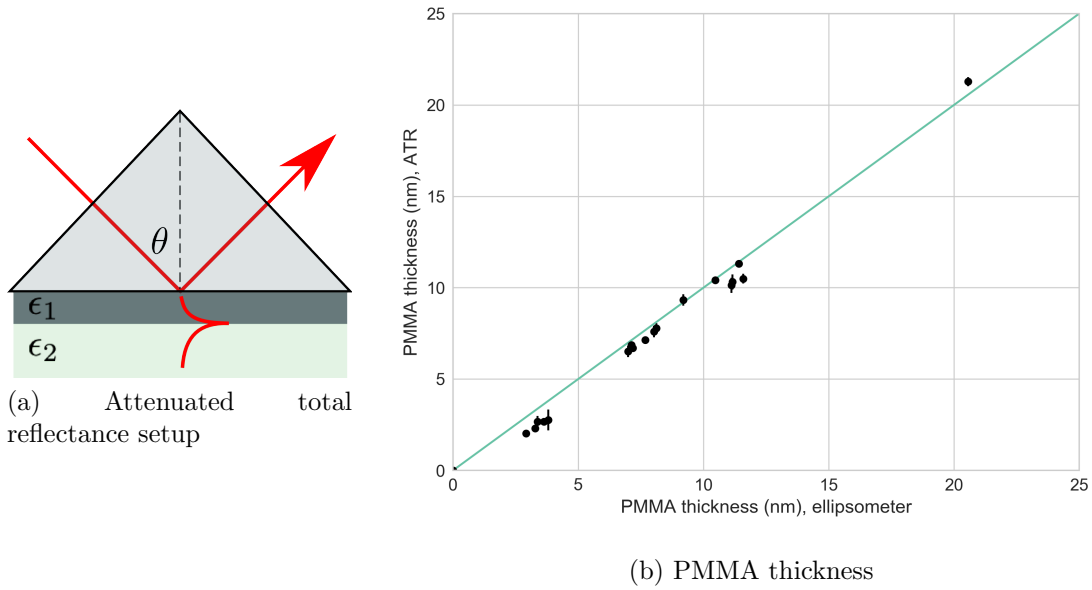
(b) PMMA thickness

FIGURE 5.2. PMMA thickness measurements.
Measurements of PMMA thickness using an ellipsometer (fast and non-invasive) differ from measurements using attenauted total reflectance (non-invasive, but slow) by less than 1nm on average, validating the use of ellipsometry to measure PMMA films thinner than 20nm.

5.3. Spin-coated nanoparticle morphology

SEM images of particles spun on PMMA films on glass were acquired on an FEI Helios SEM. Some samples (the 80nm diameter and 100nm diameter particles) were prepared by swabbing an edge with acetone to remove PMMA, in order to expose the underlying silver film which could then be grounded to the SEM stage using conductive tape. The 60nm diameter particles were imaged without an underlying silver film and so this step was omitted. Some images were cropped during analysis in order to avoid areas of severe charging.

Samples containing 60nm, 80nm, and 100nm diameter silver nanoparticles are shown in Fig. 5.3. Each sample has approximately 1% surface coverage. Particles appear to be well-dispersed over the surface, with a smattering of small aggregates typically containing 2–3 particles. Very large aggregates of particles, such as those which form in the Tollens reaction, do not occur in these colloidal systems.

Apparent background texture

Aside from the disperse spatial distribution and small number of low-N aggregates, we observe several other interesting features. First, the substrates in the images of 80nm particles appear grainy, like evaporated metal films typically appear. It is probable that this is the underlying flat silver film, perhaps visible through the 4.7nm PMMA film due to efficient grounding. However, the underlying substrate in the 100nm diameter images doesn't appear grainy; either the 5.4nm PMMA layer is more electron-opaque than the 4.7nm PMMA film, or the grounding was less efficient for the 100nm particle samples. Second, the 100nm particles looked as if they were partially embedded within the film - bright particles seem closer to the surface while the dim particles appear as if they are partially embedded within the

86

film. It is unclear whether the 100nm particles are in fact partially embedded. AFM measurements would help to clarify this, by allowing simultaneous morphological and electronic measurements using Scanning Capacitance Microscopy (SCM) or Tunneling AFM (TUNA) in Peak Force mode.

(a) 60nm

(b) 80nm

(c) 100nm
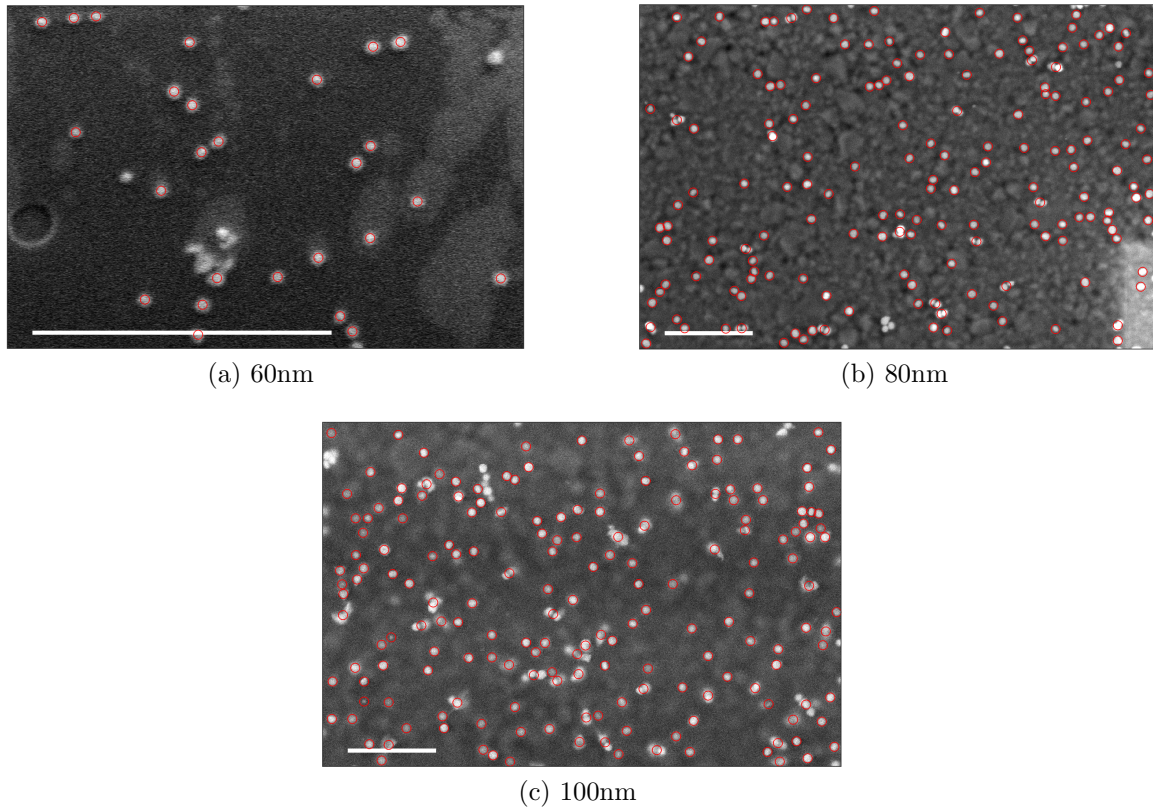
FIGURE 5.3. SEM of silver nanoparticles spun on PMMA films.
Samples have an average surface coverage of approximately 1% (9, 7, and 5 particles per square micron, from left to right). All scale bars are 1 micron. Red circles are individual particles identified using MATLAB.

An alternative explanation for the visibility of the evaporated silver substrate in the image of 80nm particles is that the PMMA film is washed from the substrate during the nanoparticle deposition process. PMMA is "conditionally resistant" to isopropanol (IPA), which is the suspension medium for these nanoparticles. It is possible that the short contact with the IPA during the spin coating process partially

dissolves or softens the PMMA films. It is also possible that the IPA might dissolve the thinner films more readily, and maybe could even wash away the thinnest PMMA films. To investigate this possibility, one could conduct ellipsometry on a PMMA-Ag film before and after contact with plain IPA solution using the same spin coating methods as for nanoparticle solutions. If the thickness is larger before than after, the IPA may indeed be damaging the PMMA films. However, the optical resonances we measure in this chapter are consistent with the assumption that the PMMA is indeed on the surface. Therefore, I find it unlikely that the PMMA is entirely washed away. It may, however, be thinned by the spin coating process. Understanding whether any partial dissolution or softening occurs in this system may provide valuable information for understanding the morphology and optical response of samples containing 100nm particles, which as we shall see is particularly unique.

Image Analysis

In order to estimate surface coverage and average nearest neighbor separation, images were analyzed using MATLAB. As in Chapter III, images were thresholded and smoothed with a gaussian kernel. Particle centroids were identified using MATLAB's built-in imfindcircles function, and centroid positions were used to tabulate nearest neighbor distances for each particle.

This particle identification procedure has some characteristic problems: first, less than 100% of particles are properly identified, especially in lower resolution images, mostly due to the difficulty of thresholding to eliminate noise without eroding some particles. Additionally, sometimes dimers are misidentified as single particles, and particles within larger aggregates often aren't detected at all. This is because particles sometimes merge under the thresholding and filtering operations, producing

a single non-round object whose constituents cannot be identified as individual separated circles. Our analysis procedure may be used to estimate surface coverage and interparticle separation, which can be used to classify a sample's morphology and anticipate its optical response. However, more extensive measurements and careful analysis would be necessary to provide statistically significant morphology information for use in modeling.

Morphological results

SEM analysis results are summarized in Table 4. The measured particle diameter is around 10nm smaller than the size quoted by the manufacturer; this is probably an artifact of the thresholding and smoothing process which erodes particle size. This erosion should not appreciably affect the centroid position or the nearest neighbor distances.

Particles can be considered to be independent scatterers (i.e. not couple with one another via near-field) if their center-center distances are greater than about four times their radii.[27] Thus we calculate the fraction of independent scatterers f_{ind} for which the distance to the nearest neighbor satisfies the criterion $d_{NN} > 4R$. The average nearest neighbor distance ranges between 180–270nm, and the fraction of the distance distribution which are approximately independent, f_{ind}, is in the 60–80% range. This implies that about 20–40% of particles are members of aggregates.

5.4. Spin-coated nanoparticle extinction

To understand the nanoparticle extinction at our concentrations, we measured the extinction of silver nanoparticles on glass substrates coated with a thick layer of PMMA. The PMMA coating is added to create a surface chemistry consistent

Sample	60nm Ag	80nm Ag	100nm Ag
Quoted diameter (nm)	60 ± 6	78 ± 9	102 ± 11
Measured diameter (nm)	46 ± 6	68 ± 6	110 ± 10
Quoted polydispersity	9.5%	11.6%	10.7%
Concentration $(/mL)$	$10 * 10^{10}$	$5 * 10^{10}$	$3 * 10^{10}$
Density $(/\mu m^2)$	9	7	5
Surface Coverage	0.6%	1%	1%
d_{NN} (nm)	188 ± 51	209 ± 21	262 ± 22
f_{ind}	72%	64%	71%

TABLE 4. Morphological attributes of silver nanoparticles on PMMA.

with the full layered system, thus ensuring equivalent morphologies for nanoparticles measured alone and in layered systems.

The extinction of 60nm, 80nm, and 100nm silver nanoparticles on PMMA-glass substrates are shown as solid lines in Fig. 5.4. These are compared to Mie simulations (dashed lines in Fig. 5.4) for monodisperse particles of the same size in a uniform $n = 1.49$ index matrix (the chosen index is an average index to account for a substrate effect to first order). The measured extinction peaks are redshifted and broadened from the simulated results. The redshift is about 10nm for the smaller particles but nearly 40nm for the 100nm diameter particles. Additionally, measured peaks are redshifted from the manufacturer-quoted values for the absorbance of nanoparticles in aqueous solutions (refractive index $n = 1.33$). The measured, simulated, and quoted extinction peak values for these particles are summarized in Table 5.
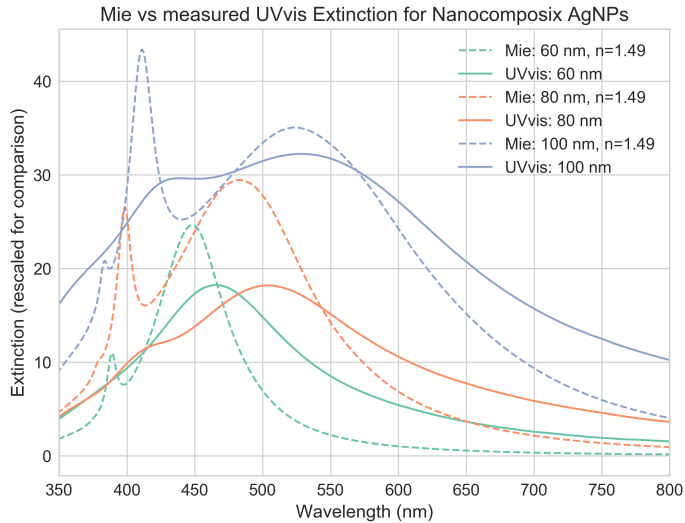
FIGURE 5.4. Measured and simulated extinction of 60, 80, and 100nm diameter silver nanoparticles.
  (Solid lines) Smoothed measured extinction spectra from particles deposited on PMMA-glass substrates from solutions with $10^{10} - 10^{11}$ particle/mL concentrations.
  (Dashed lines) Mie simulations for spheres in a refractive index environment of n=1.49. Spectra are arbitrarily normalized for comparison.

Sample	60nm	80nm	100nm
Polydispersity	9.5%	11.6%	10.7%
Nanocomposix quote (aqueous, nm)	430	461	486
Uncovered UVvis peak (nm)	459	500	530
Covered UVvis peak (nm)	462	500	-
Redshift from NanoComposix quote (nm)	30	39	44
Simulated extinction peak (n_{env}=1.49)	448	489	492
Redshift from simulated peak	11	11	38

TABLE 5. Measured and simulated extinction peaks of silver nanoparticles.

The spin-coated particle resonance may be redshifted from aqueous values because of aggregation on the substrate (leading to interparticle coupling), inhomogeneous shapes and polydispersity of the nanoparticles, the presence of the PVP layer on the NP surface, interaction with the substrate, or multiple factors. If polydispersity were the main driver of the redshift, we would expect a larger redshift and broadening for the sample with greatest polydispersity. However, the

100nm particles have the greatest redshift while the 80nm particles have the largest polydispersity. Thus, we conclude that the polydispersity is less influential than aggregation, and hypothesize that aggregation and substrate effects are the primary drivers of the observed redshift and broadening. In particular, though the substrate effect seems to account for the bulk of the redshift, the broadening of the measured extinction probably stems from aggregation.

The fact that we cannot uniquely determine the origin of the precise redshift magnitude for each type of nanoparticle is not a problem: though it does prevent strict quantitative comparison with simulation results, we can still expect the simulated trends for spacer layer thickness and for particle size to be useful guides for layered experiments.

5.5. Measuring nanoparticle-film coupling

To measure coupled resonances in the nanoparticle-film system, we measured the reflectance spectra of p-polarized light incident at 45 degrees using a home-built angle resolved spectroscopy system. Typical spectra have a noise level up to about 0.1 under 425nm due to a combination of low lamp power and grating efficiency, but from 425–750nm noise is less than 0.05. The size of the focused probe waist at the sample is about 500μm, so this measurement averages over a large ensemble of particles on the surface. Nanoparticle-film sample spectra were normalized to spectra of flat silver films with PMMA coatings. Normalized spectra were smoothed and scaled to their minima for ease of comparison.

To understand the nature of the resonance probed in this setup, we compare p- and s-polarized illumination. An example of a typical resonance is shown in Fig. 5.5. The p- and s-polarized measurements at 45 degree incidence are similar, confirming

that the measured mode is not the vertically-coupled plasmon (VCP) mode, which can only exist for p-polarization. Chapter IV revealed that the hybridized mode (consisting of the particle quadrupole coupled to image dipole) is both weaker and shorter-wavelength than the horizontally-coupled plasmon (HCP) mode. Since we only observe only one mode here, it seems likely that we are measuring the HCP.
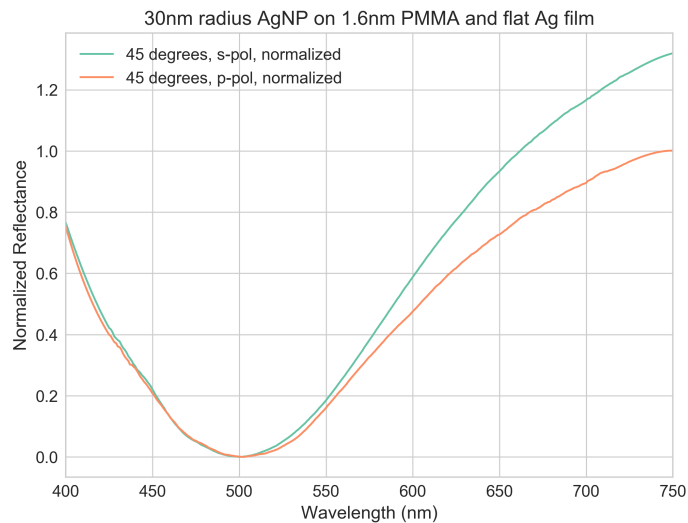
FIGURE 5.5. Example angle resolved reflectance spectra of layered samples. Both s- and p- polarizations show a similar resonance lineshape at 45 degree incidence.

5.6. Coupled system response: 60 and 80nm particles

Normalized reflectance spectra (under p-polarized illumination) of samples containing 60nm and 80nm diameter silver nanoparticles are shown in Fig. 5.6. As predicted, the layered sample resonances are redshifted from the plain nanoparticle extinction for all spacer layer thicknesses. As the PMMA spacer layer thickness decreases, the reflectance minimum redshifts.
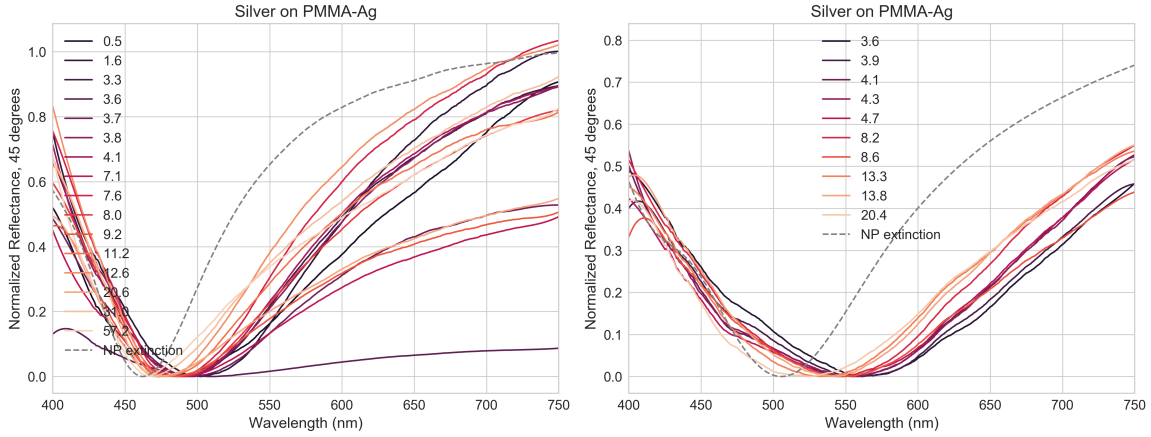
FIGURE 5.6. Coupled system reflectance spectra.
The characteristic plasmon dip of layered samples containing 60nm (left) and 80nm (right) silver particles is compared to the inverted extinction $(1 - E)$ of the same nanoparticles on PMMA-glass substrates (gray dashed line).

Following Mock *et al.*, we extracted the resonance minima and fit their dependence on thickness with a power law.[85] The power law scaling of measured and simulated values is compared in Fig. 5.7. For 60nm particles, we can access a tunability range of 465–510nm. For 80nm particles, we can access a 525–560nm range, and achieve a 532nm resonance with a 13nm spacer. Samples near this critical thickness are good candidates for enhancing emission in spacer layers containing the laser dye Rhodamine 6G.
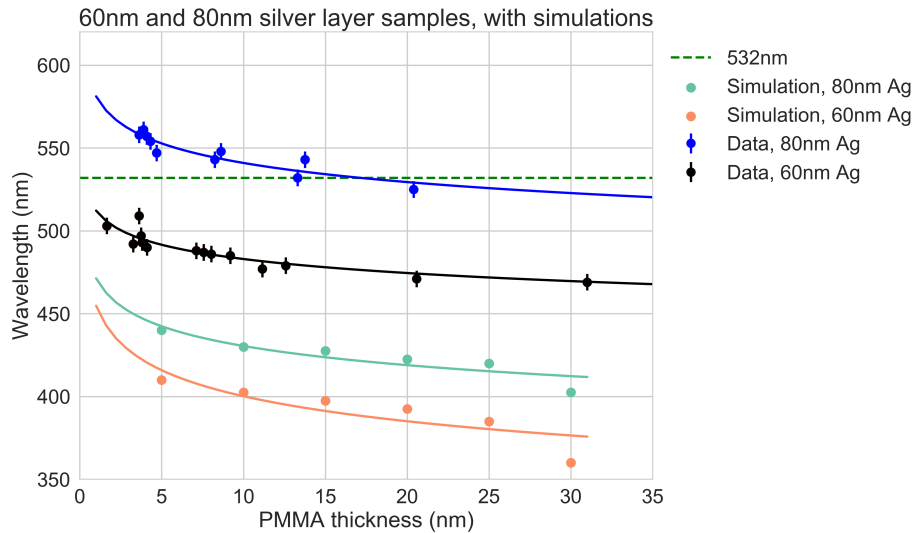
FIGURE 5.7. Power law thickness dependence of layered sample resonances. Measurements are compared to simulations at 45 degree incidence for different silver nanoparticle diameters. Dashed lines indicate the extinction peak location for nanoparticles on PMMA-glass substrates, and the green dashed line indicates the target 532nm resonance.

5.7. Assessing differences between experiment and simulation

The experimental results for 60nm and 80nm particles are redshifted by about 80nm from the simulated results in Fig. 5.7. This difference is most likely due to the aggregation and substrate effects discussed in section 5.4. In the sections that follow, we delve into some of these possibilities.

Embedding permittivity effects

First, it is possible that the nanoparticles are partially embedded within the PMMA. However, PMMA has a high elastic modulus, so it seems unlikely that the particles become embedded because of their weight as they have been found to do on soft polymers such as P3HT.[87, 100] Additionally, while SEM images in section 5.3

95

seemed to indicate that the 100nm diameter particles did indeed partially embed, the 60nm and 80nm particles did not seem to show such embedding.

Second, it is possible that the surface roughness of PMMA (typically 10nm RMS, measured via AFM on thick, flat PMMA films on glass) leads to a significant difference in the effective index of the particle environment. The effective index would take on a value between 1 and 1.5 based on the degree of the embedding.

Third, for small thicknesses, the refractive index of PMMA may be thickness-dependent. An ellipsometric study of ultra-thin PMMA films spun from toluene solutions onto silicon wafers found that while the average index of films greater than about 40nm thickness is n=1.5, the index rises as the thickness falls, to n=1.527 for 25nm films through n=1.84 for 4.6nm films, all the way to n=1.9 for 2.8nm films (Fig. 5.8).[102]

Thickness-dependent refractive index of PMMA

$0.550 * e^{-0.011 * t_d} + 1.495$
Walsh 2003 data
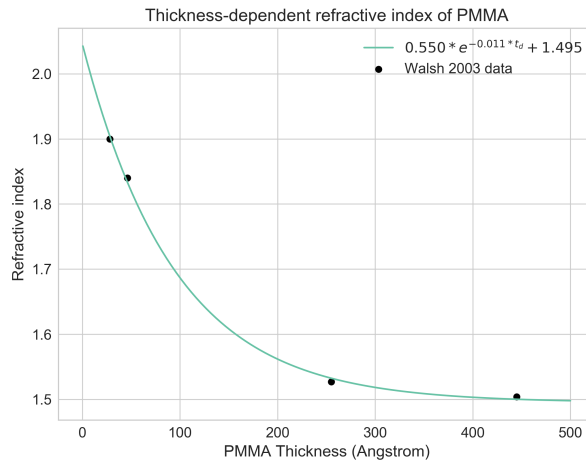
FIGURE 5.8. Thickness-dependent PMMA refractive index.
A thickness-dependent index formula is found using an exponential fit to the mean refractive index values of PMMA measured by Walsh and Franses.[102]

In order to assess the impact of a higher embedding permittivity, we simulated particles in various refractive index environments for light at 45 degree incidence.

First, we consider particles embedded not in a layer system but in a homogeneous dielectric environment with effective refractive index $n_{eff} = .5*(n_{pmma}(t_d)+1)$, where $n_{pmma}(t_d)$ is the thickness-dependent index shown in Fig. 5.8. Next, we consider particles to be fully embedded within that thickness-dependent index, such that $n_{embedding} = n_{pmma}(t_d)$. Finally, we consider a layer structure in which the spacer layer takes on $n_{spacer} = n_{pmma}(t_d)$, while the rest of the layer environment is air. These, along with the simulations of 60nm diameter particles in the original layer architecture, are shown in Fig. 5.9.
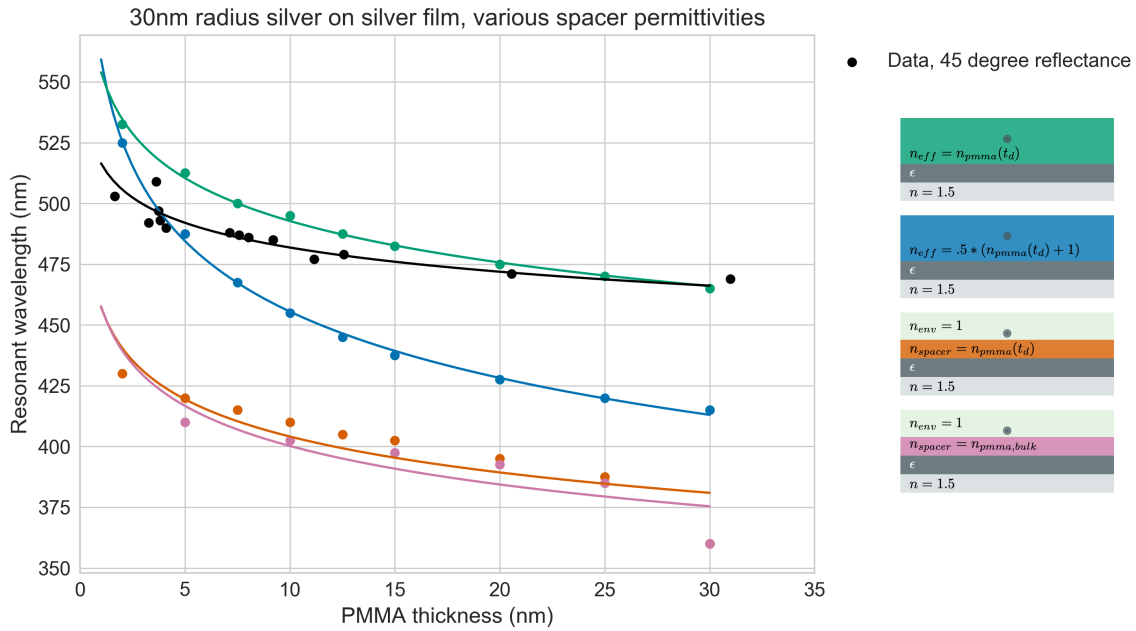
FIGURE 5.9. Measured vs simulated resonant wavelength scaling. Simulated values use various permittivities of the embedding dielectric environment. All simulations are for 45 degree incidence.

The layered system simulations are very similar whether the PMMA permittivity values are taken to be thickness-dependent (orange curve in Fig. 5.9) or identical to the bulk (pink curve). The two effective index simulations ($n_{eff} = .5*(n_{pmma}(t_d)+1)$ in blue and $n_{eff} = n_{pmma}(t_d)$ in green) have an HCP redshifted by more than 100nm

relative to the original layered environment (pink curve). The measured data falls in between the two effective index simulations. This suggests that some intermediate effective index would indeed fit our data. However, this effective index would depend on the microscopic morphology of the PMMA. As we can see, the distance between the measured points and simulated curves is not constant with thickness. Because the surface roughness and size/density of pinholes may well depend on the thickness, a different effective index would conceivably need to be found for each sample.

<u>Silver permittivity effects</u>

The best correspondence I have found between experimental data and simulations for nanoparticle-film systems uses a hydrodynamic model within a finite element method to describe the response of gold nanoparticles ensembles on gold films. A saturation of the resonance redshift with decreasing gap size, and an upper limit to the field enhancement factor, are the main consequences of the nonlocal response of the metal at small gap sizes.[32] The resonant wavelengths calculated using the local and nonlocal theories begin to diverge for spacer layers under about 3nm.[33] To make quantitative comparisons between experiment and theory, the spacer layer's refractive index was used as a fitting parameter. This refractive index parameter was fit using large spacer thicknesses of 20–30nm, and the best correspondence is found for a refractive index of 1.8, which is larger than the refractive index of the bulk spacer material (1.77 for crystalline alumina). The spacer permittivity calculated using this fitting was used in subsequent numerical simulations for thinner spacer layers. While this approach is reasonable, it still relies on an empirical parameter.

Aggregation effects

In section 5.4, we hypothesized that the broadening of measured spectra is impacted more by aggregation than by permittivity effects. This may also be true in the layered system. A weighted approach similar to the weighted Mie system in Chapter III, but using the response of NP-film constituents rather than single nanoparticle constituents, may help our model yield more quantitatively accurate results. We would consider two main constituents: a single NP-film system with filling factor f_s and a NP-film dimer with spacing d_1 and filling factor f_{d1}. Additional dimer terms may be added for additional spacings d_n, following a distribution informed by morphological data.

Recommendations for future simulations

For the purposes of quantitatively predicting plasmon mode tunability, it is desirable to refine our simulation technique to achieve better quantitative agreement with experimental measurements. Additional information about the microscopic morphology of these samples (from AFM, TEM, and SEM) can help to guide simulations toward a proper choice of the embedding refractive index of the particles at the PMMA-air boundary. Likewise, more detailed knowledge of material properties (from XRD) may yield insight into chemical composition, helping us to decide whether to include the effects of oxide and sulfide layers, rather than relying on the experimentally-tabulated silver permittivity values. Finally, morphological information about particle distribution on the surface (from SEM) can help to devise a size-distributed BEM model for sample response which may be fruitful given that 20–40% of particles may belong to aggregates.

Additionally, as we discussed in Chapter II, the hydrodynamic model for nonlocality introduces an additional boundary condition; thus it would seem that boundary element methods such as MNPBEM would be incapable of accounting for nonlocal effects. However, MNPBEM can indeed account for nonlocality by introducing a fictitious surface layer with local permittivity around metal nanostructures which take the bulk permittivity.[88, 103, 104] It is possible that simulations using this fictitious surface layer to account for nonlocal polarization response may bring simulated values into closer agreement with experiment. This is my recommended approach for future simulations of this system.

5.8. Coupled system response: 100nm diameter particles

Samples containing 100nm diameter particles are iridescent: they demonstrate an angle-dependent reflectance, shown in Fig. 5.10. Iridescence is an interference phenomenon that can be caused by thin-film interference (such as in a soap bubble), or by photonic crystal structure (such as in the structural coloration of the Blue Morpho butterfly). Due to the particulate nature of these samples, we favored a photonic crystal rather than thin-film interference explanation. In order to quantify this phenomenon, I measured the p-polarized specular reflectance for incidence angles from 30 to 80 degrees. While the measured reflectance is independent of spacer thickness at 45 degree incidence, the resonant wavelength evolves non-monotonically with changing incidence angle (Fig. 5.11).
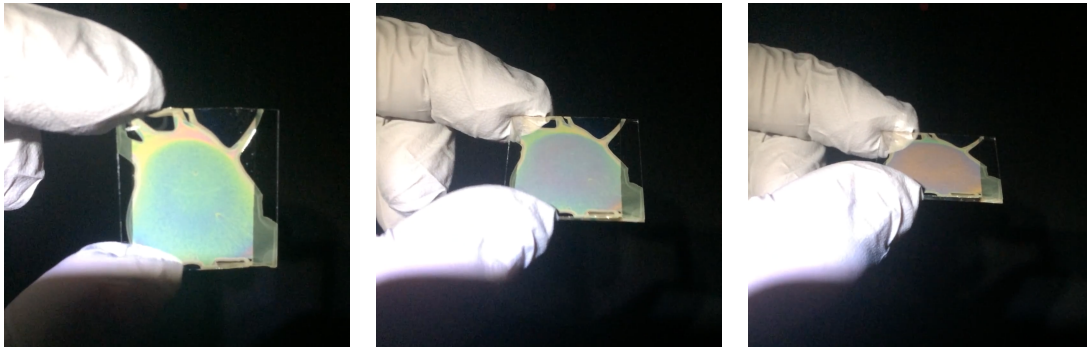
FIGURE 5.10. Iridescence displayed by 100nm particle samples.
Reflectance viewed at near-normal incidence (left) appears green. When the
substrate is tilted, the color progresses to a bluish (center) and finally to orange
(right) at grazing incidence.
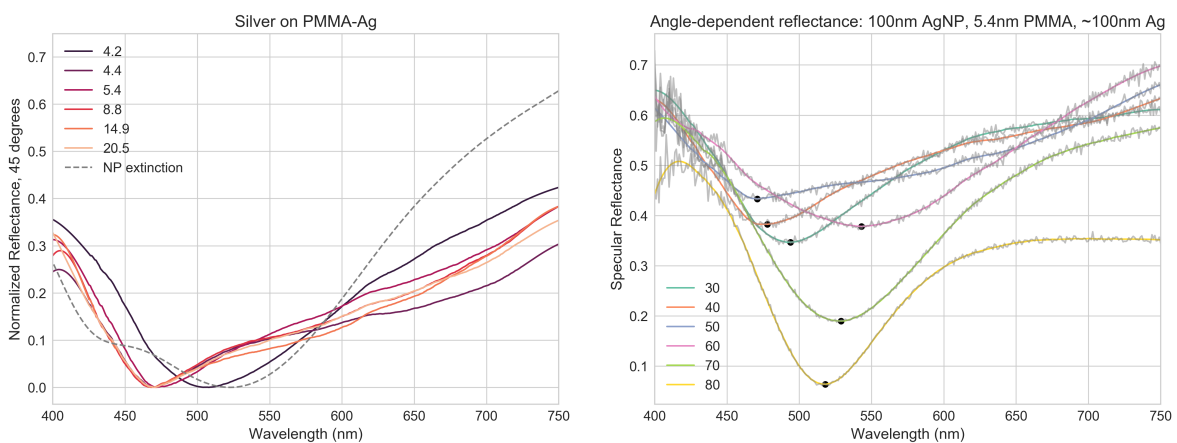
FIGURE 5.11. Reflectance of 100nm AgNP layered samples.
Left: Smoothed and offset 45 degree reflectance: the grey dashed line is the
transmission spectrum of the same concentration of nanoparticles (about $3 * 10^{10}$
particles/mL) on a PMMA-glass substrate. Right: Reflectance spectra demonstrate
a nonmonotonic shift as incidence angle is varied between 30 and 80 degrees.

SEM reveals that these particles are not close packed, so structural color from
a 2D photonic crystal origin is unlikely. Perhaps the color change of scatter from
different angles is due to a thin film interference effect between the scatter from the
particles and the reflected scatter from the flat silver film behind it. Or, since some
particles appear to be embedded within the PMMA film (Fig. 5.3), it may be that

the iridescence arises from multiple scattering from different depths of particle: a 3D photonic crystal effect. However, the effect is not seen in samples without the flat silver film, as demonstrated by the faint yellow color of the nanoparticles at the right and left edges of the sample in Fig. 5.10, where there is no flat silver film. Thus, a multiple scattering effect arising solely from particle embedding is unlikely. Instead, the phenomenon must arise from interference between light scattered from the particles at the front of the sample and the light scattered, reflected by the rear film, and potentially scattered again.

5.9. Summary

We have synthesized nanoparticle-film systems comprising silver nanoparticles, PMMA spacer layers, and flat silver films. We have observed, in agreement with existing literature, a coupled plasmon mode which redshifts with both decreasing gap thickness and increasing particle size. The optical resonance is tunable from 460nm to 560nm, by choosing nanoparticle diameters of 60nm or 80nm and PMMA thicknesses between 2–20nm thickness. An experimentally-relevant 532nm resonance is accessible by choosing 80nm diameter silver nanoparticles and a 13nm PMMA spacer. Our experimental measurements exhibit the same qualitative trends as numerical simulations, though not exact quantitative agreement. Clearly, silver poses challenges (oxidation, sulfide formation) which do not plague gold systems. The unpredictability of these challenges has driven many in the plasmonics community away from silver, at the expense of the opportunity to tune nanoparticle-film systems into the blue and green part of the visible spectrum. In this work, we have instead accepted those imperfections and so have gained insight into the feasibility of achieving tunability in the green.

CHAPTER VI

CONCLUSION

In this dissertation, we sought to harness small particles to produce materials whose optical properties are easily tailored to colors in the visible range. Our goal was to produce these materials using accessible methods, at low cost, and over large areas. In Chapter II, we reviewed the interactions of light with small particles. We learned that optical tunability in metallic nanoparticles is governed primarily by particle size and shape. We also found an opportunity to control optical tunability by varying the distance between nanoparticles and metallic substrates. In Chapter III, we focused on depositing silver nanoparticles using a simple wet chemistry procedure, and found that the surface coverage alone is insufficient to predict a system's extinction line shape. Instead, we find that the optical signature of a given sample depends mostly on the average particle size and the width of the size distribution. In Chapter IV, we simulated the scattering and extinction of metallic nanoparticles spaced nanometers away from a thin metal film. We found that the system's hybridized modes behave differently as the spacer thickness is varied, and that the mode with the greatest spectral tunability is influenced more by particle size than by spacer layer thickness. This underscores the importance of using monodisperse nanoparticles in such systems. Finally, in Chapter V, we built and measured these systems, confirming a predicted resonance in the green for silver particles near silver metal films.

We conclude that it is possible to build tunable metal nanostructures which cover large areas, and whose optical properties survive at the ensemble level, using fabrication tools such as metal evaporation and spin coating which are widely accessible to researchers. In particular, we found a route to a 532nm resonance in systems of evaporated silver films, nanometer-thick spin-coated polymer spacers, and

103

spin-coated silver nanoparticles. Such systems may be good candidates for plasmon-enhanced emission of fluorophores which absorb in the 532nm range.

6.1. Future directions

Several loose threads remain to be investigated experimentally. Primarily, there are two open questions about the morphology of both thin PMMA films and nanoparticles spun atom them. First, the morphology of the PMMA layer deserves close inspection. Our optical results suggest the possibility that particles are partly or completely surrounded by PMMA, either due to its surface roughness or partial dissolution or softening during nanoparticle spin coating. Atomic force microscopy, and additional ellipsometry of PMMA thin films before and after spin coating with a plain isopropanol solution, would clarify these open questions. Second, excellent understanding of the spatial distribution of nanoparticles over large areas a critical ingredient to design and simulate large-area sample behavior. In this work, we characterized nanoparticle spatial distribution using SEM. Often, charging was a challenge. Developing a fabrication technique for layered samples which allows for easy access to the metal flat film would make SEM easier; for example, applying conductive tape prior to polymer spin coating, or protecting part of the metal flat film from the spin coating process. More and better SEM images would bolster the existing spatial distribution data and allow for statistical confidence.

There is also an opportunity to extend this work experimentally for fluorescence enhancement applications. The nanoparticle-film system optimized for the 532nm range is a promising candidate for plasmon-enhanced fluorescence. A candidate model fluorophore is Rhodamine 6G, which has been well-studied, including within PMMA thin films, and absorbs near the 532nm line. Therefore, an immediate future direction

of this work would be to study the photoluminescence of layered samples containing Rhodamine 6G. By varying the dye-containing spacer thickness, it is possible to vary the hybridized resonance of the nanoparticle-film system to wavelengths slightly under or over the Rhodamine 6G absorption peak. Based on literature results, I hypothesize that overlapping the peak values will result in greatest emission. However, fluorophores with more complicated absorption structures (stemming from different excitation transitions) may also be interesting to study. It is possible that, rather than optimizing peak alignment, the highest level of emission enhancement may occur the nanoparticle-film and fluorophore absorption spectra have the greatest area of intersection.

When designing systems for different fluorophores, we would recommend extending the simulation methods in two ways to reach greater quantitative agreement between simulation and experiment. First, it should be straightforward to incorporate nonlocal effects in the Boundary Element Method using fictitious surface layers on metal interfaces; for thin gap distances especially this may prove to produce results which are more faithful to experiment. Second, finite element methods are a more exact way to incorporate nonlocal effects using the hydrodynamic model. The finite element method can validate or complement the computationally efficient boundary element method, which can then be applied with confidence to a wide range of geometries, either for design purposes or to understand ensembles by generating inputs for a size-distributed BEM method analogous to the size-distributed Mie theory.

Finally, enhancing absorption in thin polymer photovoltaic materials was an early motivator for this line of work. It may be possible to carefully design nanoparticle-film systems with multiple nanoparticle sizes, shapes, and materials that can be

used together to produce hybridized resonances which span the full absorption range of a given photovoltaic material. We note that there are relatively few studies of nanoparticle-film systems containing photovoltaic absorbers at this time.

6.2. Closing remarks

As we have seen, myriad applications hinge on the ability to predict and tune the optical response of silver nanostructures to specific colors in the visible range. The nanoscience community has made great strides in designing materials with exquisite properties, bringing these ideas to fruition by pushing the limits of nanofabrication, and analyzing the behavior of systems at the individual particle level to understand the limitations of physics at these dimensions and extend it accordingly. In this work, we sought to reality-test these accomplishments by focusing on simple and practical laboratory methods which can make the promise of tunable optical response accessible to a wide community of scientists.

REFERENCES CITED

[1] S. Munger, "Bad moon rising: The rare blue moon event of 1950,"
`https://seanmunger.com/2014/09/24/`
`bad-moon-rising-the-rare-blue-moon-event-of-1950/` (2014). Accessed:
2019-2-6.

[2] K. Ehlers, R. Chakrabarty, and H. Moosmüller, "Blue moons and martian
sunsets," Appl. Opt. **53**, 1808–1819 (2014).

[3] P. Lilienfeld, "Gustav Mie: the person," Appl. Opt. **30**, 4696–4698 (1991).

[4] Q. Zhao, J. Zhou, F. Zhang, and D. Lippens, "Mie resonance-based dielectric
metamaterials," Mater. Today **12**, 60–69 (2009).

[5] K. Kneipp, Y. Wang, H. Kneipp, L. T. Perelman, I. Itzkan, R. R. Dasari, and
M. S. Feld, "Single molecule detection using Surface-Enhanced Raman
Scattering (SERS)," Phys. Rev. Lett. **78**, 1667–1670 (1997).

[6] S. Nie and S. R. Emory, "Probing single molecules and single nanoparticles by
Surface-Enhanced Raman scattering," Science **275**, 1102–1106 (1997).

[7] D. O. Sigle, S. Kasera, L. O. Herrmann, A. Palma, B. de Nijs, F. Benz,
S. Mahajan, J. J. Baumberg, and O. A. Scherman, "Observing single molecules
complexing with cucurbit[7]uril through nanogap Surface-Enhanced Raman
spectroscopy," J. Phys. Chem. Lett. **7**, 704–710 (2016).

[8] W. Ye, M. Götz, S. Celiksoy, L. Tüting, C. Ratzke, J. Prasad, J. Ricken, S. V.
Wegner, R. Ahijado-Guzmán, T. Hugel, and C. Sönnichsen, "Conformational
dynamics of a single protein monitored for 24 h at video rate," Nano Lett. **18**,
6633–6637 (2018).

[9] M. Fleischmann, P. J. Hendra, and A. J. McQuillan, "Raman spectra of pyridine
adsorbed at a silver electrode," Chem. Phys. Lett. **26**, 163–166 (1974).

[10] D. L. Jeanmaire and R. P. Van Duyne, "Surface Raman spectroelectrochemistry:
Part i. heterocyclic, aromatic, and aliphatic amines adsorbed on the anodized
silver electrode," J. Electroanal. Chem. Interfacial Electrochem. **84**, 1–20
(1977).

[11] N. J. Borys and J. M. Lupton, "Surface-Enhanced light emission from single hot
spots in Tollens reaction silver nanoparticle films: Linear versus nonlinear
optical excitation," J. Phys. Chem. C **115**, 13645–13659 (2011).

[12] B. Yan, A. Thubagere, W. R. Premasiri, L. D. Ziegler, L. Dal Negro, and B. M. Reinhard, "Engineered SERS substrates with multiscale signal enhancement: nanoparticle cluster arrays," ACS Nano **3**, 1190–1202 (2009).

[13] R. T. Hill, J. J. Mock, Y. Urzhumov, D. S. Sebba, S. J. Oldenburg, S.-Y. Chen, A. A. Lazarides, A. Chilkoti, and D. R. Smith, "Leveraging nanoscale plasmonic modes to achieve reproducible enhancement of light," Nano Lett. **10**, 4150–4154 (2010).

[14] X. Wang, X. Zhu, Y. Chen, M. Zheng, Q. Xiang, Z. Tang, G. Zhang, and H. Duan, "Sensitive Surface-Enhanced Raman scattering detection using On-Demand postassembled Particle-on-Film structure," ACS Appl. Mater. Interfaces **9**, 31102–31110 (2017).

[15] K. Aslan, I. Gryczynski, J. Malicka, E. Matveeva, J. R. Lakowicz, and C. D. Geddes, "Metal-enhanced fluorescence: an emerging tool in biotechnology," Curr. Opin. Biotechnol. **16**, 55–62 (2005).

[16] J.-F. Li, C.-Y. Li, and R. F. Aroca, "Plasmon-enhanced fluorescence spectroscopy," Chem. Soc. Rev. **46**, 3962–3979 (2017).

[17] N. S. Abadeer, M. R. Brennan, W. L. Wilson, and C. J. Murphy, "Distance and plasmon wavelength dependent fluorescence of molecules bound to silica-coated gold nanorods," ACS Nano **8**, 8392–8406 (2014).

[18] P. K. Jain, W. Huang, and M. A. El-Sayed, "On the universal scaling behavior of the distance decay of plasmon coupling in metal nanoparticle pairs: A plasmon ruler equation," Nano Lett. **7**, 2080–2088 (2007).

[19] A. L. Rodarte and A. R. Tao, "Plasmon–Exciton coupling between metallic nanoparticles and dye monomers," J. Phys. Chem. C **121**, 3496–3502 (2017).

[20] M. I. Stockman, "Nanoplasmonics: The physics behind the applications," Phys. Today **64**, 39 (2011).

[21] J. D. Jackson, *Classical Electrodynamics, 3rd Edition*, Classical Electrodynamics (1998).

[22] N. W. Ashcroft and N. D. Mermin, *Solid State Physics* (Saunders College, Philadelphia, 1976).

[23] A. D. Rakić, A. B. Djurišić, J. M. Elazar, and M. L. Majewski, "Optical properties of metallic films for vertical-cavity optoelectronic devices," Appl. Opt., AO **37**, 5271–5283 (1998).

[24] C. F. Bohren and D. R. Huffman, *Absorption and scattering of light by small particles*, New York: Wiley (Wiley-VCH, Weinheim, Germany, 1983), wiley professional pbk. ed. ed.

[25] P. B. Johnson and R. W. Christy, "Optical constants of the noble metals," Phys. Rev. B Condens. Matter **6**, 4370–4379 (1972).

[26] S. A. Maier, *Plasmonics: Fundamentals and Applications* (Springer US, 2007).

[27] U. Kreibig and M. Vollmer, *Optical Properties of Metal Clusters:*, Springer Series in Materials Science (Springer Berlin Heidelberg, 1995).

[28] G. Toscano, J. Straubel, A. Kwiatkowski, C. Rockstuhl, F. Evers, H. Xu, N. A. Mortensen, and M. Wubs, "Resonance shifts and spill-out effects in self-consistent hydrodynamic nanoplasmonics," Nat. Commun. **6**, 7132 (2015).

[29] C. Ciracì and F. Della Sala, "Quantum hydrodynamic theory for plasmonics: Impact of the electron density tail," Phys. Rev. B Condens. Matter **93**, 205405 (2016).

[30] K. Ding and C. T. Chan, "An eigenvalue approach to quantum plasmonics based on a self-consistent hydrodynamics method," J. Phys. Condens. Matter **30**, 084007 (2018).

[31] C. Ciracì, J. B. Pendry, and D. R. Smith, "Hydrodynamic model for plasmonics: a macroscopic approach to a microscopic problem," Chemphyschem **14**, 1109–1116 (2013).

[32] C. Ciracì, R. T. Hill, J. J. Mock, Y. Urzhumov, A. I. Fernández-Domínguez, S. A. Maier, J. B. Pendry, A. Chilkoti, and D. R. Smith, "Probing the ultimate limits of plasmonic enhancement," Science **337**, 1072–1074 (2012).

[33] C. Ciracì, X. Chen, J. J. Mock, F. McGuire, X. Liu, S.-H. Oh, and D. R. Smith, "Film-coupled nanoparticles by atomic layer deposition: Comparison with organic spacing layers," Appl. Phys. Lett. **104**, 023109 (2014).

[34] A. Pitelet, E. Mallet, R. Ajib, C. Lemaître, E. Centeno, and A. Moreau, "Plasmonic enhancement of spatial dispersion effects in prism coupler experiments," Phys. Rev. B Condens. Matter **98**, 125418 (2018).

[35] R. Ruppin, "Optical properties of a plasma sphere," Phys. Rev. Lett. **31**, 1434–1437 (1973).

[36] V. V. Datsyuk and O. M. Tovkach, "Optical properties of a metal nanosphere with spatially dispersive permittivity," J. Opt. Soc. Am. B, JOSAB **28**, 1224–1230 (2011).

[37] J. Parker, "MiePy," (2016).

[38] G. Pellegrini, G. Mattei, V. Bello, and P. Mazzoldi, "Interacting metal nanoparticles: Optical properties from nanoparticle dimers to core-satellite systems," Materials Science and Engineering: C **27**, 1347–1350 (2007).

[39] E. Prodan, C. Radloff, N. J. Halas, and P. Nordlander, "A hybridization model for the plasmon response of complex nanostructures," Science **302**, 419–422 (2003).

[40] F. Della Sala and S. D'Agostino, *Handbook of Molecular Plasmonics* (CRC Press, 2013).

[41] M. I. Mishchenko, L. D. Travis, and A. A. Lacis, *Scattering, absorption, and emission of light by small particles* (2002).

[42] S. Sheikholeslami, Y.-W. Jun, P. K. Jain, and A. P. Alivisatos, "Coupling of optical resonances in a compositionally asymmetric plasmonic nanoparticle dimer," Nano Lett. **10**, 2655–2660 (2010).

[43] M. Quinten and U. Kreibig, "Optical properties of aggregates of small metal particles," Surf. Sci. **172**, 557–577 (1986).

[44] P. K. Jain and M. A. El-Sayed, "Plasmonic coupling in noble metal nanostructures," Chem. Phys. Lett. **487**, 153–164 (2010).

[45] A. B. Evlyukhin, C. Reinhardt, U. Zywietz, and B. N. Chichkov, "Collective resonances in metal nanoparticle arrays with dipole-quadrupole interactions," Phys. Rev. B Condens. Matter **85**, 245411 (2012).

[46] N. A. Mirin, K. Bao, and P. Nordlander, "Fano resonances in plasmonic nanoparticle aggregates," J. Phys. Chem. A **113**, 4028–4034 (2009).

[47] N. Meinzer, W. L. Barnes, and I. R. Hooper, "Plasmonic meta-atoms and metasurfaces," Nat. Photonics **8**, 889–898 (2014).

[48] A. S. Urban, X. Shen, Y. Wang, N. Large, H. Wang, M. W. Knight, P. Nordlander, H. Chen, and N. J. Halas, "Three-Dimensional plasmonic nanoclusters," Nano Lett. **13**, 4399–4403 (2013).

[49] B. Khlebtsov, A. Melnikov, V. Zharov, and N. Khlebtsov, "Absorption and scattering of light by a dimer of metal nanospheres: comparison of dipole and multipole approaches," Nanotechnology **17**, 1437 (2006).

[50] M. Quinten and U. Kreibig, "Absorption and elastic scattering of light by particle aggregates," Appl. Opt. **32**, 6173 (1993).

[51] V. Amendola and M. Meneghetti, "Size evaluation of gold nanoparticles by UVvis spectroscopy," J. Phys. Chem. C **113**, 4277–4285 (2009).

[52] F. Bourquard, A.-S. Loir, C. Donnet, and F. Garrelie, "In situ diagnostic of the size distribution of nanoparticles generated by ultrashort pulsed laser ablation in vacuum," Appl. Phys. Lett. **104**, 104101 (2014).

[53] S. Bakhti, N. Destouches, and A. V. Tishchenko, "Singular representation of plasmon resonance modes to optimize the near- and Far-Field properties of metal nanoparticles," Plasmonics **10**, 1391–1399 (2015).

[54] A. Curry, G. Nusz, A. Chilkoti, and A. Wax, "Substrate effect on refractive index dependence of plasmon resonance for individual silver nanoparticles observed using darkfield micro-spectroscopy," Opt. Express, OE **13**, 2668–2677 (2005).

[55] L. Novotny and B. Hecht, *Principles of Nano-Optics by Lukas Novotny* (Cambridge University Press, 2012).

[56] M. W. Knight, Y. Wu, J. B. Lassiter, P. Nordlander, and N. J. Halas, "Substrates matter: influence of an adjacent dielectric on an individual plasmonic nanoparticle," Nano Lett. **9**, 2188–2192 (2009).

[57] J. J. Mock, R. T. Hill, A. Degiron, S. Zauscher, A. Chilkoti, and D. R. Smith, "Distance-dependent plasmon resonant coupling between a gold nanoparticle and gold film," Nano Lett. **8**, 2245–2252 (2008).

[58] P. Nordlander and E. Prodan, "Plasmon hybridization in nanoparticles near metallic surfaces," Nano Lett. **4**, 2209–2213 (2004).

[59] Y. Wu and P. Nordlander, "Finite-Difference Time-Domain modeling of the optical properties of nanoparticles near dielectric substrates," J. Phys. Chem. C **114**, 7302–7307 (2010).

[60] H. Wang, Y. Wu, B. Lassiter, C. L. Nehl, J. H. Hafner, P. Nordlander, and N. J. Halas, "Symmetry breaking in individual plasmonic nanoparticles," Proc. Natl. Acad. Sci. U. S. A. **103**, 10856–10860 (2006).

[61] F. Le, N. Z. Lwin, J. M. Steele, M. Käll, N. J. Halas, and P. Nordlander, "Plasmons in the metallic nanoparticle-film system as a tunable impurity problem," Nano Lett. **5**, 2009–2013 (2005).

[62] U. Fano, "Effects of configuration interaction on intensities and phase shifts," Phys. Rev. **124**, 1866–1878 (1961).

[63] M. Hu, A. Ghoshal, M. Marquez, and P. G. Kik, "Single particle spectroscopy study of Metal-Film-Induced tuning of silver nanoparticle plasmon resonances," J. Phys. Chem. C **114**, 7509–7514 (2010).

111

[64] J. R. Lakowicz, Y. Shen, S. D'Auria, J. Malicka, J. Fang, Z. Gryczynski, and I. Gryczynski, "Radiative decay engineering. 2. effects of silver island films on fluorescence intensity, lifetimes, and resonance energy transfer," Anal. Biochem. **301**, 261–277 (2002).

[65] H. Wang, D. Chen, Y. Wei, Y. Chang, and J. Zhao, "A simple and sensitive assay of gallic acid based on localized surface plasmon resonance light scattering of silver nanoparticles through modified tollens process," Anal. Sci. **27**, 937–941 (2011).

[66] W.-J. Ong, L. K. Putri, L.-L. Tan, S.-P. Chai, and S.-T. Yong, "Heterostructured AgX/g-C3N4 (X=Cl and br) nanocomposites via a sonication-assisted deposition-precipitation approach: Emerging role of halide ions in the synergistic photocatalytic reduction of carbon dioxide," Appl. Catal. B **180**, 530–543 (2016).

[67] K. Rokesh, A. Pandikumar, S. Chandra Mohan, and K. Jothivenkatachalam, "Aminosilicate sol-gel supported zinc oxide-silver nanocomposite material for photoelectrocatalytic oxidation of methanol," J. Alloys Compd. **680**, 633–641 (2016).

[68] H. R. Stuart and D. G. Hall, "Absorption enhancement in silicon-on-insulator waveguides using metal island films," Appl. Phys. Lett. **69**, 2327 (1996).

[69] H. R. Stuart and D. G. Hall, "Island size effects in nanoparticle-enhanced photodetectors," Appl. Phys. Lett. **73**, 3815–3817 (1998).

[70] C. Gritti, S. Raza, S. Kadkhodazadeh, B. Kardynal, R. Malureanu, N. A. Mortensen, and A. V. Lavrinenko, "Broadband infrared absorption enhancement by electroless-deposited silver nanoparticles," Nanophotonics **6**, 83 (2017).

[71] M. S. M. Peterson, J. Bouwman, A. Chen, and M. Deutsch, "Inorganic metallodielectric materials fabricated using two single-step methods based on the tollen's process," J. Colloid Interface Sci. **306**, 41–49 (2007).

[72] Y. Yin, Z.-Y. Li, Z. Zhong, B. Gates, Y. Xia, and S. Venkateswaran, "Synthesis and characterization of stable aqueous dispersions of silver nanoparticles through the tollens process," J. Mater. Chem. **12**, 522–527 (2002).

[73] L. J. Davis, M. Boggess, E. Kodpuak, and M. Deutsch, "Modeling and numerical simulations of growth and morphologies of three dimensional aggregated silver films," J. Appl. Phys. **112**, 094310 (2012).

[74] D. L. Van Hyning, W. G. Klemperer, and C. F. Zukoski, "Silver nanoparticle formation: Predictions and verification of the aggregative growth model," Langmuir **17**, 3128–3135 (2001).

[75] K. Artyushkova, "GUI for multivariate image analysis of multispectral images, MATLAB central file exchange," (2004).

[76] L. H. Negri and C. Vestri, "lucashn/peakutils: v1.1.0," (2017).

[77] M. Newville, T. Stensitzki, D. B. Allen, and A. Ingargiola, "LMFIT: Non-Linear Least-Square minimization and Curve-Fitting for Python," (2014).

[78] D. Stauffer, "Monte carlo study of density profile, radius, and perimeter for percolation clusters and lattice animals," Phys. Rev. Lett. **41**, 1333–1336 (1978).

[79] C. E. Román-Velázquez, C. Noguez, and R. G. Barrera, "Substrate effects on the optical properties of spheroidal nanoparticles," Phys. Rev. B Condens. Matter **61**, 10427–10436 (2000).

[80] C. Noguez, "Surface plasmons on metal nanoparticles: The influence of shape and physical environment," J. Phys. Chem. C **111**, 3806–3819 (2007).

[81] R. R. Irani and C. F. Callis, *Particle size: measurement, interpretation, and application* (Wiley, New York, 1963).

[82] P. Nordlander, C. Oubre, E. Prodan, K. Li, and M. I. Stockman, "Plasmon hybridization in nanoparticle dimers," Nano Lett. **4**, 899–903 (2004).

[83] M. Quinten, "Beyond Mie's theory I – nonspherical particles," in "Optical Properties of Nanoparticle Systems," (Wiley-VCH Verlag GmbH & Co. KGaA, 2011), pp. 245–316.

[84] K. K. Madoyan, A. H. Melikyan, and H. R. Minassian, "Radiation damping of surface plasmons in a pair of nanoparticles and in nanoparticles near interfaces," J. Phys. Chem. C **116**, 16800–16805 (2012).

[85] J. J. Mock, R. T. Hill, Y.-J. Tsai, A. Chilkoti, and D. R. Smith, "Probing dynamically tunable localized surface plasmon resonances of film-coupled nanoparticles by evanescent wave excitation," Nano Lett. **12**, 1757–1764 (2012).

[86] F. M. Huang, D. Wilding, J. D. Speed, A. E. Russell, P. N. Bartlett, and J. J. Baumberg, "Dressing plasmons in particle-in-cavity architectures," Nano Lett. **11**, 1221–1226 (2011).

[87] B. Yu, J. Woo, M. Kong, and D. M. O'Carroll, "Mode-specific study of nanoparticle-mediated optical interactions in an absorber/metal thin film system," Nanoscale **7**, 13196–13206 (2015).

[88] J. Waxenegger, A. Trügler, and U. Hohenester, "Plasmonics simulations with the MNPBEM toolbox: Consideration of substrates and layer structures," Comput. Phys. Commun. **193**, 138–150 (2015).

[89] U. Hohenester and A. Trügler, "MNPBEM – a Matlab toolbox for the simulation of plasmonic nanoparticles," Comput. Phys. Commun. **183**, 370–381 (2012).

[90] S. Yashima, H. Sugimoto, H. Takashina, and M. Fujii, "Fluorescence enhancement and spectral shaping of silicon quantum dot monolayer by plasmonic gap resonances," J. Phys. Chem. C **120**, 28795–28801 (2016).

[91] G.-C. Li, Y.-L. Zhang, and D. Y. Lei, "Hybrid plasmonic gap modes in metal film-coupled dimers and their physical origins revealed by polarization resolved dark field spectroscopy," Nanoscale **8**, 7119–7126 (2016).

[92] G.-C. Li, Q. Zhang, S. A. Maier, and D. Lei, "Plasmonic particle-on-film nanocavities: a versatile platform for plasmon-enhanced spectroscopy and photochemistry," Nanophotonics **7**, 1865–1889 (2018).

[93] Z. Qi, Q. Wang, Y. Zhai, J. Xu, Z. Tao, Y. Tu, W. Lei, and J. Xia, "Plasmon-enhanced energy transfer between quantum dots and tunable film-coupled nanoparticles," J. Phys. D Appl. Phys. **49**, 235103 (2016).

[94] H. Szmacinski, R. Badugu, F. Mahdavi, S. Blair, and J. R. Lakowicz, "Large fluorescence enhancements of fluorophore ensembles with multilayer plasmonic substrates: Comparison of theory and experimental results," J. Phys. Chem. C **116**, 21563–21571 (2012).

[95] C. Lumdee, B. Yun, and P. G. Kik, "Wide-Band spectral control of Au nanoparticle plasmon resonances on a thermally and chemically robust sensing platform," J. Phys. Chem. C **117**, 19127–19133 (2013).

[96] R. T. Hill, K. M. Kozek, A. Hucknall, D. R. Smith, and A. Chilkoti, "Nanoparticle-Film plasmon ruler interrogated with transmission visible spectroscopy," ACS Photonics **1**, 974–984 (2014).

[97] Y. Brasse, M. B. Müller, M. Karg, C. Kuttner, T. A. F. König, and A. Fery, "Magnetic and electric resonances in Particle-to-Film-Coupled functional nanostructures," ACS Appl. Mater. Interfaces **10**, 3133–3141 (2018).

[98] W. M. Wilson, J. W. Stewart, and M. H. Mikkelsen, "Surpassing single line width active tuning with photochromic molecules coupled to plasmonic nanoantennas," Nano Lett. **18**, 853–858 (2018).

[99] T. Okamoto and I. Yamaguchi, "Optical absorption study of the surface plasmon resonance in gold nanoparticles immobilized onto a gold substrate by Self-Assembly technique," J. Phys. Chem. B **107**, 10321–10324 (2003).

[100] B. Yu, J. I. Tracey, Z. Cheng, M. Vacha, and D. M. O'Carroll, "Plasmonic sphere-on-plane systems with semiconducting polymer spacer layers," Phys. Chem. Chem. Phys. **20**, 11749–11757 (2018).

[101] H. Raether, *Surface Plasmons on Smooth and Rough Surfaces and on Gratings*, vol. 111 of *Springer Tracts in Modern Physics* (1988).

[102] C. B. Walsh and E. I. Franses, "Ultrathin PMMA films spin-coated from toluene solutions," Thin Solid Films **429**, 71–76 (2003).

[103] U. Hohenester and A. Trügler, "MNPBEM toolbox," `http://physik.uni-graz.at/mnpbem/` (2014). Accessed: 2019-2-7.

[104] Y. Luo, A. I. Fernandez-Dominguez, A. Wiener, S. A. Maier, and J. B. Pendry, "Surface plasmons and nonlocality: a simple model," Phys. Rev. Lett. **111**, 093901 (2013).